This is to certify that the
thesis entitled

Development and Characterization of Biocomposite Cellular
Beams and Plates for Load-Bearing Components

presented by

Mario J. Quagliata

has been accepted towards fulfillment
of the requirements for the

M.S. degree in Civil Engineering

Major Professor's Signature

8/21/03

Date

DEVELOPMENT AND CHARACTERIZATION OF BIOCOMPOSITE CELLULAR BEAMS AND PLATES FOR LOAD-BEARING COMPONENTS

By

Mario J. Quagliata

A THESIS

Submitted to
Michigan State University
in partial fulfillment of the requirements
for the degree of

MASTER OF SCIENCE

Department of Civil and Environmental Engineering

2003

ABSTRACT

DEVELOPMENT AND CHARACTERIZATION OF BIOCOMPOSITE CELLULAR BEAMS AND PLATES FOR LOAD-BEARING COMPONENTS

By

Mario J. Quagliata

Increased environmental awareness and interest in long-term sustainability of material resources has motivated considerable advancements in composite materials made from natural fibers and resins. However, despite the developments on the technology of biocomposites materials, their lower stiffness and strength properties has limited their applications to non-load-bearing components.

The stiffness of a structural component depends both on the material and structural stiffness. Thus, the material stiffness shortcomings of biocomposites can be overcome through efficient structural configurations. Popular designs for advanced composites based on this idea are cellular and sandwich structures which respectively maximize material and structural performance.

The objective of this research was to investigate the feasibility of using biocomposite materials for primary load-bearing components in civil structures by utilizing high-performance structural forms. The research work presented in this thesis focuses on the investigation of this concept through the development, manufacturing, and characterization, both experimental and analytical, of laboratory-scale cellular beams and plates. These studies were used to analytically investigate the feasibility of using biocomposite materials for full-size structural components for civil structures, and assess the future research needs for the development of load-bearing biocomposite structures.

To my parents; Michael and Susan
for their love, support, and guidance throughout my life

ACKNOWLEDGEMENTS

I am most grateful to my advisor, Dr. Rigoberto Burgueño, for his insights, encouragement, time, and patience, which provided me with a guiding light to follow throughout this research. This work was enabled and sustained by his vision and ideas.

I wish a very special thanks to Dr. Amar Mohanty and Dr. Manjusri Misra for providing their expertise in biocompostie materials, and for their guidance, encouragement, and enthusiasm throughout this research.

I am grateful to Geeta Mehta for her guidance in the laboratory, and for all her help in manufacturing the cellular beams and plates. Her friendship and encouragement helped me through the difficult times in this research.

I wish to thank the member of my master's committee, Dr. Ronald Harichandran, Dr. Manjusri Misra, Dr. Amar Mohanty, and Dr. Amit Varma, for their time and insightful comments.

I wish thanks to James "JC" Brenton for his help in fabricating the cellular beam and plate molds, and Siavosh Ravanbakhsh for his help in preparing the test setup and testing the cellular beams and plates at the Civil Infrastructure Laboratory.

I would like to acknowledge Robert Jurek, Michael Rich, and Kelby Thayer from the Composite Materials and Structures Center for their help in the manufacturing and material testing performed in the laboratory for this project.

This study was funded by a 2002 Research Excellence Funds award through Michigan State University's Composite Materials and Structures Center, which is gratefully acknowledged.

TABLE OF CONTENTS

LIST OF TABLES

LIST OF FIGURES

CHAPTER 1 INTRODUCTION

1.1 Overview

Fiber reinforced polymer (FRP) composites have surpasses their initial target applications in the aerospace industry to become a viable material alternative in the sporting goods, automotive, and construction industries. High performance FRP composites made with synthetic fibers such as carbon, glass, or aramid embedded in polymeric matrices provide the advantages of high stiffness and strength to weight ratio and increased chemical inertness compared to conventional construction materials, i.e., wood, concrete, and steel. In spite of these advantages, the wide-spread use of synthetic FRP composites has been limited, among several factors, due to their higher initial material costs, their use in non-efficient structural forms, and their environmental impact.

Increased environmental awareness and the interest in long-term sustainability of construction materials have thus challenged the development of environmentally friendlier alternatives to synthetic oil-based FRP composites (Mohanty et al. 2000). Natural-fiber-reinforced polymer composites, or biocomposites, have emerged in the past decade as an environmentally friendly and cost-effective option to synthetic FRP composites. Despite the interest and environmental appeal of biocomposites, their use has been limited to non-primary, or non-load-bearing applications due to their lower strength and stiffness compared with synthetic FRP composites (Biswas et al. 2001). Recent developments, however, have shown that the properties of "engineered" biocomposites are comparable with those of entry-level structural synthetic fiber composites, namely glass-FRP (Mohanty et al. 2001, Rout et al. 2001).

While biocomposite materials with specific properties equivalent to entry-level structural materials are feasible, this performance level is still not enough to compete with our existing construction materials. However, the performance of a component depends on both its material and structural properties. The lower material stiffness of biocomposite materials can thus be overcome by using efficient structural configurations that place the material in specific locations for highest structural performance for minimum material use and thus minimum weight (Gibson and Ashby 1988). This concept has been recognized for some time and has recently gained new attention due to the way that nature's own materials and structures follow this principle.

The above concepts have been integrated in this thesis, where engineered biocomposites and their arrangement in efficient cellular and sandwich configurations are shown to lead to environmentally friendly and structural efficient structural components. In the following section the background on the current uses of FRP composites in load bearing civil structures is presented to give context to the use of biocomposites in the civil sector. This is followed by background on biocomposite materials, and high-performance cellular and sandwich structural forms that can be used to efficiently arrange biocompostie materials. The chapter is concluded with the objective and scope of the research work presented in this thesis.

1.2 Fiber Composites for Load Bearing Civil Structures

High performance FRP composites, with synthetic fibers such as carbon, glass, or aramid, are increasingly being considered for use in civil infrastructure applications ranging from rehabilitation of buildings and bridges to the construction of new structural systems (Karbhari and Seible 2000). The advantages of FRP composites that have attracted their use in civil structures includes: high specific properties, enhanced fatigue life, corrosion resistance, and tailorable properties (Barbero and GangaRao 1991). Specific applications of FRP composites in civil infrastructure include: retrofit of columns in seismic regions, strengthening of degraded beam, slab and deck structures, replacement and new construction of bridge decks, and new structural systems (Karbhari and Seible 2000). FRP composites have also been used for reinforcement and prestressing cables in reinforced and prestressed concrete, and have been manufactured in standard pultruded shapes (Barbero and GangaRao 1992, and 1991).

Despite the advantages of high performance FRP composites, their wide-spread implementation in civil infrastructure has been limited, primarily due to: (i) higher initial material cost, (ii) lack of familiarity in most areas of civil engineering, (iii) lack of comprehensive standards and design guidelines at the present, and (iv) need for integrated materials-process-design structure in product development (Karbhari and Seible 2000). While biocomposites materials may be a low-cost, environmentally friendly alternative to synthetic FRP composites, biocomposites will also encounter the same issues limiting the implementation of high performance FRP composites in civil infrastructure.

1.3 Bio-Based Composite Materials

Natural fibers embedded in a natural or synthetic polymeric matrix, known as *biocomposites*, have gained recent interest because of their low material and manufacturing costs, light weight, high specific modulus (elastic modulus over density), and environmentally friendly appeal (Mohanty et al. 2000). Depending on their origin, natural fibers may be grouped into: bast (stem), leaf, and seed types (Brouwer 2000).

The best know examples are: (i) bast: hemp, flax, jute, kenaf, and ramie; (ii) leaf: sisal, henequen, and pineapple leaf fiber; (iii) seed: cotton, coir. Bast fibers have the highest mechanical properties (especially: hemp, flax, and ramie) and thus, are the ones typically considered for high-quality applications. Typical mechanical properties of these fibers together with E-glass fibers are given in Table 1.1. The density of natural fibers is about half that of E-glass (Table 1.1), which makes their specific strength quite comparable, while the elastic modulus and specific modulus are comparable or even superior to E-glass fibers.

Table 1.1. Typical properties of glass fiber and natural fibers (after Brouwer 2000)

	Fibers					
Properties	*E-Glass*	*Flax*	*Hemp*	*Jute*	*Ramie*	*Sisal*
Density (g/cm^3)	2.55	1.40	1.48	1.46	1.50	1.33
Tensile Strength (Mpa)	2400	800 - 1500	550 - 900	400 - 800	500	600 - 700
E-Modulus (Gpa)	73	60 - 80	70	10 - 30	44	38
Specific Modulus (E/density)	29	26 - 46	47	7 - 21	29	29
Elongation at Failure (%)	3	1.2 - 1.6	1.6	1.8	2	2-3
Moisture Absorption (%)	--	7	8	12	12 - 17	11
Price/kg ($) *Raw*	1.3	0.5 - 1.5	0.6 - 1.8	0.35	1.5 - 2.5	0.6 - 0.7
Price/kg ($) *Fabric/mat*	1.7 - 3.8	2 - 4	2 - 4	0.9 - 2	1.5 - 2.5	--

The applications for which biocomposites have been studied include interior and exterior paneling of automobiles, interior paneling in rail vehicles, furniture, and replacement of wood products in housing applications. Daimler Chrysler (2001) has used biocomposites of green flax and hemp fiber mats with polyester for under body panels of the EvoBus (a touring coach). Daimler Chrysler found replacing the under body panel, previously a glass fiber composite, with biocomposites required 83 percent less energy to manufacture, and the resulting part was 40 percent cheaper. In addition, the same tools and machine used to manufacture the part with glass-fiber composites were used for manufacturing with biocomposites. Biocomposite materials have also been used for interior paneling applications in automobiles, including door paneling and rear shelf paneling (Biswas et al. 2002). The interior paneling of rail vehicles in Germany has also been manufactured using biocomposites, mainly for weight savings over glass-fiber composites (Nickel and Riedel 2003). In this application the standards for fire protection are very high in Germany. Thus, the biocomposites were treated with flame retardants to attain the high levels of fire-protection required by the standards. Phenix Biocomposites (2003) of Mankato, Minnesota have developed biocomposite materials with decorative surfaces for furniture, table tops, wall panels, and other home and office finished surface applications. These applications by Phenix Biocomposties show that biocomposites can be manufactured and used in products where attractive surface finishing is required. Jute and coir based biocomposites have been developed in India as substitutes for plywood and medium density fiber boards for low-cost housing needs (Biswas et al. 2001). Other products under development include the use of sisal-based biocomposites as panels and roofing sheets, which could also be used as false ceilings and partition boards. The current market uses of bio-based composites in North America are shown in Figure 1.1 (Mohanty et al. 2000).

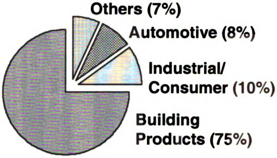

Figure 1.1. North American major end markets of natural fiber composites, year 2000

Consideration of biocomposites for load-bearing, i.e. structural, applications has been neglected due to their low stiffness and strength in comparison with conventional construction materials. However, recent research on biocomposite materials has shown that "engineered," or treated, natural fibers can lead to biocomposites with properties that can compete with glass fiber composites (Figure 1.2). This has motivated further research initiatives that consider biocomposites as a technical and environmentally conscious alternative to E-glass reinforced fiber composites (the most common synthetic fiber composites) without sacrificing performance. Natural fibers/unsaturated polyester composites show lower density, equal flexural modulus, comparable flexural strength, but relatively poor impact strength as compared to a glass fibers composite as show in Figure 1.2 (Mishra et al. 2002, Mohanty et al. 2000).

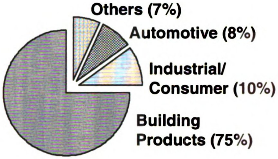

Figure 1.1. North American major end markets of natural fiber composites, year 2000

Consideration of biocomposites for load-bearing, i.e. structural, applications has been neglected due to their low stiffness and strength in comparison with conventional construction materials. However, recent research on biocomposite materials has shown that "engineered," or treated, natural fibers can lead to biocomposites with properties that can compete with glass fiber composites (Figure 1.2). This has motivated further research initiatives that consider biocomposites as a technical and environmentally conscious alternative to E-glass reinforced fiber composites (the most common synthetic fiber composites) without sacrificing performance. Natural fibers/unsaturated polyester composites show lower density, equal flexural modulus, comparable flexural strength, but relatively poor impact strength as compared to a glass fibers composite as show in Figure 1.2 (Mishra et al. 2002, Mohanty et al. 2000).

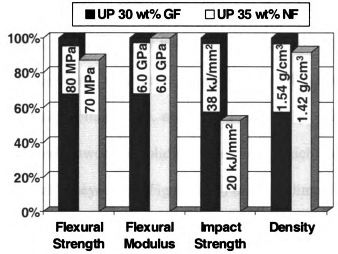

Figure 1.2. Comparison of natural fiber (NF) and glass fiber (GF) – unsaturated polyester (UP) composites

1.4 Load-Bearing Biocomposites

While the properties of biocomposites can compete with those of E-glass composites, their strength, and particularly stiffness, is lower than that of conventional structural materials. This has limited their application primarily to non-load-bearing, or non-structural, components. One way to overcome their low mechanical properties is through hybridization with stiffer and stronger (i.e., synthetic) fibers (Mishra et al. 2003, Biswas et al. 2001). A more efficient way of improving the performance of biocomposite components is to use them in high-performance structural forms. Scrutiny of nature's materials shows that high structural efficiency can be achieved by strategic material organization (Gibson and Ashby 1988, Gunderson and Thorp 1993). Optimized hierarchical cellular arrangement of the material leads to enhanced and efficient use of the material system and thus structural components at reduced weight and cost.

The stiffness shortcomings of biocomposites can then be overcome by efficient structural configurations. By looking to nature for efficient structural forms, the most common are cellular sandwich structures, which consist of a dense skin integrally connected to a low-density cellular core, as shown Figure 1.3a. Cellular materials are made of an interconnected network of solid struts or plate, which have the general form of either two-dimensional honeycombs (Figure 1.3b) or three-dimensional foams (Figure 1.3c). By integrally connecting the low-density cellular core with the dense skin face sheets delamination between the core and face sheets can be avoided, which can lead to premature failure of sandwich structures (Jones 1999).

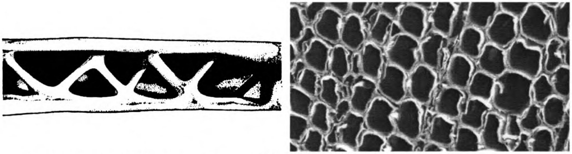

(a) A section through a bird's wing (Thompson 1961)

(b) Wood 2-D cellular structure

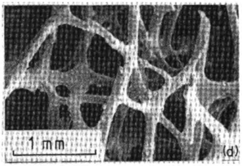

(c) Cancellous bone 3-D cellular structure (Gibson and Ashby 1988)

Figure 1.3. Sandwich structures and cellular structures in nature

1.5 Objective and Scope

The objective of this research is to investigate the feasibility of using biocomposite materials for primary load-bearing components in civil structures. High-performance structural forms, such as cellular and sandwich configurations, will be investigated with the aim of improving the structural performance of biocomposites for application in load-bearing civil structures. The thesis focuses on the investigation of this concept through the development, manufacturing, and characterization, both experimental and analytical, of laboratory-scale cellular beams and plates. The potential of cellular biocomposites for full-size load-bearing structural components is studied by comparing extrapolated results to the performance of commercial components made with conventional construction materials, and by selecting dimensions of cellular biocomposite structures for civil applications based on deflection limits given in structural design codes. The research work involved the following tasks:

- Experimental material characterization of biocomposite material systems
- Identification and characterization of high-performance structural forms using laboratory-scale cellular beams and plates
- Identification and validation of analytical tools for biocomposite materials and cellular structures
- Analytically studies on the feasibility of using biocomposite materials for load-bearing structural components

The research presented in this thesis integrates all the aspects of structural design, from selection of the material and structural form, to manufacturing of the structural component. Thus, a holistic view of the design process for biocomposite structural components is shown, which emphasizes the impact each link in the design process has on the performance of the resulting structural component. Understanding this interaction between the various aspects of design can help engineers design efficient structures, which meet the desired performance for a specific application.

Based on the above research tasks, the chapters of the thesis are organized in the following order:

- Chapter 2: Material development and characterization
- Chapter 3: Cellular beams and plates
- Chapter 4: Analytical studies
- Chapter 5: Results, feasibility, and recommendations
- Chapter 6: Conclusions

CHAPTER 2 MATERIAL DEVELOPMENT AND CHARACTERIZATION

2.1 Overview

A material experimental program was undertaken with two main objectives: (i) to establish a minimum database for biocomposite materials to asses their current status and evaluate their feasibility for structural applications, and (ii) to provide the necessary material characterization for the material systems used in the structural experimental studies (Chapter 3). Hybrid material systems using hemp fibers in combination with chopped E-glass, and woven jute fabrics were also investigated. In addition, material systems using chopped E-glass, unidirectional carbon, and woven jute mats were investigated to provide the necessary material characterization for the integral face sheet materials used in the structural experimental studies (Chapter 3). The performance of the biocomposite material systems was compared with that of E-glass composite materials. A schematic of the material experimental program is shown in Figure 2.1.

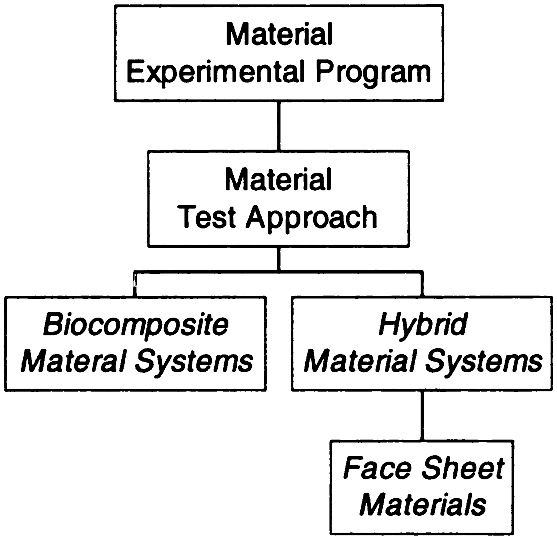

Figure 2.1. Schematic of the material experimental program

In the following sections, the test approach and testing procedures followed by the test results from the biocomposite and hybrid material systems are provided. The manufacturing procedures for both the biocomposite and hybrid material systems is also presented and summarized in photographic sequences.

2.2 Material Test Approach

The mechanical properties of the material systems were studied through American Society of Testing Materials (ASTM) material testing procedures for fiber-reinforced plastics. The following mechanical properties were evaluated in the material experimental program:

- Tensile modulus, strength, and elongation at break
- Fracture toughness
- Coefficient of thermal expansion
- Moisture absorption

Details of the testing procedures used for each material property are provided in the following sections. All of the material characterization testing was conducted at the facilities of the Composite Materials and Structures Center (CMSC) at Michigan State University.

Specimens for performing the mechanical property tests were prepared by manufacturing a 200 mm x 200 mm compression molded plate for each material system type. Manufacturing details of the compression molded plates are provided in sections 2.3.2 and 2.4.2. The number and size of the test specimens required for each test were prepared using the layout shown in Figure 2.2. The samples were cut from the plate using a band saw, and were then machined to the proper shape and dimensions using standard templates.

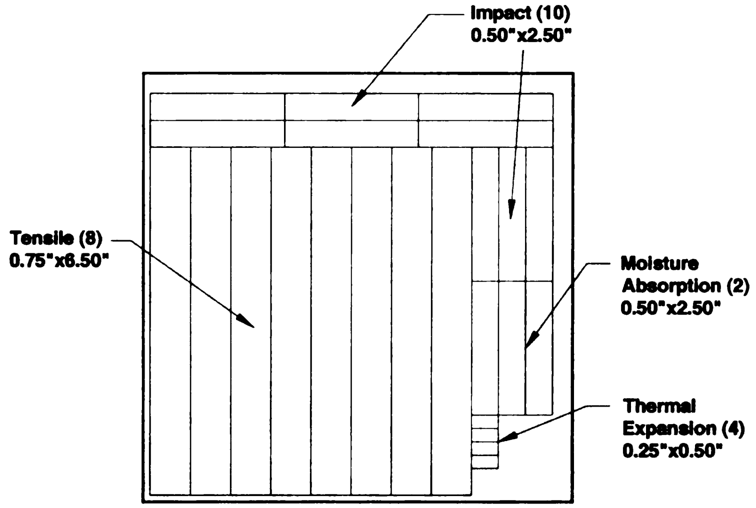

Figure 2.2. Sample layout for material property tests

2.2.1 Tensile Testing

The tensile properties of the material systems were determined using ASTM D790 specifications for sample shape, size, conditioning, and testing procedure. ASTM Type I dogbone specimens were used: a 13.0 mm x 57.0 mm narrow section with 20 mm-wide grip ends and a total length of 165 mm (Figure 2.3). A Universal Testing Systems testing frame with an external laser extensometer was used to conduct the tests. The applied load and displacement on the narrow section of the sample were recorded, converted to a stress-strain response, and used to determine the tensile modulus, strength, and elongation at break. The samples were only tested in one direction due to the random orientation of the natural fiber reinforcement.

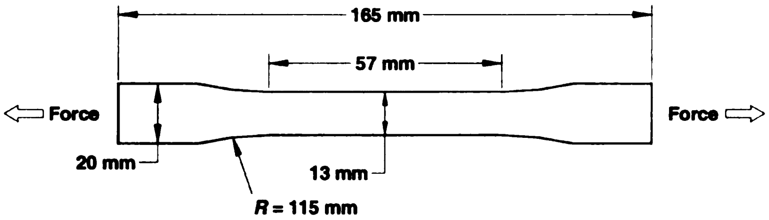

Figure 2.3. ASTM D790 Type I tensile specimen

2.2.2 Impact Strength Testing

The Impact strength of the material systems was measured using ASTM D256 specifications for sample shape, size, conditioning, and testing procedure. ASTM Izod type test specimens were used: 63 mm x 12.7mm samples with a 45° notch and bottom radius of 0.25 mm at the sample mid-length (Figure 2.4a). The samples were tested using ASTM Test Method A (Izod Type), where the sample is cantilevered in the setup with the notch facing the striking edge (Figure 2.4b).

The samples were tested by swinging the pendulum, with striking edge, and striking the notched cantilevered sample. The energy lost (required to break the sample) as the pendulum swings through the sample is measured from the distance of the pendulum follow through. The energy lost per unit of specimen thickness at the notch (J/m) is reported as the impact strength. The testing apparatus used for this experiment program (Figure 2.5) automatically measured the energy lost and computed the impact strength. Wind and friction losses in the system were measured and used to correct the impact strength value.

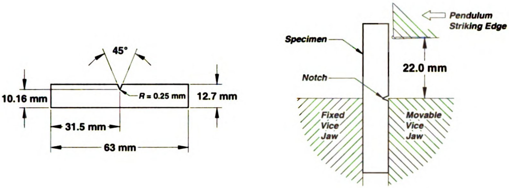

(a) Izod Type test specimen (b) Izod test (Test Method A)

Figure 2.4. Impact strength testing, ASTM D256

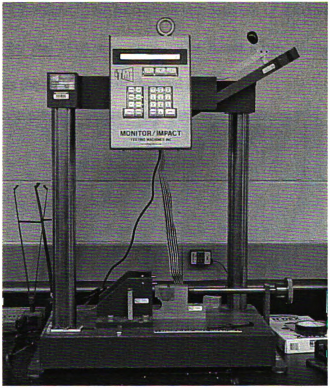

Figure 2.5. Impact strength testing apparatus

2.2.3 Coefficient of Thermal Expansion Testing

The coefficient of thermal of the material systems was measured using the Thermal Mechanical Analysis (TMA) apparatus at the CMSC (Figure 2.6). The two main components of the TMA apparatus are the probe and the furnace. The probe holds the sample and measures the change in length during the test. The furnace applies heat to the sample at a specified rate of temperature increase. The temperature and displacement are measured throughout the test to generate a strain-temperature curve. The dimensions of the test specimens were 6.3 mm in height by 12.7 mm in width. The samples were dried in a vacuum oven at 80°C and 100 kPa pressure for at least one hour before testing to eliminate any dimensional changes due to moisture effects.

The samples were tested by heating the specimen from room temperature to 140°C at a rate of 4°C/minute. The strain and temperature of the sample were measured throughout the test by the TMA apparatus. The linear slope of the strain-temperature curve was reported as the coefficient of thermal expansion.

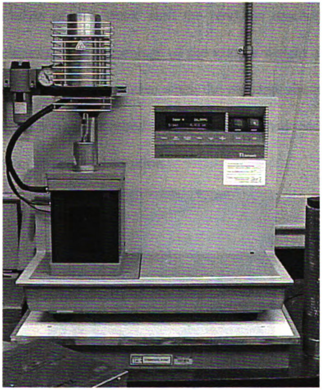

Figure 2.6. Thermal apparatus used for coefficient of thermal expansion tests

2.2.4 Moisture Absorption Testing

The moisture absorption of the material systems was measured using an environmental chamber (Figure 2.7), which maintains a constant temperature and humidity. The dimensions of the test specimens were 12.7 mm by 63 mm. The side edges of the samples, which were exposed when the samples were cut from the compression molded plate, were sealed with unsaturated polyester resin to be consistent with the material on the surface of the specimen.

The moisture absorption testing was performed by storing the samples in the environmental chamber at 30°C and 90% humidity and measuring the increase in weight of the samples. On the first days of testing, measurements were taken at: 1 hour, 2 hours, 4 hours, 8 hours, 18 hours, 24 hours, and 48 hours. After the initial readings, measurements were taken once a week until the readings reached a steady state (no longer absorbing moisture). The percentage of the sample weight absorbed was plotted against the square root of time to determine when the moisture absorption had reached a steady state. The percent weight absorbed once the readings had reached steady state was reported as the degree of moisture absorption.

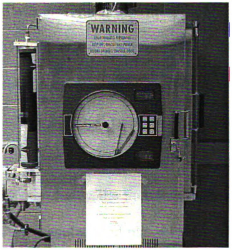

Figure 2.7. Environmental chamber used for moisture absorption testing

2.3 Biocomposite Material Systems

The material test program was initiated by identifying potential biocomposite material systems and performing material testing to evaluate their probable use for load-bearing structural components. Hemp fiber was determined to be the stiffest, cheapest, and most readily available fiber type for use in load-bearing structural applications. Thus, hemp was used as the base natural fiber reinforcement in the biocomposite materials. Flax fibers were also used for specific applications. Unsaturated polyester resin was also determined to be the most readily available and cheapest resin type for use in load-bearing structural applications. Thus, unsaturated polyester was used as the matrix for the biocomposite and hybrid material systems. The performance of the biocomposite material systems was compared with that of E-glass fiber reinforced composite materials.

The fiber content in the material studies was selected to match the fiber content in the cellular beams and plates manufactured for the structural experimental program (Chapter 3). In most cases, the fiber weight fraction (ratio of fiber weight to total weight) was between 10-20%, which corresponds to roughly an 8-16% fiber volume fraction. The E-glass material system was manufactured with approximately 30% fibers by weight, which corresponds to roughly a 15% fiber volume fraction. At this fiber weight fraction the E-glass and biocomposite material systems have approximately the same fiber volume fraction. Because of the high percentage of resin used in the material systems, resin was squeezed out of the sample during the pressing of the compression molded plates. The squeeze out of resin during the pressing of the sample made it difficult to control the fiber content in the manufactured plates for material characterization. Thus, the fiber content could not exactly match the contents in the cellular beams and plates manufactured for the structural experimental program.

2.3.1 Materials and Constituents

The biocomposite plates for material characterization were designed to match the material systems used for the cellular beams and plates for the structural experimental program (Chapter 3). All biocomposite material systems were composed of either hemp fibers or chopped flax fibers and unsaturated polyester resin with a fiber weight fraction of 10-20%, which corresponds to roughly an 8-16% fiber volume fraction. The hemp fibers (Figure 2.8a) were chopped with an average length of 6mm, and purchased from BioInnova of Germany. The flax fibers (Figure 2.8b) were chopped with an average length of 2 mm, contained 50% core material, and were purchased from Flax Craft of New Jersey. The E-glass fibers were chopped with an average length of 7 mm, sized for polyester resin, and purchased from Owens Corning of Ohio. The resin system used was ortho unsaturated polyester (UPE) with methyl ethyl ketone peroxide (MEKP) catalyst (1% by weight of resin), and cobalt naphthenate (CN) promoter (0.03% by weight of resin). The resin system composition is show in tabular form in Table 2.1.

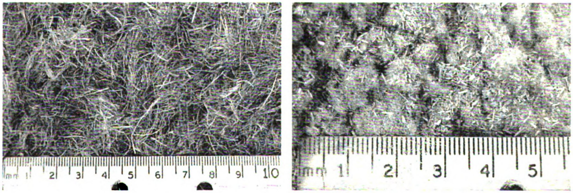

(a) Hemp fibers

(b) Chopped flax, 50% fibers, 50% core

Figure 2.8. Close-up view of natural fibers used for manufacturing

Table 2.1. Unsaturated polyester (UPE) resin system

Resin System Component	*Percentage by Weight of Resin*
Ortho Unsaturated Polyester Resin (UPE)	--
Methyl Ethyl Ketone Peroxide Catalysis (MEKP)	1%
Cobalt Naphthenate Promoter (CN)	0.03%

A summary of the average mechanical properties of the material systems used in the material and structural (cellular beams and plates) characterization studies is presented in Table 2.2. The physical characteristics of the fiber types used for each material system, including fiber weight fraction, fiber volume fraction, fiber length, and aspect ratio, are provided in Table 2.3.

Table 2.2. Average properties of natural fiber and unsaturated polyester composites

Fiber type	*Fiber Volume Fraction* (%)	*Density* (g/cm^3)	*Elastic Modulus* (GPa)	*Tensile Strength* (MPa)
Green Hemp	10	1.18	3.81	14.47
Green Hemp	13	1.19	4.40	14.91
Green Hemp	20	1.22	5.23	16.79
Unprocessed Green Hemp	25	1.14	8.65	10.08
Raw Hemp	15	1.21	6.15	19.49
Flax	35	1.10	3.37	13.31
E-Glass	15	1.36	7.80	34.70

Table 2.3. Physical characteristics of the reinforcing fibers

Fiber Type	*Fiber Wt.* (%)	*Fiber Vol.* (%)	*Fiber Length* (mm)	*Fiber L/d*
Green Hemp	13	10	2 - 10	60
Green Hemp	17	13	2 - 10	60
Green Hemp	25	20	2 - 10	60
Unprocessed Green Hemp	25	25	5 - 20	125
Raw Hemp	20	15	8 - 12	100
Flax	33	35	1 - 2	15
E-Glass	29	15	6 - 8	467

2.3.2 Manufacturing

Characterization of the biocomposite material systems was done through ASTM testing of coupon samples taken from compression molded plates. The typical manufacturing process of the compression molded plates is summarized in the photograph sequence shown in Figure 2.9. The manufacturing process began by first preparing a 200 mm x 200 mm picture frame mold (Figure 2.9a), followed by top and bottom Teflon coated aluminum sheets, and top and bottom steel plates (Figure 2.9b). The fibers (Figure 2.9c) were dried in a vacuum oven at 80°C and 100 kPa of pressure for at least 10 hours before manufacturing. The polyester resin system (Figure 2.9d) shown in Table 2.1 was measured and mixed. The resin was then poured on the fibers (Figure 2.9e) and mixed by hand (Figure 2.9f) until the material was consistent. The impregnated fibers were then placed in the picture frame mold (Figure 2.9g). The natural fibers have a tendency to clump and tangle together when mixed. Thus, to ensure a uniform sample care must be taken to evenly distribute the material in the mold.

Once the impregnated fibers were placed in the mold, the top Teflon and steel plates were placed on top of the material. The entire mold was wrapped with aluminum foil to catch any resin that squeezed out of the sample during pressing. The sample was then placed in the press for curing under compression (Figure 2.9h). The sample was cured under 550 kPa of pressure for a total of 4 hours. During the 4 hour curing period the following temperatures were used: 100°C for 2 hours, followed by 150°C for 2 hours. Typical biocomposite compression molded plates and samples for material testing are shown in Figure 2.10.

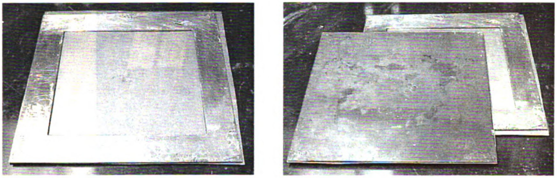

(a) Teflon coated picture frame mold

(b) Top steel plate

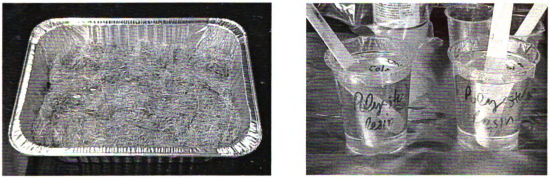

(c) Tray with hemp fibers

(d) Unsaturated polyester resin

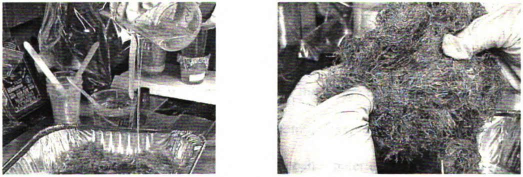

(e) Pour resin on fibers

(f) Mix fibers and resin by hand

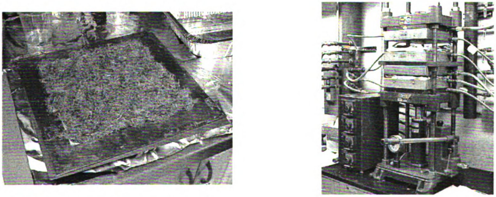

(g) Impregnated biofibers in mold

(h) Compression curing of sample

Figure 2.9. Manufacturing process of compression molded biocomposite plates

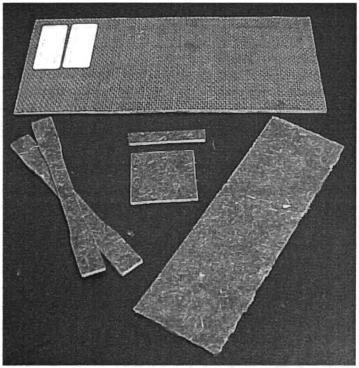

Figure 2.10. Compression molded biocomposite materials

2.3.3 Test Matrix

Material property tests were performed on the following reinforcing fiber types: green hemp, unprocessed green hemp, raw hemp, flax, and E-glass. Unsaturated polyester was used as the matrix for all the composite material systems. Each material type was given a sample identification label (ID) depending on the material and fiber weight fraction used. The first letter of the ID, P, stands for compression molded plate. The next two digits of the ID stand for the material type, as shown in Table 2.4. The final two digits stand for the fiber weight fraction used in the material. The physical characteristics of the fiber types used for each material system are provided in Table 2.5.

Table 2.4. Biocomposite material system naming convention

ID Label	*Fiber Type*	*Fiber Physical Description*
01	Green Hemp	short fibers, low core content
02	Unprocessed Green Hemp	long fibers, high core content
03	Raw Hemp	long fibers, low core content
04	Flax	short fibers, 50% fibers, 50% core
05	E-Glass	short chopped fibers, sized for polyester

Table 2.5. Physical characteristics of the composite material systems

SAMPLE	*ID*	*Fiber Wt. (%)*	*Fiber Vol. (%)*	*Density (g/cm^3)*
Green Hemp/UPE - 13 wt.%	P-01-13%	13	10	1.18
Green Hemp/UPE - 17 wt.%	P-01-17%	17	13	1.19
Green Hemp/UPE - 25 wt.%	P-01-25%	25	20	1.22
Unprocessed Green Hemp/UPE	P-02-25%	25	25	1.14
Raw Hemp/UPE	P-03-20%	20	15	1.21
Flax/UPE	P-04-33%	33	35	1.10
E-Glass/UPE	P-05-29%	29	15	1.36

2.3.4 Tensile Test Results

The tensile stress-strain response of each biocomposite material system was measured using ASTM D638 and used to determine the modulus of elasticity, ultimate tensile strength, and the elongation at break. The results for each of these tensile properties are presented in the following sections. The specific modulus and strength of the biocomposite material systems are presented at the end of the section.

2.3.4.1 Tensile Characteristic Values

A summary of the characteristic tensile properties including: modulus of elasticity (MOE), ultimate tensile strength, and elongation at break are shown in Table 2.6 for the biocomposite material systems. The results from each of these tensile properties are presented in detail and discussed in the following sections

Table 2.6. Tensile test results summary for biocomposite material systems

SAMPLE	*ID*	*MOE* (GPa)	*Tensile Str.* (MPa)	*Tensile Elong* (%)
Green Hemp/UPE - 13wt.%	P-01-13%	3.81	14.47	0.32
Green Hemp/UPE - 17wt.%	P-01-17%	4.40	14.91	0.30
Green Hemp/UPE - 25wt.%	P-01-25%	5.23	16.79	0.33
Unprocessed Green Hemp/UPE	P-02-25%	8.65	10.08	0.16
Raw Hemp/UPE	P-03-20%	6.15	19.49	0.33
Flax/UPE	P-04-33%	3.37	13.31	0.33
E-Glass/UPE	P-05-29%	7.80	34.70	0.50

2.3.4.2 Modulus of Elasticity

The results for the modulus of elasticity are given in Table 2.7 and shown in Figure 2.11. The test results show that, on average, the modulus of the E-glass material system was 1.5 times that of the biocomposite material systems (Table 2.7). However, the unprocessed green hemp material system, with a modulus of 8.65 GPa, showed a higher value than the E-glass material system, with a modulus of 7.80 GPa (Table 2.7). The raw hemp material system, with a modulus of 6.80 GPa, showed a modulus comparable to the E-glass material system. It should be noted that the E-glass fibers were sized (chemically treated for improved adhesion) for polyester resin (see Table 2.4, page 24), which may lead to improved properties for the E-glass material system.

The results from the green hemp material systems show increased modulus of elasticity with increase in fiber weight fraction. For example, as the fiber weight fraction of the green hemp material systems increased from 13% to 25%, the modulus increased from 3.81 GPa to 5.23 GPa, an increase of 37% (Table 2.7). This trend is expected, as the fibers are stiffer and stronger than the matrix material.

Table 2.7. Modulus of elasticity (MOE) test results for biocomposite material systems

SAMPLE	*ID*	*MOE* (GPa)	*Std. Dev.* (GPa)	*Coeff. of Variation*
Green Hemp/UPE - 13wt.%	P-01-13%	3.81	0.43	11%
Green Hemp/UPE - 17wt.%	P-01-17%	4.40	0.41	9%
Green Hemp/UPE - 25wt.%	P-01-25%	5.23	0.82	16%
Unprocessed Green Hemp/UPE	P-02-25%	8.65	2.80	32%
Raw Hemp/UPE	P-03-20%	6.15	1.12	18%
Flax/UPE	P-04-33%	3.37	0.24	7%
E-Glass/UPE	P-05-29%	7.80	1.29	17%

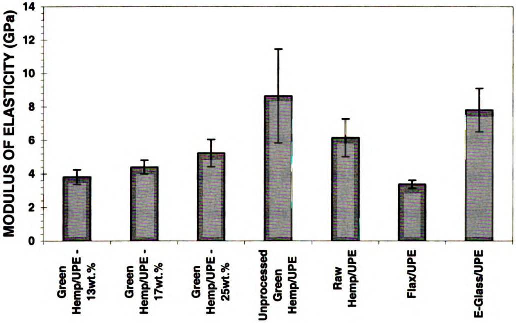

Figure 2.11. Modulus of elasticity (MOE) test results for biocomposite material systems

2.3.4.3 Ultimate Tensile Strength

The results for the ultimate tensile strength are provided in Table 2.8 and shown in Figure 2.12. Test results show that the strength of the E-glass material system was, on average, 2.3 times that of the biocomposite material systems (Table 2.8). As stated in the previous section, the E-glass fibers were sized for polyester resin (Table 2.4, page 24), which may lead to improved composite properties. Despite this fact, the strength of E-glass fibers are in general much stronger than natural fibers (see Table 1.1, page 4).

The results from the green hemp material systems show increased tensile strength with increase in fiber weight fraction. For example, as the fiber weight fraction of the green hemp material systems increased from 13% to 25%, the strength increased from 14.47 MPa to 16.79 MPa, an increase of 16% (Table 2.8). This trend is expected, as the fibers are stronger than the matrix material.

Results from the tensile strength tests have a high variation for most material systems, with coefficients of variation (standard deviation divided by mean value) ranging from 25% to 50% (Table 2.8). The variation in the results may be due to manufacturing defects on the surface of the compression molded plates, which may lead to premature tensile failure and cause scatter in the results. Variation may also be due to impurities, such as the wood like core material present in the natural fibers. These impurities may act as crack initiators or lead to poor fiber-matrix adhesion.

Table 2.8. Ultimate tensile strength (UTS) test results for biocomposite material systems

SAMPLE	*ID*	*Tensile Str. (MPa)*	*Std. Dev. (MPa)*	*Coeff. of Variation*
Green Hemp/UPE - 13wt.%	P-01-13%	14.47	5.74	40%
Green Hemp/UPE - 17wt.%	P-01-17%	14.91	5.67	38%
Green Hemp/UPE - 25wt.%	P-01-25%	16.79	4.19	25%
Unprocessed Green Hemp/UPE	P-02-25%	10.08	5.89	58%
Raw Hemp/UPE	P-03-20%	19.49	3.10	16%
Flax/UPE	P-04-33%	13.31	2.63	20%
E-Glass/UPE	P-05-29%	34.70	17.49	50%

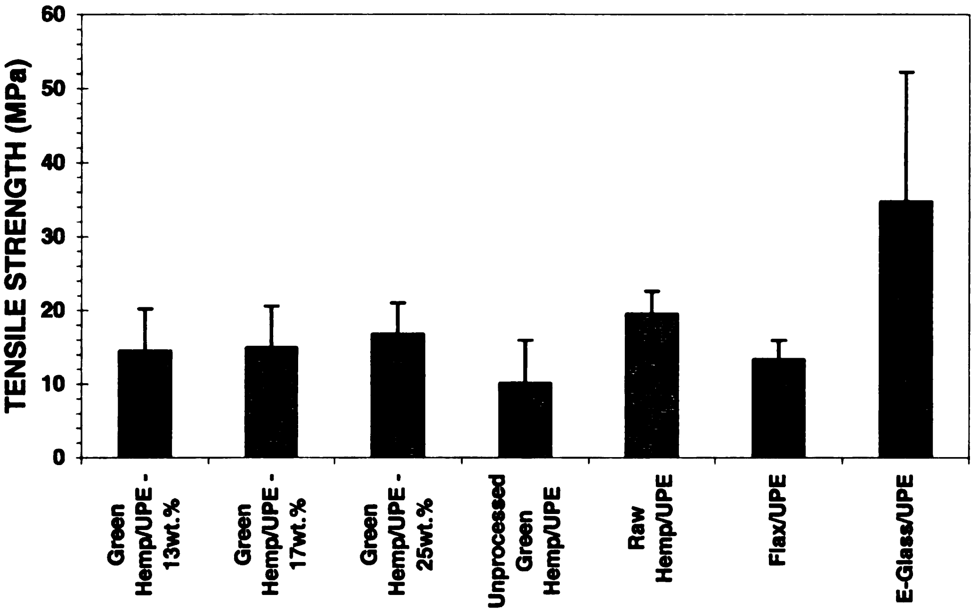

Figure 2.12. Ultimate tensile strength (UTS) test results for biocomposite material systems

2.3.4.4 Elongation at Break

Test results for the tensile elongation at break are provided in Table 2.9 and shown in Figure 2.13. The results from the elongation at break have a high variation for most material systems, with coefficients of variation ranging from 20-75% (Table 2.9). As with the ultimate tensile strength results, that variation in results may be due to manufacturing defects on the surface of the compression molded plates, which may lead to premature tensile failure and cause scatter in the results.

The test results show that the elongation at break for the E-glass material system was, on average, 1.5 times that of the biocomposite material systems (Table 2.9). The tensile elongation at break of the biocomposite material systems was very similar, with an average elongation at break of 0.32% (Table 2.9). However, the ultimate strain of the unprocessed green hemp material system was only half that of the other biocomposite material systems (Table 2.9).

Table 2.9. Tensile elongation at break test results for biocomposite material systems

SAMPLE	ID	Tensile Elong (%)	Std. Dev. (%)	Coeff. of Variation
Green Hemp/UPE - 13wt.%	P-01-13%	0.32	0.16	50%
Green Hemp/UPE - 17wt.%	P-01-17%	0.30	0.15	49%
Green Hemp/UPE - 25wt.%	P-01-25%	0.33	0.07	22%
Unprocessed Green Hemp/UPE	P-02-25%	0.16	0.12	75%
Raw Hemp/UPE	P-03-20%	0.33	0.07	20%
Flax/UPE	P-04-33%	0.33	0.16	47%
E-Glass/UPE	P-05-29%	0.50	0.21	41%

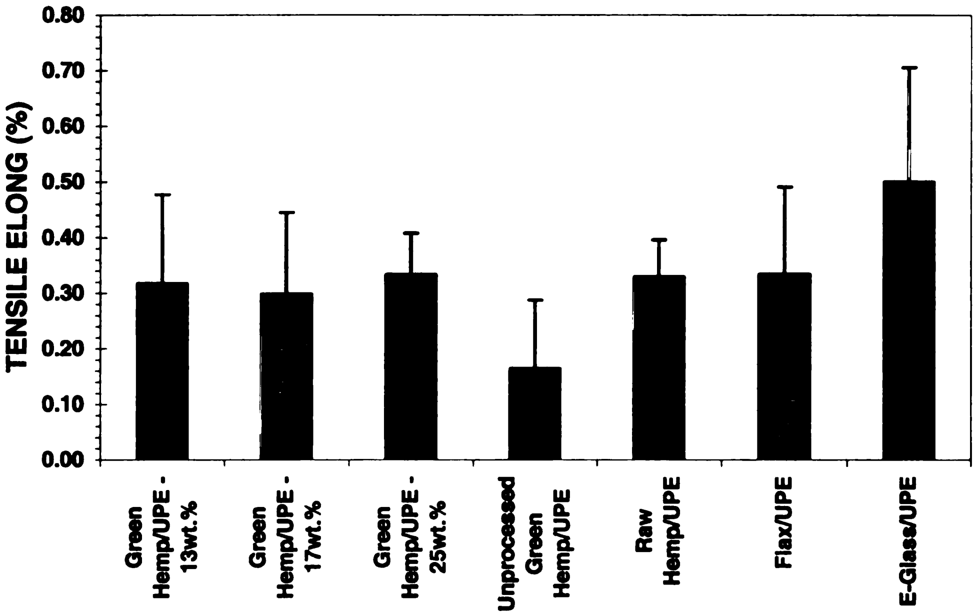

Figure 2.13. Tensile elongation at break test results for biocomposite material systems

2.3.4.5 Specific Tensile Properties

The specific tensile stiffness is provided in Table 2.10 and show in Figure 2.14, while the specific tensile strength is proved in Table 2.11 and shown in Figure 2.15.

Both the specific stiffness and strength show similar trends to the modulus of elasticity (Figure 2.11) and ultimate tensile strength (Figure 2.12). Because of the low fiber weight (and volume) fraction used for the E-glass material system, the density of the material is relatively low. Thus, the specific properties of the biocomposite material systems do not compare well with the tested E-glass material systems. If higher volume fractions were used for both the E-glass and biocomposite samples, improvement in specific properties of the biocomposite materials would have been more noticeable.

Table 2.10. Specific tensile stiffness of biocomposite material systems

SAMPLE	*ID*	*Density* (g/cm^3)	*MOE* (GPa)	*E/ρ* [$GPa/(g/cm^3)$]
Green Hemp/UPE - 13wt.%	P-01-13%	1.18	3.81	3.24
Green Hemp/UPE - 17wt.%	P-01-17%	1.19	4.40	3.69
Green Hemp/UPE - 25wt.%	P-01-25%	1.22	5.23	4.28
Unprocessed Green Hemp/UPE	P-02-25%	1.14	8.65	7.59
Raw Hemp/UPE	P-03-20%	1.21	6.15	5.07
Flax/UPE	P-04-33%	1.10	3.37	3.06
E-Glass/UPE	P-05-29%	1.36	7.80	5.74

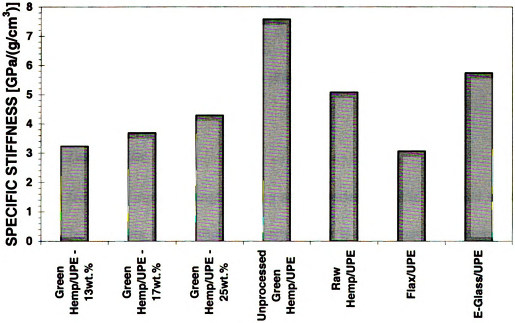

Figure 2.14. Specific tensile stiffness of biocomposite material systems

Table 2.11. Specific tensile strength of biocomposite materials systems

SAMPLE	*ID*	*Density* (g/cm^3)	*Tensile Str.* (MPa)	σ/ρ [MPa/(g/cm^3)]
Green Hemp/UPE - 13wt.%	P-01-13%	1.18	14.47	12.29
Green Hemp/UPE - 17wt.%	P-01-17%	1.19	14.91	12.51
Green Hemp/UPE - 25wt.%	P-01-25%	1.22	16.79	13.73
Unprocessed Green Hemp/UPE	P-02-25%	1.14	10.08	8.85
Raw Hemp/UPE	P-03-20%	1.21	19.49	16.07
Flax/UPE	P-04-33%	1.10	13.31	12.06
E-Glass/UPE	P-05-29%	1.36	34.70	25.51

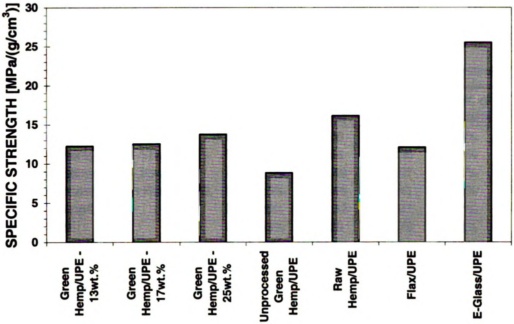

Figure 2.15. Specific tensile strength of biocomposite material systems

2.3.5 Impact Test Results

Results from the impact strength testing are provided in Table 2.12 and shown in Figure 2.16. The test data shows that, on average, the E-glass material system had an impact strength 5.6 times that of the bio composite material systems (Table 2.12).

The test results, excluding the E-glass material system, are shown in Figure 2.17 to better compare the results from the biocomposite materials. The results from the biocomposite material systems show increased impact strength with increase in fiber weight fraction. For example, as the fiber weight fraction of the green hemp material systems increased from 13% to 25%, the impact strength increased from 6.86 J/m to 10.40 J/m, an increase of 52% (Table 2.12). This trend of increasing impact strength with increased fiber weight fraction is expected as the fibers provide more impact strength than the matrix material. The flax biocomposite material system showed the lowest impact strength, at 5.28 J/m (Table 2.12), which may be due to the short fiber length and the 50% core material contained with the flax fibers.

Table 2.12. Impact strength (Izod Test) test results for biocomposite material systems

SAMPLE	*ID*	*Impact Str. (J/m)*	*Std. Dev. (J/m)*	*Coeff. of Variation*
Green Hemp/UPE - 13wt.%	P-01-13%	6.86	1.88	27%
Green Hemp/UPE - 17wt.%	P-01-17%	7.54	2.06	27%
Green Hemp/UPE - 25wt.%	P-01-25%	10.40	2.07	20%
Unprocessed Green Hemp/UPE	P-02-25%	17.45	3.41	20%
Raw Hemp/UPE	P-03-20%	13.52	5.01	37%
Flax/UPE	P-04-33%	5.28	0.76	14%
E-Glass/UPE	P-05-29%	67.29	7.55	11%

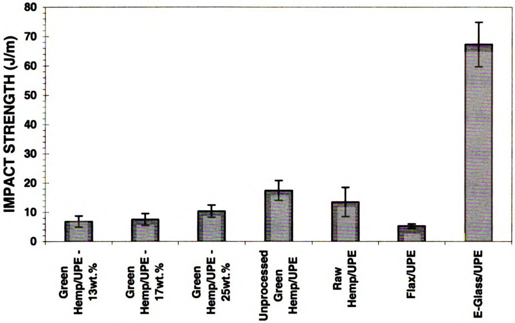

Figure 2.16. Impact strength (Izod Test) test results for biocomposite material systems

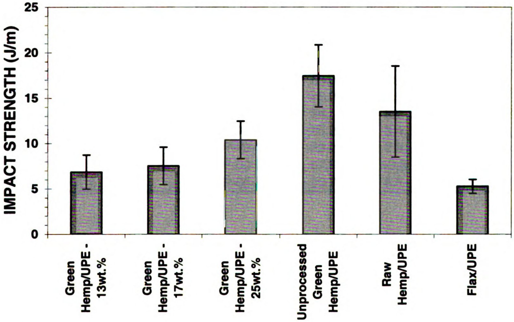

Figure 2.17. Impact strength (Izod Test) test results for biocomposite materials only

2.3.6 Thermal Expansion Test Results

Results from the coefficient of thermal expansion (CTE) tests are provided in Table 2.13 and shown graphically in Figure 2.18. The results from the CTE tests show that the biocomposite material systems, on average, have a CTE 30% higher than the E-glass material system (Table 2.13). In addition, the results from the green hemp material systems show that the CTE decreases as the fiber weight fraction increases (Table 2.13). For example, as the fiber weight fraction of the green hemp material systems increased from 13% to 25%, the CTE decreased from 51.0 μm/m°C to 34.1 μm/m°C, a decrease of 58% (Table 2.13). This trend verifies that the CTE of the matrix material is higher than that of the natural fibers, thus, the CTE of the composite material system can be reduced by increasing the content of natural fibers.

Table 2.13. Coefficient of thermal expansion (CTE) test results for biocomposite material systems

SAMPLE	*ID*	*CTE* (μm/m°C)	*Std. Dev.* (μm/m°C)	*Coeff. of Variation*
Green Hemp/UPE - 13wt.%	P-01-13%	59.0	10.7	18%
Green Hemp/UPE - 17wt.%	P-01-17%	45.0	7.2	16%
Green Hemp/UPE - 25wt.%	P-01-25%	34.1	3.4	10%
Unprocessed Green Hemp/UPE	P-02-25%	35.2	3.4	10%
Raw Hemp/UPE	P-03-20%	23.2	2.8	12%
Flax/UPE	P-04-33%	67.6	10.8	16%
E-Glass/UPE	P-05-29%	30.7	8.8	29%

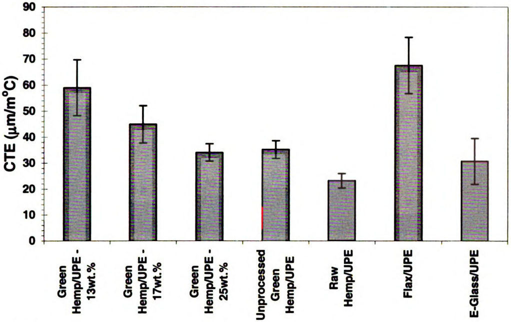

Figure 2.18. Coefficient of thermal expansion (CTE) test results for biocomposite material systems

The CTE of the green hemp material system with a fiber weight fraction of 25% is compared with conventional building materials in Figure 2.19. The comparison shows that the CTE of the biocomposite material is approximately 3 times larger than that of steel, and concrete (Figure 2.19). This difference in CTE of the biocomposite material system with conventional construction materials, and the resulting differential thermal effects, must be considered if biocomposite materials are used with conventional building materials for structural applications.

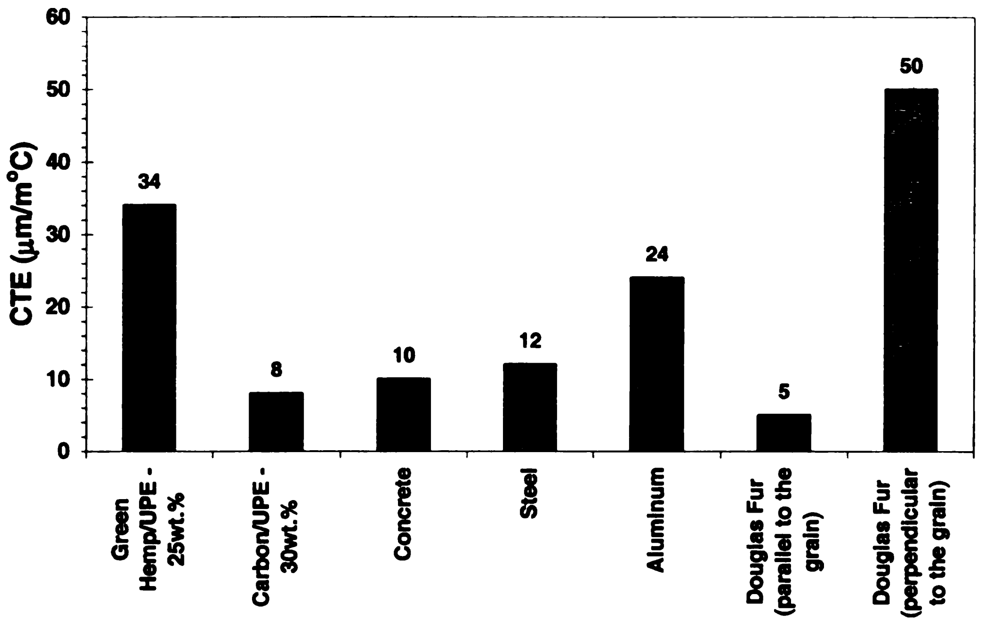

Figure 2.19. Comparison of Coefficient of thermal expansion (CTE) with conventional materials

2.3.7 Moisture Absorption Test Results

The moisture absorption test results are given in Table 2.14 and shown in Figure 2.20. The moisture absorbed by the material systems was measured over a period of 50 days as show in the plot of percent weight absorbed versus the square root of time in Figure 2.21. The moisture absorption of all material systems stabilized after approximately 33 days (800 hours) in the environmental chamber.

Results from the moisture absorption test show that the biocomposite material systems, on average, absorbed 4 times as much moisture as the E-glass material system (Table 2.14). In addition, the results from the green hemp material systems show that moisture absorption increases as the fiber weight fraction increases (Table 2.14). For example, as the fiber weight fraction of the green hemp material systems increased from 13% to 25%, the moisture absorption increased from 0.96% to 1.31%, an increase of 36%

(Table 2.14). This trend is expected as the fibers absorb more moisture than the matrix material. The trend of increasing moisture absorption with increasing fiber weight fraction is also seen with other material systems. For example, the raw hemp material with a fiber weight fraction of 20% absorbed 1.37% moisture, while the unprocessed green hemp material with a fiber weight fraction of 25% absorbed 1.44%, and the flax material with a fiber weight fraction of 33% absorbed 1.71% (Table 2.14).

The results from the moisture absorption test also show that the biocomposite material systems absorb less moisture than the natural fiber constituents. The hemp biocomposite material systems (green, unprocessed, and raw) absorbed between 0.96% to 1.44% moisture, while the hemp fibers alone absorb 8% moisture (see Table 1.1). The flax biocomposite material system absorbed 1.71% moisture, while the flax fibers alone absorb 7% moisture (see Table 1.1). This trend suggests that the matrix material acts as a moisture barrier and helps reduce the moisture absorbed by the composite material system.

Table 2.14. Moisture absorption test results for biocomposite material systems

SAMPLE	*ID*	Moisture *Absorption (%)*	*Std. Dev. (%)*	*Coeff. of Variation*
Green Hemp/UPE - 13wt.%	P-01-13%	0.96%	0.03%	3%
Green Hemp/UPE - 17wt.%	P-01-17%	1.05%	0.06%	6%
Green Hemp/UPE - 25wt.%	P-01-25%	1.31%	0.04%	3%
Unprocessed Green Hemp/UPE	P-02-25%	1.44%	0.08%	6%
Raw Hemp/UPE	P-03-20%	1.37%	0.21%	15%
Flax/UPE	P-04-33%	1.71%	0.09%	5%
E-Glass/UPE	P-05-29%	0.34%	0.02%	6%

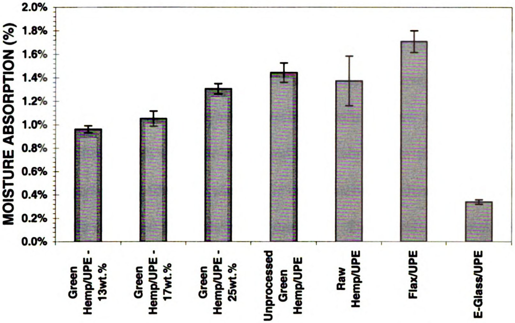

Figure 2.20. Moisture absorption test results for biocomposite material systems

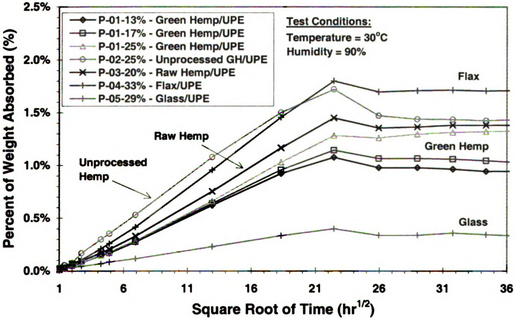

Figure 2.21. Percent weight absorbed versus square root of time for biocomposite material systems

2.4 Hybrid Material Systems

Improvement of the structural performance of biocomposite material systems and cellular structures through the use of hybrid material systems was investigated at both the material and structural level. A hybrid material is defined here as combination of chopped natural fibers with synthetic or natural fiber fabrics. In the hybrid material system the chopped natural fibers are used as the core material, sandwiched between face sheets of synthetic or natural fiber fabrics (Figure 2.22). These hybrid material systems could be used as face sheet, or cell wall materials in cellular beams and plates. The use of fabric face sheets also improves the ability to handle the natural fibers during manufacturing. Thus, the hybrid material systems are ideal for use as pre-forms for automated manufacturing.

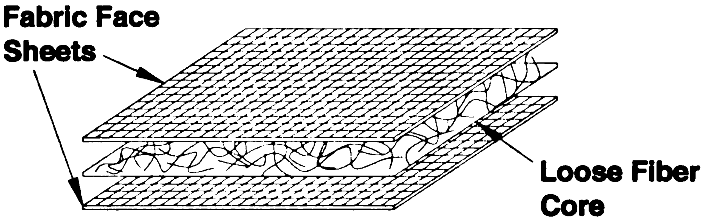

Figure 2.22. Hybrid material system

In addition, single composite laminates using chopped strand E-glass, unidirectional carbon, and woven jute mats were investigated to provide the necessary material characterization for the face sheet materials used in the structural experimental studies (Chapter 3). These material systems were only tested for tensile properties.

2.4.1 Materials and Constituents

Two types of fiber fabrics (Figure 2.23) were used for the hybrid material systems: (a) randomly oriented glass, and (b) woven jute. These fabrics, along with unidirectional carbon (Figure 2.23c), were considered as face sheet materials for hybrid cellular plates (see Chapter 3). Engineered hybrid fabric/biofiber blends for the hybrid material systems consisted of: (a) top and bottom chopped glass strand mat face sheets with raw hemp fiber core, and (b) top and bottom woven jute fabric with a raw hemp fiber core. The woven jute hybrid composite material contained 60% core fibers by total fiber weight in the sample, while the glass strand mat hybrid material contained 51% core fibers by total fiber weight. Both hybrid materials were manufactured with a fiber weight fraction of 15%. Due to resin squeeze-out during pressing, the actual fiber weight fraction was higher than 15%. The measured fiber weight fraction of the jute hybrid material was 27%, while the glass strand mat hybrid material was 31% (Table 2.15). The resin system used was unsaturated polyester (UPE), as shown in Table 2.1.

The composite systems for single natural and synthetic fabrics (Figure 2.23) were composed of one layer of fabric material and unsaturated polyester (UPE). The fabric material systems were manufactured with a fiber weight fraction of 30% to match the estimated face sheet material composition used in the structural experimental studies (Chapter 3).

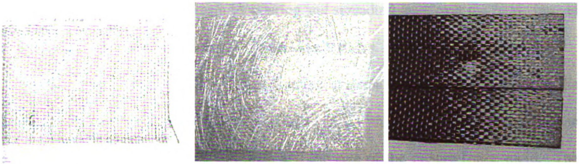

(a) Woven jute (b) Randomly orientated glass (c) Unidirectional carbon

Figure 2.23. Fiber mat fabrics used as face sheets for hybrid material systems

Table 2.15. Average properties of the hybrid material systems with biocomposite and E-glass material systems

SAMPLE	*Fiber Weight Fraction*	Density (g/cm^3)	*MOE* (GPa)	*Tensile Str.* (MPa)
Green Hemp/UPE T&B Jute	27%	1.17	10.78	28.19
Green Hemp/UPE T&B Glass	31%	1.29	11.92	43.37
Green Hemp	25%	1.22	5.23	16.79
E-glass	29	1.36	7.8	34.7

2.4.2 Manufacturing

The characterization of the hybrid material systems was done by manufacturing compression molded plates of sandwiched material systems as well as composite systems of the individual natural and synthetic fabrics. The typical manufacturing process of the hybrid compression molded plates is summarized in the photograph sequence shown in Figure 2.24. The manufacturing of the hybrid material systems was very similar to the biocomposite compression molded plates (Figure 2.9) with the only difference being that face sheets were used for the hybrid material systems. The face sheets were added to the system by placing a bottom layer of fabric (Figure 2.24d), followed by the impregnated chopped hemp fiber core (Figure 2.24e), and then the top face sheet (Figure 2.24f). The face sheets were wet out with resin by pouring and spreading resin over the fabric instead of the hand mixing used to wet out the loose natural fibers.

The manufacturing of the fabric material systems was also very similar to the biocomposite compression molded plates (Figure 2.9), with the only differences being the procedure for mixing the fibers and resin and the size of the picture frame mold. The fibers and resin were mixed by simply pouring and spreading the resin over the fibers (Figure 2.24d). A smaller 178mm x 127 mm picture frame mold was used because the fabric material systems were only tested in tension. Thus, a smaller amount of material was required for the test specimens.

All the hybrid material system plates were cured under 550 kPa of pressure for a total of 4 hours. During the 4 hours the following temperatures were used: 100°C for 2 hours, followed by 150°C for 2 hours.

The two hybrid compression molded plates manufactured for the experimental program are shown in Figure 2.25. The compression molded plates of the fiber mat materials are shown in Figure 2.26.

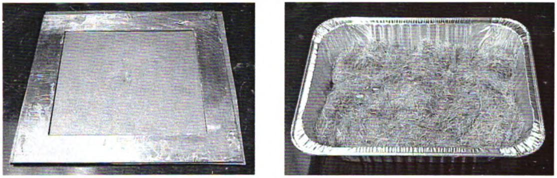

(a) Teflon coated picture frame mold (b) Tray with hemp fibers

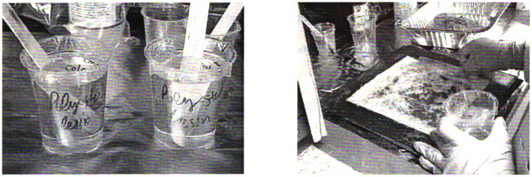

(c) Unsaturated polyester resin (d) Wet-out of bottom mat layer

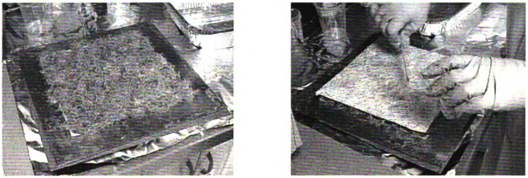

(e) Placement of hemp fibers (f) Wet out of bottom mat layer

(g) Hybrid fabric/biofiber blend (h) Compression curing of sample

Figure 2.24. Manufacturing process of compression molded hybrid plates

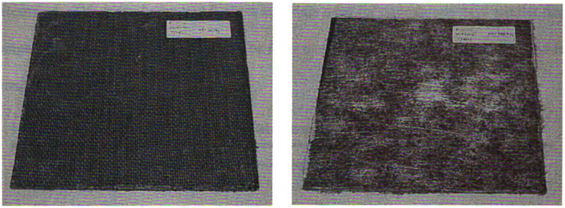

(a) Hemp core with jute fabric face sheets (b) Hemp core with glass strand mat face sheets

Figure 2.25. Hybrid compression molded plates

(a) Unidirectional Carbon (b) Randomly orientated E-glass (c) Woven jute

Figure 2.26. Compression molded plates of fiber mat materials and polyester resin

2.4.3 Test Matrix

Each material type tested was given a sample identification label (ID) depending on the material type and the fiber weight fraction used as shown in Table 2.16. The first letter of the ID, P, stands for compression molded plate. The next two digits of the ID stand for the material type. The final two digits stand for the sample number of the particular material type. The results from the previous green hemp and E-glass material tests are used for comparison with the results from the hybrid plates throughout this discussion. The green hemp and E-glass materials used for comparison have similar fiber weight fractions to the hybrid plates. The fiber mat material systems were only tested for tensile properties.

Table 2.16. Hybrid material system plate naming convention

ID Label	*Plate Type*	*Constituents*
11	Hybrid plate	Top and bottom glass face sheets With green hemp core
31	Hybrid plate	Top and bottom jute fabric face sheets With green hemp core
10	Randomly orientated glass strand mat	Randomly orientated glass strand mat
20	Unidirectional carbon fiber mat	Unidirectional carbon with nylon stitching
30	Woven jute fabric mat	Woven jute fabric

2.4.4 Tensile Test Results

The tensile stress-strain response of each hybrid material system was measured using ASTM D638 and used to determine the modulus of elasticity, ultimate tensile strength, and the elongation at break. The results for each of these tensile properties are presented in the following sections. The specific modulus and strength of the hybrid material systems are presented at the end of the section.

2.4.4.1 Tensile Characteristic Values

A summary of the characteristic tensile properties for the hybrid material systems including modulus of elasticity (MOE), ultimate tensile strength, and elongation at break are shown in Table 2.17. The results from each of these tensile properties are presented in detail and discussed in the following sections.

Table 2.17. Tensile test results summary for hybrid material systems

SAMPLE	*ID*	*MOE* (GPa)	*Tensile Str.* (MPa)	*Tensile Elong* (%)
Green Hemp/UPE T&B Jute - 27 wt.%	P-31-02	10.78	28.19	0.39
Green Hemp/UPE T&B Glass - 31 wt.%	P-11-02	11.92	43.37	0.61
Green Hemp/UPE - 25 wt.%	P-01-25%	5.23	16.79	0.33
E-Glass/UPE - 29 wt.%	P-05-29%	7.80	34.70	0.50
Glass Strand Mat/UPE	P-10-01	13.46	67.02	0.91
Unidirectional Carbon/UPE	P-20-01	37.92	585.12	1.67
Woven Jute/UPE	P-30-01	4.03	22.01	0.68

2.4.4.2 Modulus of Elasticity

Results for the modulus of elasticity are given in Table 2.18 and shown in Figure 2.27 and Figure 2.28. The addition of the fabric face sheets in the hybrid material systems clearly improved the modulus of elasticity over the solid material systems (Figure 2.27). By adding jute fabric face sheets to the hemp core the modulus was increased by 106% over the all hemp material, and by adding glass fabric face sheets the modulus was increased by 128% over the all-hemp sample (Table 2.18). The glass hybrid material system also showed an improvement in the modulus of 53% over the all-glass material (Table 2.18). Despite these improvements in modulus, the hybrid material systems have more deviation in the results compared to the all-biocomposite material plates (Table 2.18). This may be due to voids in the green hemp core material from non-uniform placement of the material during manufacturing.

The unidirectional carbon fabric material system showed by far the highest modulus of the face sheet fabric material systems (Figure 2.28). The modulus of the carbon fabric material system was 2.8 times the modulus of the glass fabric material, and 9.4 times the modulus of the jute fabric material (Table 2.18).

Table 2.18. Modulus of elasticity (MOE) test results for hybrid material systems

SAMPLE	*ID*	*MOE (GPa)*	*Std. Dev. (GPa)*	*Coeff. of Variation*
Green Hemp/UPE T&B Jute - 27 wt.%	P-31-02	10.78	6.12	57%
Green Hemp/UPE T&B Glass - 31 wt.%	P-11-02	11.92	7.30	61%
Green Hemp/UPE - 25 wt.%	P-01-25%	5.23	0.82	16%
E-Glass/UPE - 29 wt.%	P-05-29%	7.80	1.30	17%
Glass Strand Mat/UPE	P-10-01	13.46	10.74	80%
Unidirectional Carbon/UPE	P-20-01	37.92	3.69	10%
Woven Jute/UPE	P-30-01	4.03	0.64	16%

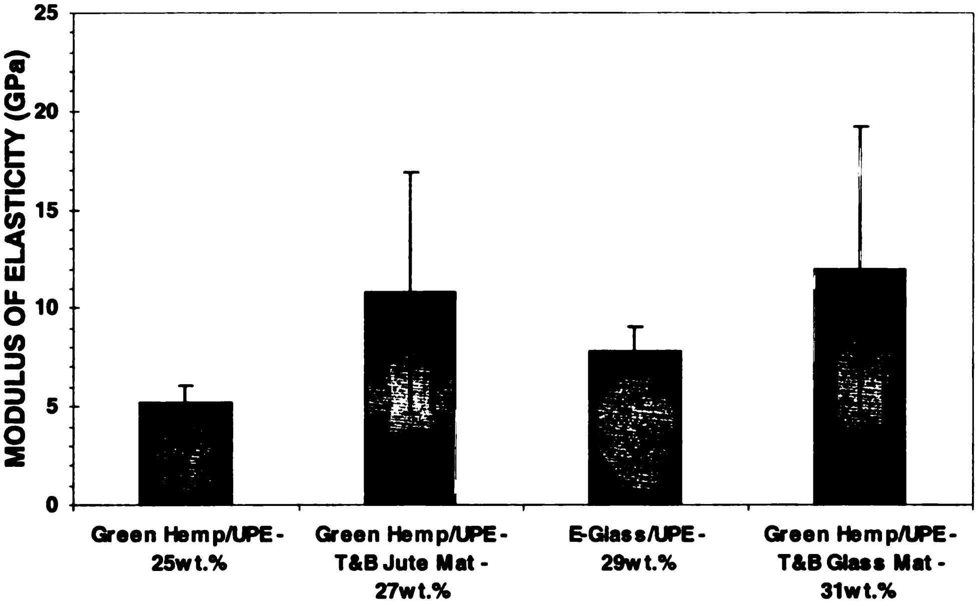

Figure 2.27. Modulus of elasticity (MOE) test results for hybrid material systems

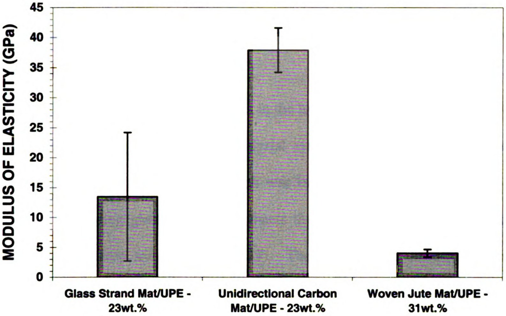

Figure 2.28. Modulus of elasticity (MOE) test results for face sheet material systems

2.4.4.3 Ultimate Tensile Strength

The results for the ultimate tensile strength are provided in Table 2.19 and shown in Figure 2.29 and Figure 2.30. When loaded up to failure in tension the two hybrid material systems failed in different manners. The jute hybrid material system failed in a sudden brittle manner, with complete fracture of the material and little noise from fiber cracking before failure. The glass hybrid material system also failed in a brittle manner, but with partial fracture of the material and fiber cracking noise before failure. At failure, the hemp core fractured, while the glass fibers in the face sheets had began to pull out of the matrix but did not completely fracture.

The face sheet fabric material systems also failed in different manners under tensile loading. Both the glass and jute fabric material systems failed in a sudden brittle mode with noise from fiber cracking near failure. The unidirectional carbon material system failed in a gradual manner, with considerable matrix cracking and debonding near failure. The matrix cracking was accompanied by loud cracking noises and an explosive noise at failure.

The addition of the fabric face sheets in the hybrid material systems improved the ultimate tensile strength over the solid material systems. By adding jute fabric face sheets to the hemp core the tensile strength was increased by 68% over the all-hemp material, and by adding glass fabric face sheets the tensile strength was increased by 158% over the all-hemp sample (Table 2.19). The glass hybrid material system also showed an improvement in tensile strength of 25% over the all-glass material (Table 2.19).

Table 2.19. Ultimate tensile strength (UTS) test results for hybrid material systems

SAMPLE	*ID*	*Tensile Str.* (MPa)	*Std. Dev.* (MPa)	*Coeff. of Variation*
Green Hemp/UPE T&B Jute - 27% wt.	P-31-02	28.20	4.5	16%
Green Hemp/UPE T&B Glass - 31% wt.	P-11-02	43.4	3.3	8%
Green Hemp/UPE - 25 wt.%	P-01-25%	16.79	4.19	25%
E-Glass/UPE - 29 wt.%	P-05-29%	34.70	17.49	50%
Glass Strand Mat/UPE	P-10-01	67.0	12.2	18%
Unidirectional Carbon/UPE	P-20-01	585.1	152.8	26%
Woven Jute/UPE	P-30-01	22.0	1.3	6%

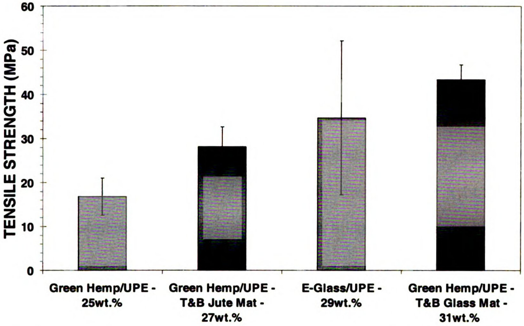

Figure 2.29. Ultimate tensile strength (UTS) test results for hybrid material systems

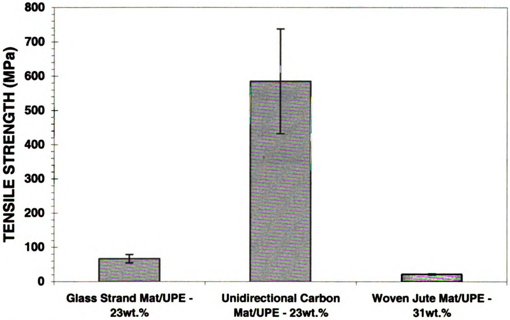

Figure 2.30. Ultimate tensile strength (UTS) test results for face sheet material systems

2.4.4.4 Elongation at Break

Results for the tensile elongation at break are provided in Table 2.20 and shown in Figure 2.31 and Figure 2.32. The hybrid material systems showed improvement in elongation at break compared to the hemp and glass material systems, with trends similar to the results shown for the modulus of elasticity and ultimate tensile strength. The increase in both the elongation at break and tensile strength of the hybrid material systems may be attributable to the face sheet materials bridging and preventing cracks in the hemp core material, which lead to sudden crack propagation and failure. The elongation at break of the hybrid materials show a high variation (Table 2.20), which, as previously described, may be due to manufacturing defects in the samples.

Table 2.20. Tensile elongation at break test results for hybrid material systems

SAMPLE	*ID*	*Tensile Elong (%)*	*Std. Dev. (%)*	*Coeff. of Variation*
Green Hemp/UPE T&B Jute - 27% wt.	P-31-02	0.39	0.24	60%
Green Hemp/UPE T&B Glass - 31% wt.	P-11-02	0.61	0.32	53%
Green Hemp/UPE - 25 wt.%	P-01-25%	0.33	0.07	22%
E-Glass/UPE - 29 wt.%	P-05-29%	0.50	0.21	41%
Glass Strand Mat/UPE	P-10-01	0.91	0.60	66%
Unidirectional Carbon/UPE	P-20-01	1.67	0.11	6%
Woven Jute/UPE	P-30-01	0.68	0.07	11%

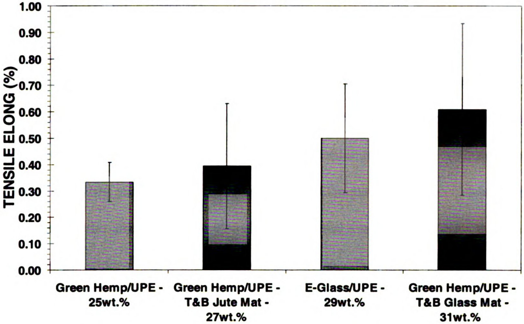

Figure 2.31. Tensile elongation at break test results for hybrid material systems

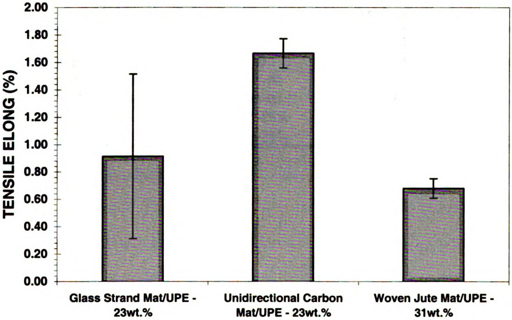

Figure 2.32. Tensile elongation at break test results for face sheet material systems

2.4.4.5 Specific Tensile Properties

Specific tensile stiffness values are provided in Table 2.21 and shown graphically in Figure 2.33, while specific tensile strengths are proved in Table 2.22 and shown in Figure 2.34. The hybrid material systems showed higher specific stiffness and specific strength (Table 2.21 and Table 2.22) with trends similar to the results shown for the modulus of elasticity and ultimate tensile strength. Comparing the two hybrid material systems, the specific strength of the glass/hemp material system was higher than that of the jute material system (Table 2.22). However, the specific stiffness of the jute hybrid material system was equal to the specific stiffness of the glass hybrid material system (Table 2.21). This shows the improved performance that can be achieved with the use of natural fiber reinforcement in place of synthetic fiber reinforcement.

Table 2.21. Specific tensile stiffness of hybrid material systems

SAMPLE	*ID*	*Density* (g/cm^3)	*MOE* (GPa)	*E/ρ* [$GPa/(g/cm^3)$]
Green Hemp/UPE T&B Jute - 27 wt.%	P-31-02	1.17	10.78	9.22
Green Hemp/UPE T&B Glass - 31 wt.%	P-11-02	1.29	11.92	9.21
Green Hemp/UPE - 25 wt.%	P-01-25%	1.22	5.23	4.28
E-Glass/UPE - 29 wt.%	P-05-29%	1.36	7.80	5.74

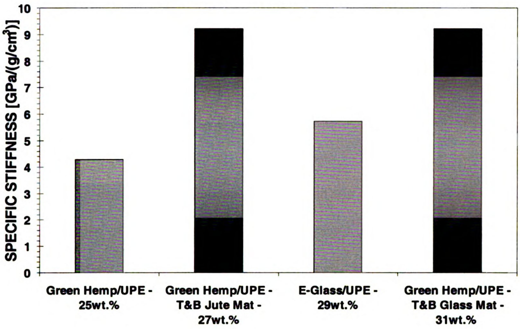

Figure 2.33. Specific tensile stiffness of hybrid material systems

Table 2.22. Specific tensile strength of hybrid materials systems

SAMPLE	*ID*	*Density* (g/cm^3)	*Tensile Str.* (MPa)	σ/ρ [MPa/(g/cm^3)]
Green Hemp/UPE T&B Jute - 27 wt.%	P-31-02	1.17	28.19	24.11
Green Hemp/UPE T&B Glass - 31 wt.%	P-11-02	1.29	43.37	33.51
Green Hemp/UPE - 25 wt.%	P-01-25%	1.22	16.79	13.73
E-Glass/UPE - 29 wt.%	P-05-29%	1.36	34.70	25.51

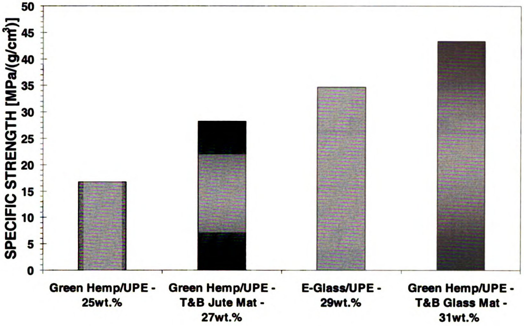

Figure 2.34. Specific tensile strength of hybrid materials systems

2.4.5 Impact Test Results

Impact strength test results are provided in Table 2.23 and shown in Figure 2.35. The hybrid material systems showed improved impact strength over the all-hemp and all-glass material systems (Table 2.23). By adding jute fabric face sheets to the hemp core the impact strength was increased by 9% over the all-hemp material, while the impact strength was increased by 86% by adding glass fabric face sheets (Table 2.23). The glass/hemp hybrid material system also showed an improvement in tensile strength of 7% over the all-glass material (Table 2.23). The increase in impact strength of the glass hybrid material system over the all-glass material system may be due to the longer length of fibers used in the glass strand fabric.

Table 2.23. Impact strength (notched Izod) test results for hybrid material systems

SAMPLE	*ID*	*Impact Str.* (J/m)	*Std. Dev.* (J/m)	*Coeff. of Variation*
Green Hemp/UPE T&B Jute - 27% wt.	P-31-02	11.28	2.57	23%
Green Hemp/UPE T&B Glass - 31% wt.	P-11-02	72.11	7.82	11%
Green Hemp/UPE 25 wt.%	P-01-25%	10.40	2.07	20%
E-Glass/UPE 29 wt.%	P-05-29%	67.29	7.55	11%

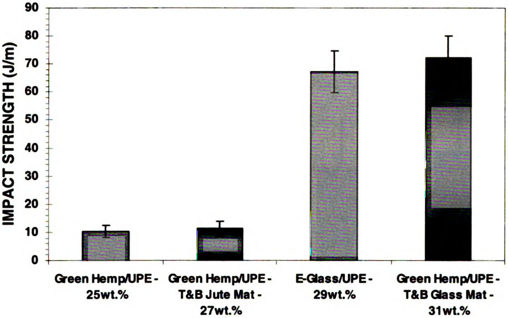

Figure 2.35. Impact strength (notched Izod) test results for hybrid material systems

2.4.6 Thermal Expansion Test Results

Results from the coefficient of thermal expansion (CTE) tests are provided in Table 2.24 and shown in Figure 2.36. In general, the hybrid material systems showed little or no difference in CTE compared to the all-hemp and all-glass material systems. The jute hybrid material systems show no difference in the CTE compared to the all-hemp material system (Table 2.24), which may be due to the hemp fibers and jute fibers having similar CTE values. The glass hybrid material system showed an increase in CTE over the all-glass material system (10%, Table 2.24), which may be due to the core hemp fibers having a larger CTE than the glass fabric fibers.

Table 2.24. Coefficient of thermal expansion (CTE) test results for hybrid material systems

SAMPLE	*ID*	*CTE (μm/m°C)*	*Std. Dev. (μm/m°C)*	*Coeff. of Variation*
Green Hemp/UPE T&B Jute - 27% wt.	P-31-02	33.38	4.86	15%
Green Hemp/UPE T&B Glass - 31% wt.	P-11-02	33.93	8.15	24%
Green Hemp/UPE - 25% wt.	P-01-25%	34.10	3.37	10%
E-Glass/UPE - 29% wt.	P-05-29%	30.73	8.81	29%

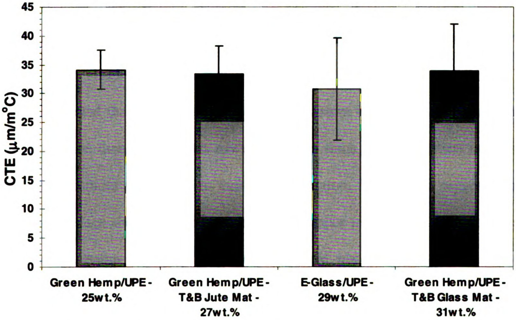

Figure 2.36. Coefficient of thermal expansion (CTE) test results for hybrid material systems

2.4.7 *Moisture Absorption Test Results*

Moisture absorption test results are given in Table 2.25 and shown in Figure 2.27. The moisture absorbed by the material system was measured over a period of 50 days, as shown in the plot of percent weight absorbed versus the square root of time in Figure

2.38. The moisture absorption of all material systems stabilized after approximately 30 days (675 hours) in the environmental chamber.

Moisture absorption for the jute hybrid material system was 1.25%, while the absorption of the all-hemp material system was 1.31% (Table 2.25). Thus, the results from the absorption tests show that the jute hybrid material system had little effect on moisture absorption (Figure 2.27). However, the glass hybrid material system showed a much lower moisture absorption than the all-hemp material system (Figure 2.27). The moisture absorption of the glass hybrid material system was 0.41%, while the all-hemp material system was 1.31% (Table 2.25). Results for the glass hybrid material were more comparable to the all-glass material system with a moisture absorption of 0.34% (Table 2.25). It is expected that the glass hybrid material system would have a slightly larger moisture absorption than the all-glass material system since the hemp fibers used in the hybrid system are more susceptible to moisture absorption. The results suggest that the use of glass-fiber face sheets, which have higher resistance to moisture absorption, act as a barrier for the hemp fibers in the core the hybrid material system. This hybrid arrangement of material is thus efficient for reducing moisture absorption in the biocomposite core material system.

Table 2.25. Moisture absorption test results for hybrid material systems

SAMPLE	*ID*	Moisture *Absorption (%)*	*Std. Dev. (%)*	*Coeff. of Variation*
Green Hemp/UPE T&B Jute - 27wt.%	P-31-02	1.25%	0.06%	5%
Green Hemp/UPE T&B Glass - 31wt.%	P-11-02	0.42%	0.05%	12%
Green Hemp/UPE - 25wt.%	P-01-25%	1.31%	0.04%	3%
E-Glass/UPE - 29wt.%	P-05-29%	0.34%	0.02%	6%

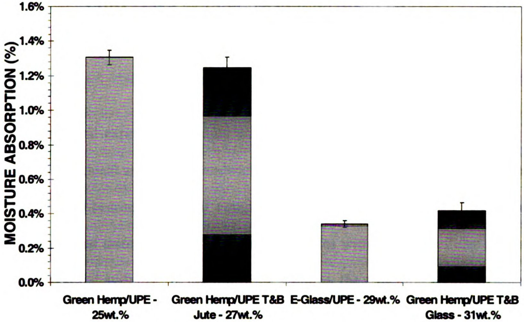

Figure 2.37. Moisture absorption test results for hybrid material systems

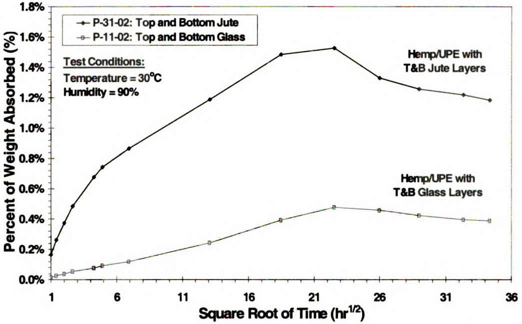

Figure 2.38. Percent weight absorbed versus square root of time for hybrid material systems

CHAPTER 3 CELLULAR BEAMS AND PLATES

3.1 Overview

A structural experimental study was conducted with the aim of developing and evaluating hierarchical and hybrid sandwich structures that would allow biocomposites to be used for load-bearing structural components. The studies included development, manufacturing, and testing of cellular beams and plates with varying cellular topologies and hybrid material systems. In the following sections, the structural forms investigated in the experimental studies are described, followed by the manufacturing and testing of the test units. The results of the flexural tests are provided with emphasis on comparing the performance of the various structural forms investigated in this study. The chapter is concluded with an experimental comparison of wood materials with the biocomposite cellular beams and plates tested in this study.

3.2 Structural Forms

Three types of high-performance structural forms were investigated for the structural experiments: (i) cellular sandwich structures, (ii) hierarchical cellular structures, and (iii) hybrid cellular structures. A brief description of each structural form is provided in the following sections.

3.2.1 Cellular Sandwich Structures

A sandwich structure is typically a low-density core material sandwiched between two high modulus face sheets to produce a lightweight panel with excellent stiffness (Allen 1969). The face sheets act like the flanges of an I-beam carrying the tensile and compressive loads due to bending, while the core acts like the web of an I-beam carrying the shear loads. The core material provides the panel thickness, and is typically made of a cellular structure to minimize the weight of the panel. The thicker the core of the panel, the higher the stiffness and strength for minimum weight gain. These conceps of cellular and sandwich structures are thus used to provide an efficient material arrangement for biocomposite structures.

The most important characteristic of a cellular structure affecting its mechanical properties is its *relative density*, ρ^*/ρ_s, i.e. the density of the cellular material, ρ^*, divided by the density of the solid from which the cells are made, ρ_s. This concept will be discussed further in the analytical studies chapter (Chapter 4). However, the relative density is used in this chapter to distinguish between the different cellular structures studied in the experimental program.

In the structural experimental program, sandwich beams and plates with cellular cores were investigated. A cellular core comprised of circular periodic cells in the longitudinal direction of the structure (Figure 3.1) was selected for the cellular beams and plates based on a similar study by Huang and Gibson (1995).

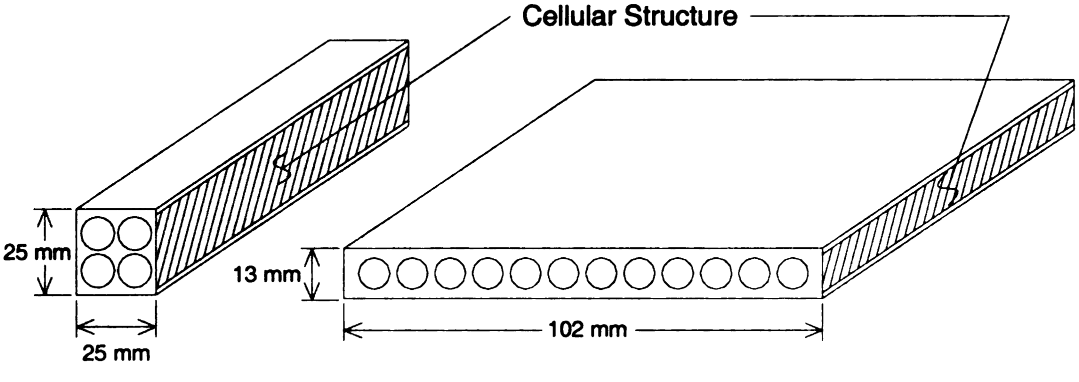

Figure 3.1. Periodic cellular sandwich bema and plate

3.2.2 Hierarchical Cellular Structures

The concept of hierarchical cellular structures, which is commonly found in nature, can be used to further increase the stiffness and efficiency of a cellular sandwich structure (Gunderson and Thorp 1993). Hierarchical cellular structures are complex microstructures that are designed to place material where most needed, i.e. in areas of high stress, and which feature multiple levels of embedded complexity in their geometric or material morphology. For structures primarily subjected to bending loads, the material in the section is most densely arranged near the top and bottom of the section where the stresses are high, and less densely arranged near the center of the section where the stresses are low.

The hierarchical cellular structures developed for the structural experimental program consisted circular cells, in the longitudinal direction of the structure, arranged in varying sizes through the depth of the structure (Figure 3.2).

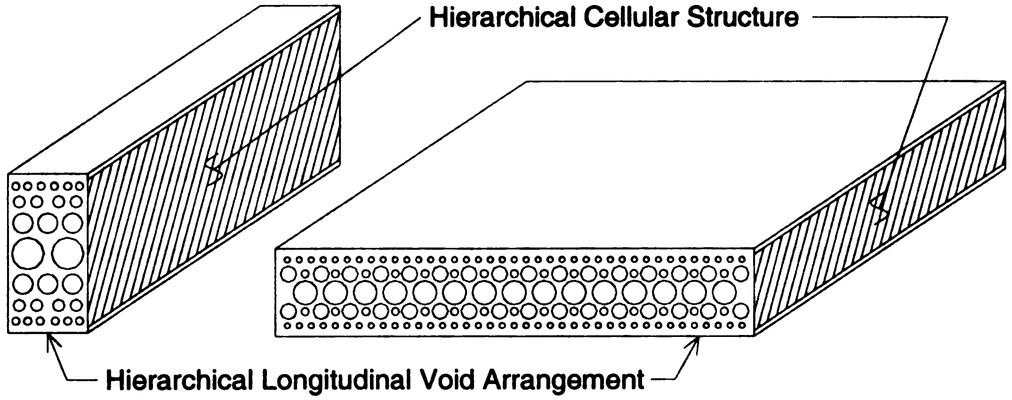

Figure 3.2. Hierarchical cellular sandwich beam and plate

3.2.3 Hybrid Cellular Structures

The hybrid cellular structures investigated in the structural experimental program were either cellular sandwich structures, or hierarchical cellular structures with integral bottom, or top and bottom, face sheets (Figure 3.3). The face sheets used consisted of natural and synthetic fiber mats, as described in the material experimental program of Chapter 2. The face sheets were integrally cured with the cellular structure to avoid delamination problems.

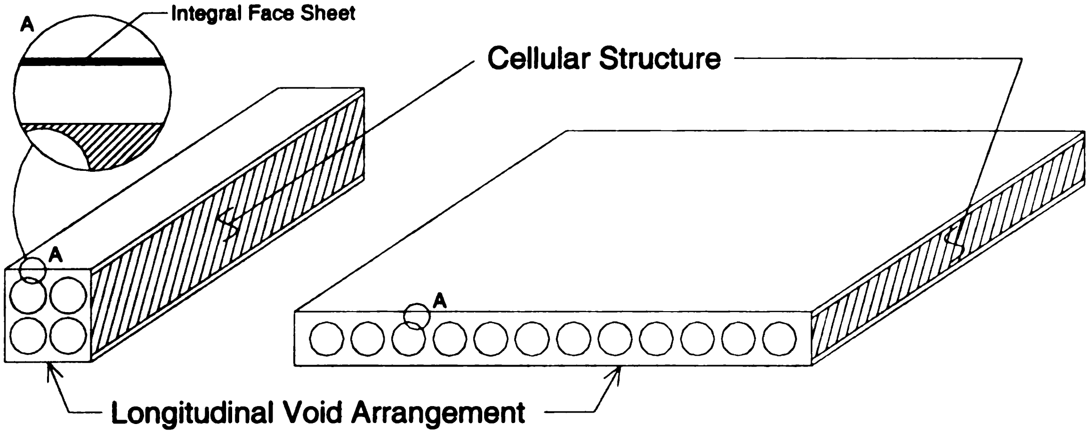

Figure 3.3. Hybrid cellular beam and plate

3.3 Experimental Studies

A structural experimental study was conducted with the aim of developing and evaluating hierarchical and hybrid sandwich structures that would allow biocomposites to be used for load-bearing structural components. The study included manufacturing and flexural testing of laboratory-scale cellular beams and plates with varying cellular topologies and hybrid material systems. The dimensions of the test units (Figure 3.1) and size of the cells were selected based on a similar study by Huang and Gibson (1995), where all-resin cellular beams and plates were manufactured and tested to show the improvement in performance gained by using cellular structures.

Several manufacturing issues arose during the development of the structural forms, which limited the level of detail that could be achieved in the cellular structures and the fiber volume content of the biocomposite material system. As mentioned above the size of the beams and plates and the cell size were selected base on a study by Huang and Gibson. In addition, the size of the beams and plates were limited to due cost concerns for this experimental study. The cells were created using rubber tubes, which are limited to standard sizes and typically run in 3.18 mm (1/8") intervals. Thus, the level of cellular and hierarchical structure that could be achieved in the test units was constrained, since the cell sizes were based on a limited set of dimensions. Coupled with the size of the cellular beam and plate molds, the dimensions of the cell sizes considered for the cellular beams and plates were limited to diameters of: 9.53 mm (3/8"), 6.35 mm (1/4"), 4.76 mm (3/16"), and 3.18 mm (1/8"). In addition, the relatively small size of the mold compared to the size of the cells left very small spaces between the cells. These small gaps were very difficult to uniformly fill with material during manufacturing. By trial and error, a fiber weight fraction of 10% (which corresponds to a fiber volume fraction of approximately 8%) was found to be adequate for manufacturing. Thus, the cellular beams and plates investigated in the experimental studies were developed based on the above mentioned manufacturing constraints. These manufacturing constraints may not arise for larger scale cellular beams and plates.

In the following section the dimensions and details of the developed cellular layouts are presented in a test matrix, which is followed by the materials and constituents used for the experimental studies. The process used for manufacturing the cellular beams and plates is then presented, followed by the details of the setup used for the flexural testing the cellular beams and plates.

3.3.1 Test Matrix

The use of hierarchical cellular and sandwich structures to improve the performance of biocomposite materials was investigated experimentally through flexural tests on laboratory-scale beams and plates. The objective of the study was to evaluate the flexural performance of the biocomposite cellular concepts, and to assess the effects of hierarchical cellular architectures and hybrid material designs. Three cellular beams with varying cellular structures, two cellular plates with varying cellular structures, and four hybrid cellular plates systems were considered for the structural experimental program. The test matrix with dimensions, cellular structures, and relative densities of all the samples is schematically depicted in Figure 3.4.

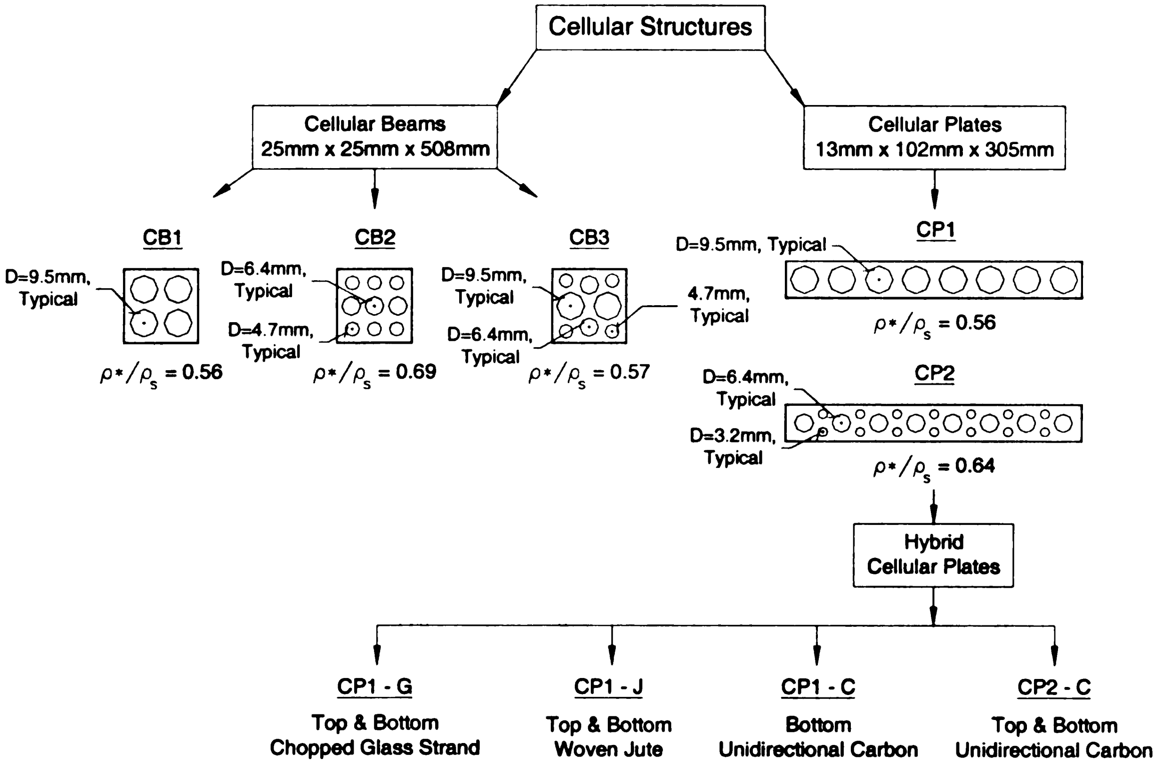

Figure 3.4. Schematic of the sample matrix for the experimental studies

Each cellular beam and plate type was given a sample identification label (ID) depending on the type of structure (cellular beam or plate), the cellular architecture used, and the hybrid material system (if used). The first letters of the ID stand for either cellular beam, CB, or cellular plate, CP. The following digit refers to the layout of the cellular architecture as shown in Figure 3.4. A final letter is used for the hybrid cellular structures, which stands for the type of fiber face sheets used in the hybrid structure. The hybrid material systems and letter IDs are shown in Figure 3.4.

The material design for all the test units is summarized in Table 3.1, noting that unsaturated polyester resin was used for all materials systems. The influence of the hierarchical arrangement of the cellular structure was evaluated through different cellular design as shown in Figure 3.4. Improvement on structural performance through hybrid cellular sandwich plates was investigated by the use of synthetic and natural fibers cured integrally with the cellular core. The hybrid material systems used for the experimental study are shown in Figure 3.4. It should be noted that the research program was aimed towards concept development and feasibility evaluation. Thus, multiple tests of equal samples were not considered. A pictorial summary of the built test units is given in Figure 3.5 through Figure 3.8.

Table 3.1. Test matrix of cellular beams and plates with unsaturated polyester resin

Fiber	*Material ID*	*Fiber Volume (%)*	*Test Unit ID*
Cellular Beams			
Green Hemp	01	8	CB1, CB2, CB3
Cellular Plates			
Green Hemp	01	8	CP1, CP1-G, CP1-J, CP1-C
Raw Hemp	02	8	CP1, CP2, CP2-C
Flax	03	10	CP1, CP1-J


(a) Cellular beam 1 (CB1) (b) Cellular beam 2 (CB2) Cellular beam 3 (CB3)

Figure 3.5. Pictorial summary of the cellular beam test units

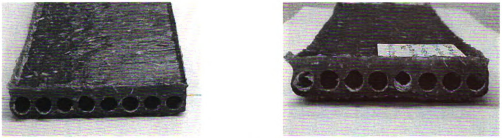

(a) Cellular plate 1 (CP1)

(b) Cellular plate 1 with bottom carbon layer (CP1-C)

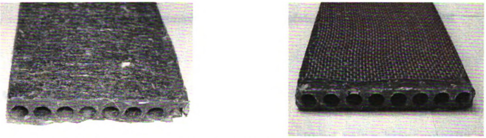

(c) Cellular plate 1 with top and bottom glass strand mat layers (CP1-G)

(d) Cellular plate 1 with top and bottom woven jute fabric layers (CP1-J)

Figure 3.6. Pictorial summary of cellular plates with green hemp/UPE

(a) Cellular plate 2 (CP2)

(b) Cellular plate 2 with top and bottom carbon layers (CP2-C)

Figure 3.7. Pictorial summary of the cellular plates with raw hemp/UPE

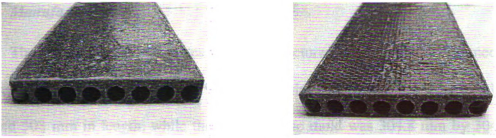

(a) Cellular plate 1 (CP1)

(b) Cellular plate 1 with top and woven jute fabric layers (CP1-J)

Figure 3.8. Pictorial summary of the cellular plates with chopped flax/UPE

3.3.2 Materials and Constituents

The cellular beams and plates were manufactured using biocomposite material systems with either green hemp, raw hemp, or chopped flax fibers, and unsaturated polyester resin (Table 3.1). The biocomposite material systems are described and the performed characterization studies are presented in Section 2.3. The resin system used was an ortho unsaturated polyester (UPE) with methyl ethyl ketone peroxide (MEKP) catalyst (1% by weight of resin), and cobalt naphthenate (CN) promoter (0.03% by weight of resin). The resin system used for the cellular beams and plates was the same system used for the material experimental program, and is shown in tabular form in Table 2.1.

The hybrid cellular plates were manufactured with integral face sheets of either synthetic or natural fabrics. Three types of fiber fabrics were used for the face sheet layers: (a) woven jute, (b) randomly orientated glass, and (c) unidirectional carbon (Figure 2.23). The face sheet material systems and their characterization is presented in Section 2.4. A summary of the average mechanical properties of the face sheet material systems used in the hybrid cellular plates is given in Table 2.17.

3.3.3 *Manufacturing*

The cellular beams and plates were manufactured using specially designed molds with removable faceplates (Figure 3.9). The cellular beam mold was 25.4 mm by 25.4 mm and 508 mm in length, while the cellular plate mold was 304.8 mm by 304.8 mm with a thickness of 12.7 mm. The removable faceplates allowed different cellular configurations to be implemented with the same mold.

In order to release the samples from the mold after curing, the molds were lined with Teflon paper (Figure 3.10a). The cells in the cellular beams and plates were created by placing rubber tubing through the faceplate (Figure 3.9). Steel rods were placed inside the rubber tubes to stiffen the tubes, and ensure that the tubes remained straight during manufacturing (Figure 3.10b). Tubes smaller than 6.4 mm (1/4") in diameter were held straight by tensioning the tubing and anchoring it to the mold using small nails. A wood block was placed inside the plate mold to allow manufacturing of plates with a reduced width of 101.6 mm (Figure 3.9b).

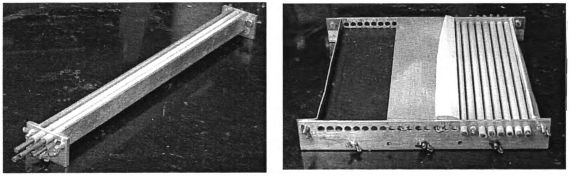

(a) Cellular beam mold, and rods

(b) Cellular plate mold, rods, and Teflon paper

Figure 3.9. Specially designed molds used for manufacturing the cellular beams and plates

The biocomposite material system was prepared for manufacturing by pouring the resin over the fibers (Figure 3.10e) and mixing the two materials together by hand until the composite material was consistent (Figure 3.10f). For the hybrid cellular plates, the fiber fabric layers were wet out by pouring and spreading the resin over the fabric and were then placed in the mold. The typical mold and material preparation process for manufacturing of the cellular beams and plates is summarized in the photograph sequence shown in Figure 3.10.

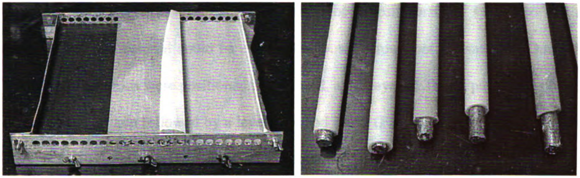

(a) Mold with Teflon paper

(b) Rubber rods with inner rods

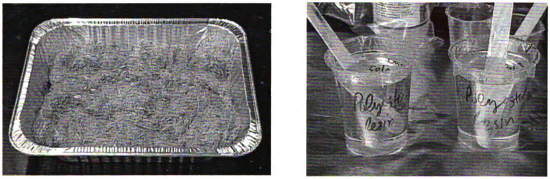

(c) Pan with dry natural fibers

(d) Unsaturated polyester resin

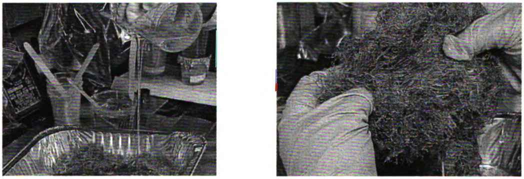

(e) Wetting of fibers with resin

(f) Mixing of fibers and resin

Figure 3.10. Preparation of the mold and material system

With the preparation of the mold and material system completed, a layer of material was placed on the bottom of the mold, followed by a layer of rods (Figure 3.11g-i). Another layer of material was then placed on top of the rods and compacted in the voids between the rods (Figure 3.11j). This procedure was repeated until all the layers of rods had been placed in the mold. Because of the small space left between the rods, a low fiber weight fraction was required for the biocomposite material system so that a properly wet-out material could be evenly distributed throughout the sample. Once all the material and rods were positioned in the mold, a top layer of Teflon paper was placed on top of the sample followed by a leveling wood block (Figure 3.11k). Steel plates and weights (14 kPa of pressure) were then placed on top of the leveling wood block to uniformly compact the top layer of the sample and obtain a flat surface (Figure 3.11l). All cellular beams and plates were oven cured using a cycle of 100°C for 2 hours, followed by 150°C for 2 hours. The typical manufacturing process of the cellular beams and plates is summarized in the photograph sequence shown in Figure 3.11.

(g) Inserting rods into plate mold

(h) Mold with rods in place (partial)

(i) Mold with rods in place

(j) Placement of top material layer

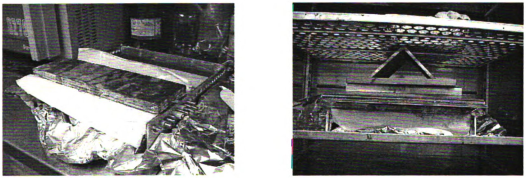

(k) Covering and leveling

(l) Oven curing with steel weights

Figure 3.11. Manufacturing process of biocomposite cellular beams and plates

3.3.4 Test Setup

The flexural characterization of the cellular beams and plates was done through flexural test setups mounted on an MTS loading frame. The cellular beams were tested in four-point bending with a total span on 457 mm. Load was applied to the beams using the test frame loading ram and a loading fixture that applied two point loads at 102 mm apart with 178 mm shear spans (Figure 3.12a). The cellular plates were tested in three-point bending with a shear span of 267 mm (Figure 3.12b). The samples were supported using a fixture from a steel I-beam and adjustable roller supports. To avoid local deformations (crushing), aluminum strips were placed underneath each sample at the supports. The testing setups used for both the cellular beams and plates are shown in Figure 3.13. All test units were loaded monotonically up to failure in displacement control at a deformation rate of 0.01 mm/sec. The deflection of the beams and plates was measured at mid-span using an externally mounted extensometer and the internal LVDT of the loading frame. The applied load was measured using the internal 12 kN load cell of the testing frame. The stiffness (force per unit displacement) was measured by taking the slope of the initial linear portion of the measured load displacement curve.

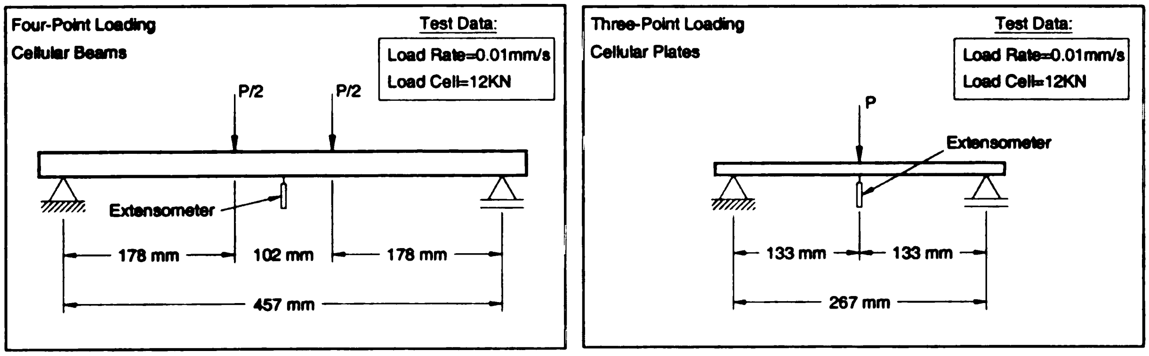

(a) Cellular beam four-point bending test (b) Cellular plate three-point bending test

Figure 3.12. Schematic of flexural test setups

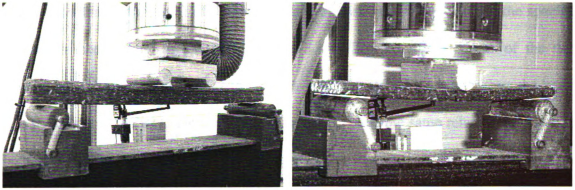

(a) Cellular beam four-point bending test (b) Cellular plate three-point bending test

Figure 3.13. Pictures of flexural tests on cellular beams and plates

3.4 Cellular Beams

Biocomposite cellular beams with varying cellular and hierarchical topologies were tested to investigate the effect of hierarchical cellular architectures on the flexural performance. The observed test behavior and results are presented in the following section.

3.4.1 Observed Behavior and Test Results: Cellular Beams

The results of the cellular beams with green hemp/unsaturated polyester are shown in Figure 3.14 and given in Table 3.2. All cellular beams behaved linear-elastically up to failure exhibiting only small deformations. The failure mode of the biocomposite cellular beams was a sudden tensile rupture of the bottom surface of the beam.

The effect of cellular and hierarchical topologies in the performance of the cellular beams is not evident in the force-displacement response (Figure 3.14). Clearly from the measured results, the beams with higher relative density, i.e. more solid material, showed a higher flexural stiffness (Figure 3.14). The effect of hierarchical structure on the performance of the beams must be evaluated by comparing the specific stiffness of the beams, as shown in Figure 3.15. The specific stiffness of the two hierarchical cellular beams (CB2 and CB3) is approximately 12% higher than the beam with periodic cells (CB1). Notice that CB1 and CB3 have the same relative density (use the same amount of material), but by arranging the material of CB3 in a hierarchical architecture the stiffness (Table 3.2) and relative stiffness (Figure 3.15) are improved.

Due to manufacturing limitations and constraints on the available cell sizes the level of hierarchical architecture that could be achieved was limited. Thus, the improvement in performance shown in the experimental results is not large. Nonetheless, the experimental results show the improvement in structural performance that can be achieved by using an efficient hierarchical arrangement of material. More detailed and efficient hierarchical arrangements should be possible for larger structures with more available options in cell sizes.

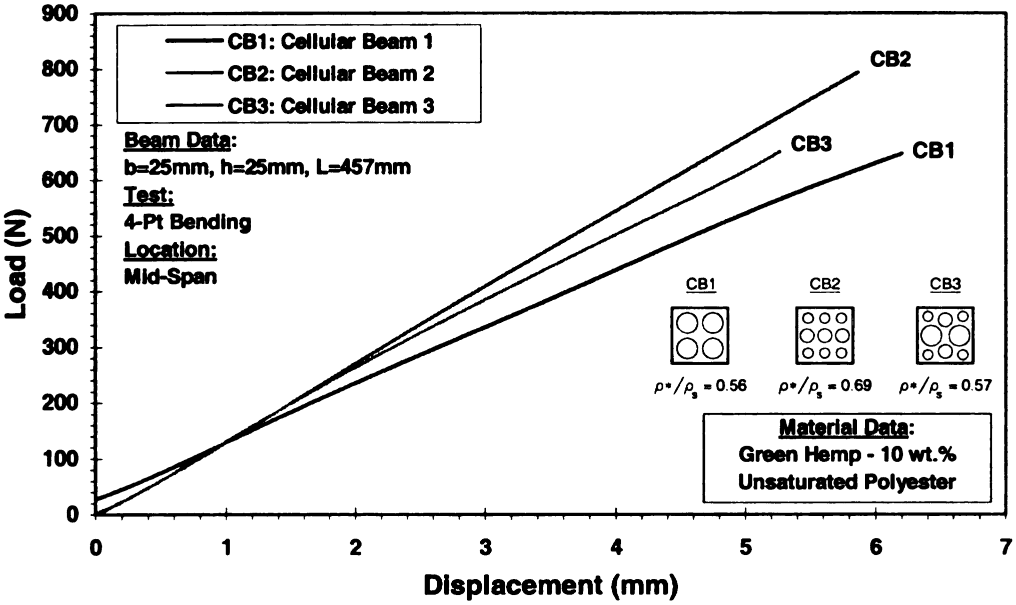

Figure 3.14. Force versus displacement response at mid-span of cellular biocomposite beams

Table 3.2. Flexural test results summary of cellular biocomposite beams

Material	*Beam Type*	*Fibers by Wt. (%)*	*ID*	*Strength (N)*	*Max Displ. (mm)*	*Stiffness (N/mm)*
G.Hemp/UPE	CBS1	10	CBS1-01-03	669.7	6.20	101.9
G.Hemp/UPE	CBS2	10	CBS2-01-01	813.2	5.87	135.1
G.Hemp/UPE	CBS3	10	CBS3-01-02	677.5	5.58	117.0

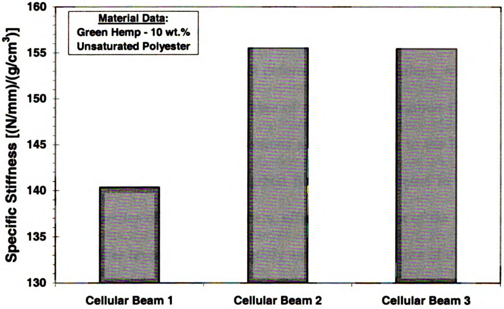

Figure 3.15. Specific stiffness of cellular biocomposite beams

3.5 Cellular Plates

Results form the flexural tests on cellular plates are divided into the following groups: (i) cellular and hybrid plates with green hemp/unsaturated polyester, (ii) hybrid cellular plates with carbon face sheets and the corresponding non-hybrid cellular plates, and (iii) cellular and hybrid plates with flax/unsaturated polyester. Data from the flax cellular plates is presented together with results from the green hemp and an all-unsaturated polyester cellular plates for comparison. The observed test behavior and results are presented in the following section.

3.5.1 Observed Behavior and Test Results: Cellular Beams

The results of the cellular and hybrid plates with green hemp/unsaturated polyester are shown in Figure 3.16 and provided in Table 3.3. All plates behaved linear-elastically up to failure (Figure 3.16), failing in a sudden brittle rupture at the bottom fiber of the plate. The plates exhibited small deformations up to failure, with exception of the hybrid cellular plate with a bottom layer of unidirectional carbon (Figure 3.16). This hybrid cellular plate showed large defections near failure due to the large strength capacity provided by the bottom layer of carbon fibers. The increase in strength is a result of the high properties of the carbon fibers, efficient placement of the material, and curing of the carbon fiber layer of fibers integrally with the cellular core of the plate.

The use of hybrid cellular plate systems improved both the stiffness and strength of the plates as shown in Figure 3.17. The hybrid plates with top and bottom layers of glass strand mat and jute fabric increased the strength of the cellular plate by 50%, while their stiffness remained constant (Table 3.3). The increase in strength due to the addition of top and bottom jute fabric layers is nearly equal to the increase due to the use of glass strand mat layers (Table 3.3). This suggests the strength of a biocomposite cellular plate can be increased by adding woven natural fiber layers, which maintains the "green" appeal of the biocomposite material system. The use of unidirectional glass mat or a denser weave of natural fiber fabric may result in a stiffer fiber mat, thus increasing the stiffness of the plate as well as the strength.

The results in Figure 3.16 show that both the strength and stiffness are significantly improved by adding only a bottom layer of carbon fiber to the biocomposite cellular plate. The carbon fiber layer is most efficient on the bottom of the plate because it prevents the progressive tensile rupture of the biocomposite material in this region, and improves the structural stiffness of the plate. Therefore, the hybrid hemp/carbon plate increased the strength of the base-line cellular plate by a factor of seven, and almost doubled the stiffness (Table 3.3). The hybrid hemp/carbon cellular plate also improved the strength of the plate four and a half times over the hybrid hemp/glass and hemp/jute plates (Table 3.3). The results show that by placing only a small amount of high performance material in the most efficient location the properties of the plate can be dramatically increased.

In addition to the improvement in strength and stiffness due to the use of hybrid systems, the integral casting of the fiber layers with the cellular plate eliminates failure due to delamination. Delamination failure typically occurs in sandwich panels where the top and bottom face sheets are simply bonded to the core material. The bond between the face sheet and the core creates a weak plane that can lead to premature failure of the plate (Jones 1999). None of the samples tested failed by delamination, thus showing the importance of casting the top and bottom face sheets integrally with the cellular core.

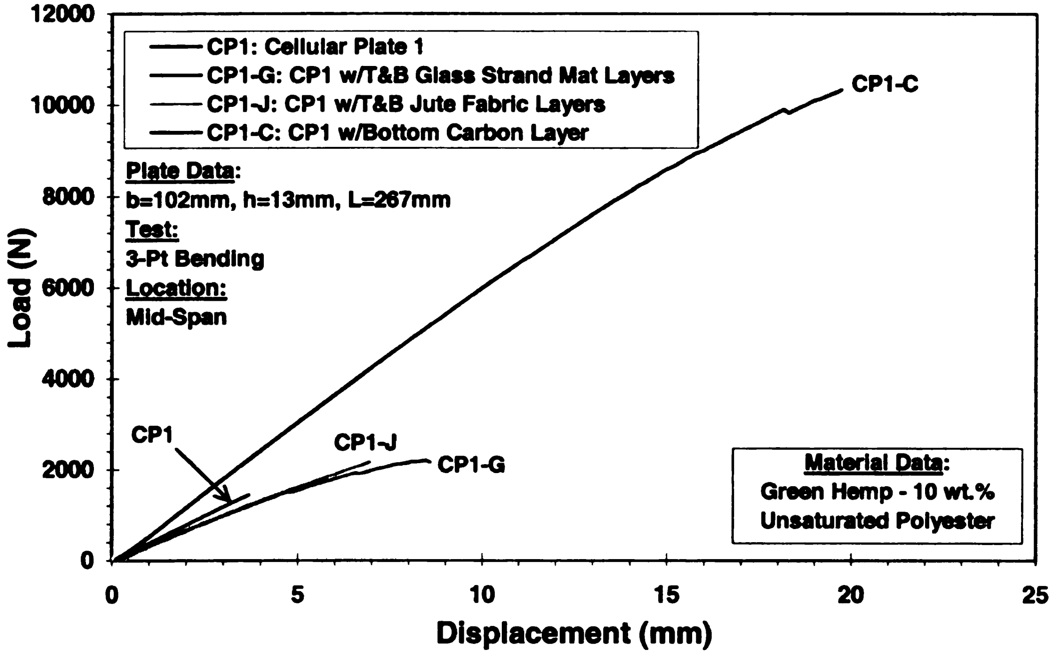

Figure 3.16. Force versus displacement response at mid-span of cellular and hybrid plates with green hemp fibers, and unsaturated polyester

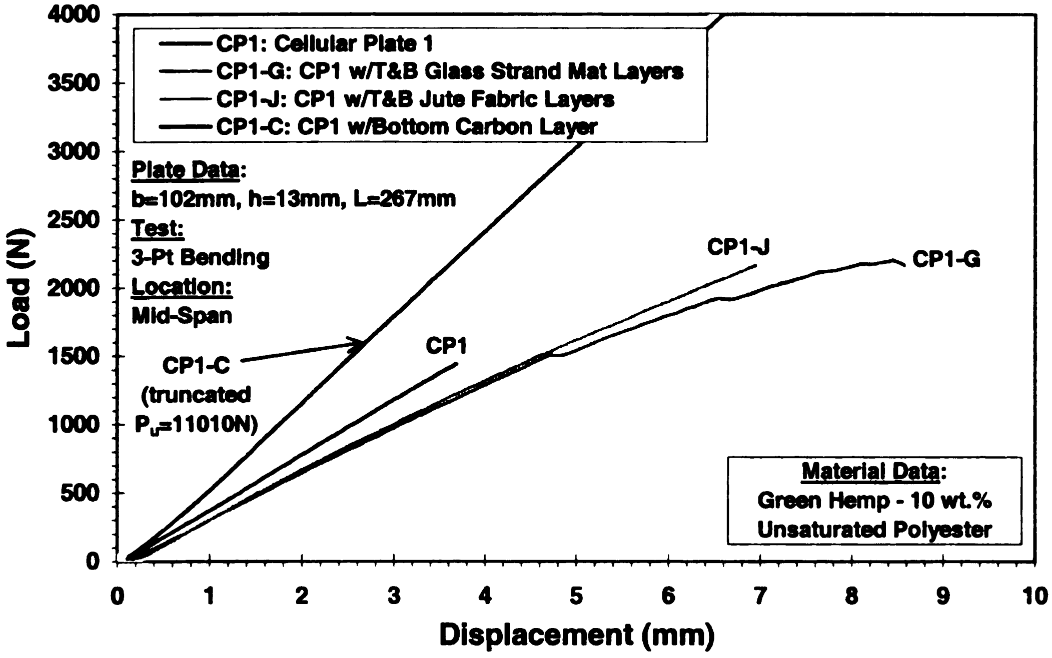

Figure 3.17. Force versus displacement response at mid-span of cellular and hybrid plates with green hemp fibers, and unsaturated polyester, zoomed in view

Table 3.3. Flexural test results summary of cellular, and hybrid plates with green hemp fibers

Material	*Beam Type*	*Fibers by Wt. (%)*	*ID*	*Strength (N)*	*Max Displ. (mm)*	*Stiffness (N/mm)*
G.Hemp/UPE	CP1	10	CP1-01-01	1483.3	3.65	406.0
G.Hemp/UPE - T&B Glass	CP1	10	CP1-11-01	2236.904	8.42	319.7
G.Hemp/UPE - Bottom Carbon	CP1	10	CP1-21-01	10396.8	19.70	591.9
G.Hemp/UPE - T&B Jute	CP1	10	CP1-31-01	2196.8	6.95	308.7

Results for the hybrid cellular plates with carbon face sheets, and the corresponding non-hybrid cellular plates are shown in Figure 3.18 and provided in Table 3.4. The response of all the cellular plates were similar to the results previously mentioned, except for the hybrid cellular plate with top and bottom carbon face sheets.

The results of the plate with top and bottom carbon layers (Figure 3.18) showed a bi-linear response due to buckling of the top carbon layer. Before buckling of the top layer both carbon layers contribute to the stiffness of the plate, thus the large slope of the first portion of the plot. After buckling of the top layer of carbon this layer no longer contributes to the stiffness of the plate, and thus the slope of the load-displacement plot decreases at this point. Essentially, after buckling of the top layer of carbon the plate is equivalent to the plate with only a bottom layer of carbon. This is shown in Figure 3.18 by comparing the slope of the plate with top and bottom carbon layers after buckling with the slope of the plate with only a bottom layer of carbon. The two slopes are almost the same after buckling of the top carbon layer.

Although the stiffness of the plate with top and bottom carbon layers was increased by 150% over the plate with only a single bottom carbon layer, the strength of the plate was not improved. This is due to the buckling of the top layer of carbon fabric, which occurred at only 50% of the peak load. In structural applications, the large loss of stiffness after buckling could make the structure unusable. Thus, when using hybrid material systems to improve the performance of biocomposite cellular structures, the placement of the material should be designed by considering the effect on the complete response of the structural component.

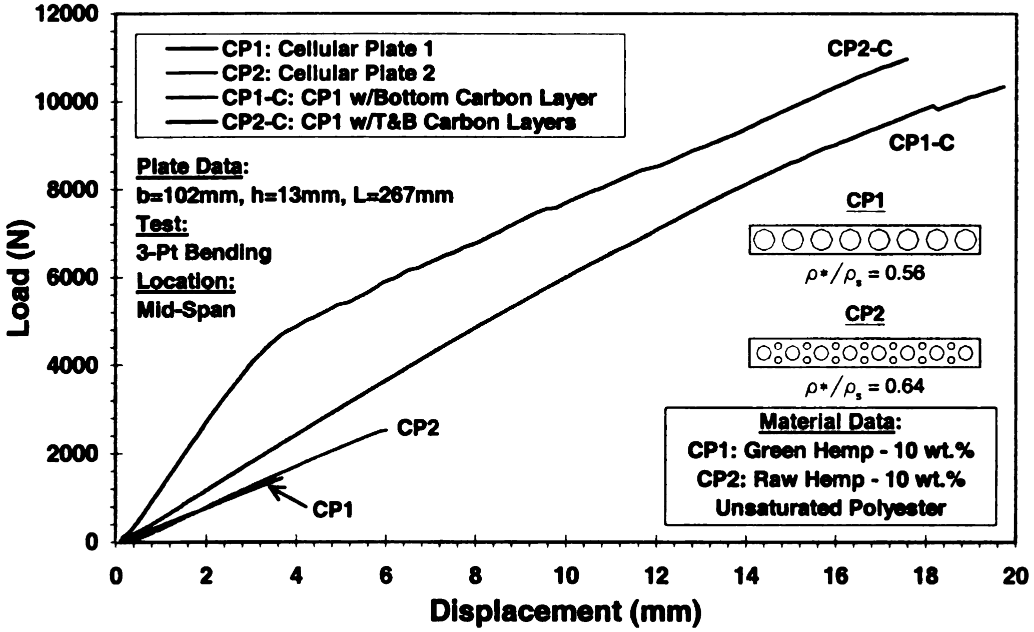

Figure 3.18. Force versus displacement response at mid-span of cellular, and hybrid plates with green hemp, and raw hemp fibers, and unsaturated polyester

Table 3.4. Flexural test results summary of cellular, and hybrid plates with green hemp fibers

Material	*Beam Type*	*Fibers by Wt. (%)*	*ID*	*Strength (N)*	*Max Displ. (mm)*	*Stiffness (N/mm)*
G.Hemp/UPE	CP1	10	CP1-01-01	1483.3	3.65	406.0
Raw Hemp/UPE	CP2	10	CBS2-01-01	2556.6	5.39	501.5
G.Hemp/UPE - Bottom Carbon	CP1	10	CP1-21-01	10396.8	19.70	591.9
Raw Hemp/UPE - T&B Carbon	CP2	10	CBS3-01-02	11010.4	17.56	1480.0

The effect of hierarchical topology on the performance of the cellular plates was investigated in a plate with periodic cells (CP1) and a plate with a hierarchical arrangement (CP2) as shown in Figure 3.18. The hierarchical cellular plate showed an increase in specific stiffness of 13% over the periodic cellular plate. As with the cellular beams, manufacturing limitations constrained the level of topological hierarchy that could be achieved in the cellular plates. Nevertheless, the experimental results show the improvement in structural performance that can be achieved by using an efficient hierarchical arrangement of material.

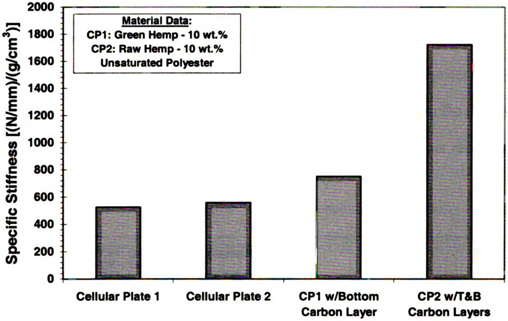

Figure 3.19. Specific stiffness of cellular and hybrid plates with green hemp fibers, and unsaturated polyester

The results of the cellular and hybrid plates with flax/unsaturated polyester are shown in Figure 3.20 and provided in Table 3.5. The flax biocomposite plates are compared with the green hemp/unsaturated polyester cellular plate and an all-unsaturated polyester plate. Both flax plates behaved linear-elastically up to failure exhibiting only small deformations. The failure mode for both cellular plates was a sudden tensile rupture at the bottom fiber of the plate.

Test results showed that the hybrid cellular plate system with top and bottom woven jute fabric layers improved both the stiffness and strength of the flax plate (Figure 3.20), increasing the stiffness by 32% and the strength by 70% (Table 3.5). These test results are similar to the test results of the green hemp hybrid plates in this section.

The test results also show that the flax cellular plate performs relatively poorly compared to the green hemp cellular plate (Figure 3.20). In fact, the stiffness of the flax cellular plate was equal to the all-unsaturated polyester cellular plate, while the strength was lower. Thus, the flax fibers are not reinforcing the unsaturated polyester matrix, but they are rather acting as a pollutant. This behavior is most likely due to the short length of the flax fibers. Based on these results, the chopped flax fibers are not recommended for structural applications.

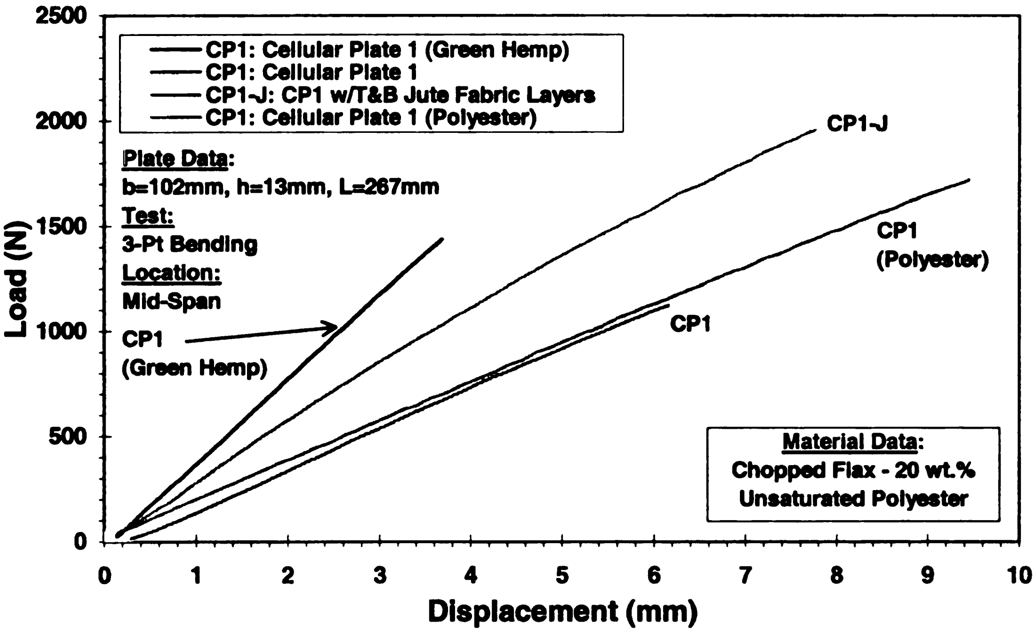

Figure 3.20. Force versus displacement response at mid-span of cellular and hybrid plates with flax fibers, and unsaturated polyester

Table 3.5. Flexural test results summary of cellular, and hybrid plates with flax fibers

Material	*Beam Type*	*Fibers by Wt. (%)*	*ID*	*Strength (N)*	*Max Displ. (mm)*	*Stiffness (N/mm)*
G.Hemp/UPE	CP1	10	CP1-01-01	1483.3	3.65	406.0
Flax/UPE	CP1	20	CP1-04-01	1171.7	6.16	196.5
Flax/UPE - T&B Jute	CP1	20	CP1-34-01	1979.7	7.77	259.4
Polyester	CP1	--	CP1-03-04	1764.2	9.45	185.8

3.6 Comparison with Wood Beams and Plates

One wood beam and three wood plates were tested in flexure and used for comparison with the cellular beam and plate results from the structural experimental program. One type of wood, douglas fur, was used for the beam, and three types of wood, douglas fur (DF), oriented strand board (OSB), and particle board (PB), were used for the plates. The same dimensions of cellular beams and plates used in the experimental studies were used for the wood beam and plates. The DF wood beam is shown in Figure 3.21a, while the DF plate is shown in Figure 3.21b, the OSB plate is shown in Figure 3.22a, and the PB plate is shown in Figure 3.22b.

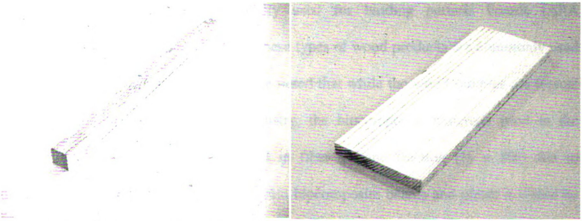

(a) Beam: 25.4 mm x 25.4mm x 508 mm (b) Plate: 12.7 mm x 106.4 mm x 304.8 mm

Figure 3.21. Douglas Fur beam and plate test units

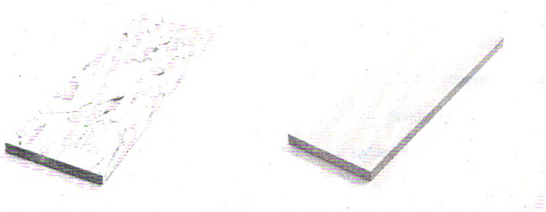

(a) Orientated strand board plate: 0.5"x 4"x 12" (b) Particle board plate: 0.5"x 4"x 12"

Figure 3.22. Wood plate test units

The douglas fur wood material is standard stock lumber (solid piece of wood). The oriented strand board is made by pressing layers of wood chip lamina together and bonding them with a small amount of resin. Phenolic and diphenyl-methane-di-isocyanate (MDI) resins are typically used for binding OSB panels (APA Engineered Wood Association 2003). The particle board is made in a similar manner, by pressing small wood fibers (saw dust) and bonding them together with a small amount of resin. Urea-Formaldehyde resins are typically used for binding particle boards (APA Engineered Wood Association 2003). These types of wood products are commonly used in the construction industry. It should be noted that while the wood samples are typical materials used in the construction industry, the biocompostie materials used in the cellular beams and plates were limited in fiber volume fraction (V_f = 8%) due to limitations in manufacturing. For full-scale biocomposite beams and plates it would be possible to achieve much higher volume fractions, thus improving the properties of the material. The comparison of the wood and biocomposite cellular structures must be viewed in this context.

3.6.1 Observed Behavior and Test Results: Wood Beams

The results of the douglas fur (DF) beam is compared with the biocompoiste cellular beams in Figure 3.23 and Table 3.6. The DF beam behaved nonlinearly due to crushing of the material in the top layer of the beam near failure exhibiting large deformations. The failure mode of the DF beam was a sudden tensile rupture of the bottom fiber of the beam.

The DF beam out-performed the biocompsotie beams in both stiffness and strength (Figure 3.23). This is expected, as the wood material is structural grade, while the manufacturing constrains of the biocomposites material limited the fiber volume fraction that could be achieved.

Despite the use of hierarchical cellular structures in the biocomposites beams, the DF beam still out-performed the biocomposite cellular beams (Figure 3.24). The large specific stiffness of the DF beam is due to the high stiffness of the wood beam to the biocomposite beams, and the very low density of wood.

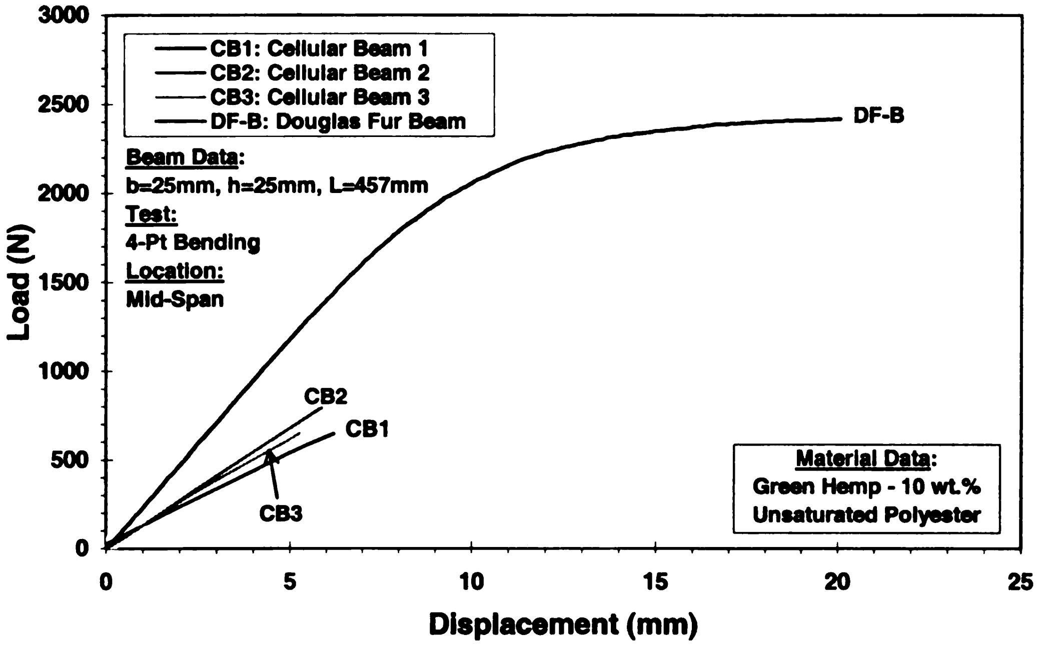

Figure 3.23. Force versus displacement response comparison of cellular, and wood beams

Table 3.6. Flexural test results summary of cellular, and wood beams

Material	*Beam Type*	*Fibers by Wt. (%)*	*ID*	*Strength (N)*	*Max Displ. (mm)*	*Stiffness (N/mm)*
G.Hemp/UPE	CBS1	10	CBS1-01-03	669.7	6.20	101.9
G.Hemp/UPE	CBS2	10	CBS2-01-01	813.2	5.87	135.1
G.Hemp/UPE	CBS3	10	CBS3-01-02	677.5	5.58	117.0
Douglas Fur	DF-B	--	DF-B-01	1379.4	5.73	236.6

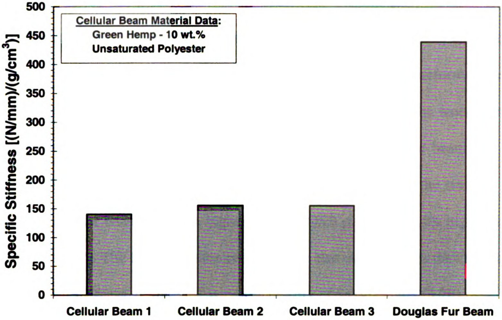

Figure 3.24. Specific stiffness of cellular and wood beams

3.6.2 Observed Behavior and Test Results: Wood Plates

The results of the douglas fur (DF), oriented strand board (OSB), and particle board (PB) wood plates are compared with a green hemp/unsaturated polyester biocomposite cellular plate in Figure 3.25 and Table 3.7. The DF plate behaved nonlinearly due to crushing of the material in the top layer of the beam near failure exhibiting large deformations. The failure mode of the DF plate was tensile rupture of the bottom fiber of the beam. The fracture of the bottom fiber of the DF plate was not sudden, but rather gradual cracking along the bottom of the plate (shown by the spikes in Figure 3.25). The OSB and PB plates behaved linear-elastically up to failure exhibiting only small deformations. The failure mode of the OSB plate was fracture of the cross-ply above the bottom fiber of the plate, while the failure mode of the PB plate was a sudden tensile rupture of the bottom layer of the beam.

The DF plate out-performed the biocomposite cellular plate in stiffness, and strength (Figure 3.25), and specific stiffness (Figure 3.26). These results are similar to those of the DF beam. However, the biocomposite cellular plate out-performed the OSB and the PB plates in strength and stiffness (Figure 3.25), even though the wood plates are considered structural grade. The stiffness of the biocomposite cellular beam was 107% higher than the OSB plate and 230% higher than the PB plate, while the strength of the biocomposite cellular beam was 62% higher than the OSB plate and 114% higher that the PB plate (Table 3.7). The bio composite cellular plate also out-performs the OSB and PB plates in specific stiffness, despite the very low density of wood (Figure 3.26).

The results of this comparison show that biocomposite cellular plates can out-perform engineered wood products. Thus, biocomposites cellular structures have the potential to be used for applications where these engineered wood products are used. The results would be more in favor of the biocomposite cellular plates if an improved manufacturing procedure was used to fabricate plates with higher fiber volume fractions, or if hybrid biocomposite cellular components were used.

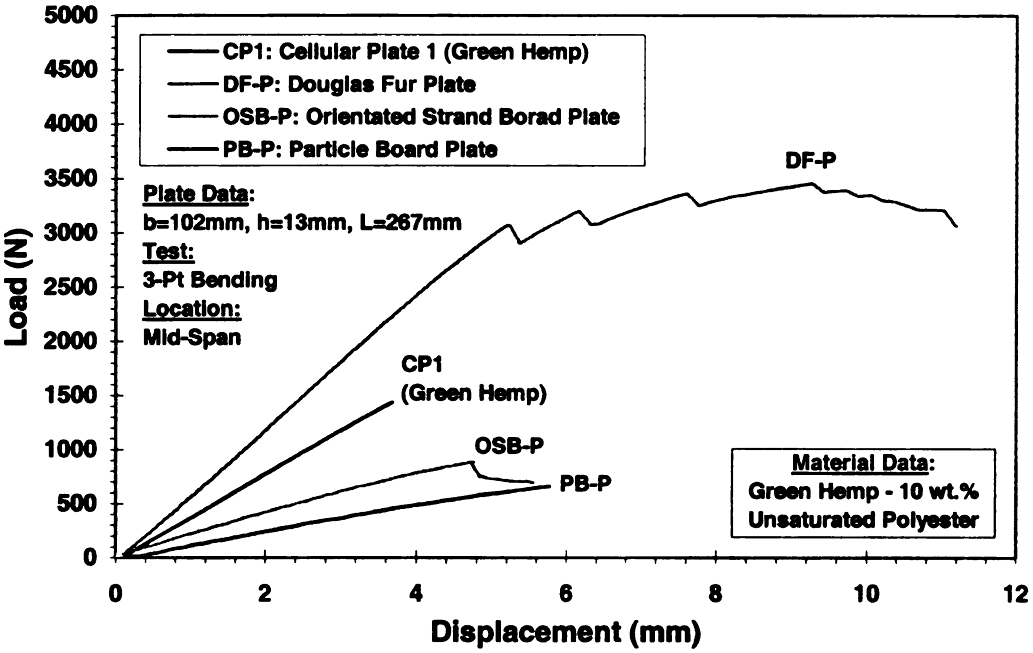

Figure 3.25. Force versus displacement response comparison of cellular, and wood plates

Table 3.7. Flexural test results summary of cellular, and wood plates

Material	*Plate Type*	*Fibers by Wt. (%)*	*ID*	*Strength (N)*	*Max Displ. (mm)*	*Stiffness (N/mm)*
G.Hemp/UPE	CP1	10	CP1-01-01	1483.3	3.65	406.0
Douglas Fur	DF-P	--	DF-P-01	3494.7	11.19	628.7
Orientated Strand Board	OSB-P	--	OSB-P-01	916.6	5.56	195.8
Fiber Board	PB-P	--	FB-P-01	694.3	6.15	123.0

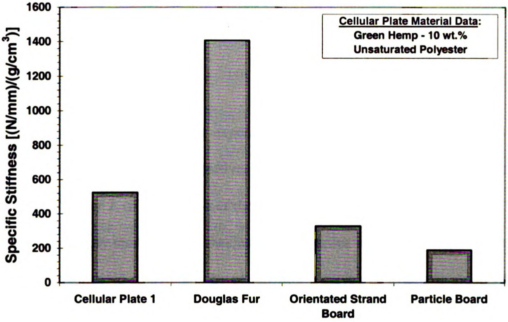

Figure 3.26. Specific stiffness of cellular and wood plates

CHAPTER 4 ANALYTICAL STUDIES

4.1 Overview

The material and structural experimental studies of Chapters 2 and 3 were investigated analytically with the objectives of: (i) validation of the material experimental studies from Chapter 2, (ii) validation of the structural experimental studies from Chapter 3, and (iii) feasibility studies. The mechanical properties of the biocompostie material systems are investigated analytically by conducting a survey of available models for the properties of randomly oriented short fiber composites, and comparing the models with experimental results. The biocomposite material models are then used with conventional structural mechanics to analyze the cellular beams and plates, and compare with the measured results. Next, the performance of the biocomposite cellular structures in flexure is assessed using indices and factors, which measure the efficiency of a material and structure in flexure. A more refined analysis procedure is then proposed, which can be automated in mathematical software to easily analyze hierarchical cellular structures and used for parametric and optimization studies. The thermal effects due to curing in hybrid cellular structures are considered, and the resulting prestressing of the section is investigated analytically on laboratory and full-scale structural components. The analytical models are then used to predict the performance of full-scale biocomposite structural components for civil applications. Application of biocomposite structural components for a highway bridge deck, and commercial and residential flooring systems is investigated. The concepts discussed above are presented in detail in the following sections

4.2 Properties of Randomly Oriented Short Fiber Composites

The elastic constants, and strength of biocomposite materials can be predicted using analytical models for randomly oriented short fiber composites. The analytical models for randomly oriented short fiber composites presented in this section are based on using the properties of equivalent unidirectional lamina and averaging the properties over all fiber directions. Thus, the micromechanical properties of unidirectional orthotropic lamina are presented along with the properties of randomly oriented fiber composites.

Randomly oriented short fiber-reinforced composites are not as strong or as stiff as continuous fiber-reinforced composites, but short fiber composites do have several attractive characteristics that make them attractive for structural applications (Gibson 1994). For example, short fiber composites can be easily mixed with liquid resin and used to produce parts having complex geometry. The processing methods for short fiber composites such as resin transfer molding, injection molding, or compression molding are fast and inexpensive, which makes them attractive for high volume applications. Composites having randomly oriented short fiber reinforcement are nearly isotropic, compared to unidirectional continuous fiber composites that are highly anisotropic. The advantages of low cost, ease of fabricating complex parts, and isotropic behavior make short fiber composites attractive for many applications.

In the following sections the micromechanical equations for the elastic moduli, and strength of continuous fiber composites are presented. The continuous unidirectional equations are needed to model the face sheet materials, e.g. carbon and jute fiber mats, and to establish limits for the short fiber models. Next, models for the properties of short fiber composites, including a series of models for the isotropic elastic constants and strength of randomly oriented short fiber composites are presented. The results from the analytical models for randomly oriented short fiber composites are then compared with measured results from the material experimental program of Chapter 2.

4.2.1 Continuous Fiber Composites

A mechanics of materials approach can be used as a basic method to model the micromechanics of continuous fiber-reinforced composite materials (Jones 1999). The mechanics of materials approach implies that certain simplifying assumptions must be made in order to arrive at an effective solution. The most important assumption made is that the strains in the fiber direction of the composite are the same in the fibers as in the matrix. In other words, when stressed in the 1-axis, or material longitudinal axis, the plane sections normal to the 1-axis will remain plane after stressing. This assumption is similar to the "plane sections remain plane" assumption made in the mechanics of materials approach to beam theory. Other important assumptions in the mechanics of materials approach include: (i) the fibers are all uniform in properties and diameter, continuous, and parallel through the media, and (ii) there is a perfect bond between the fibers and matrix so that no slippage can occur.

In the following sections the mechanics of materials approach is used to derive the orthotropic moduli, E_1, E_2, ν_{12}, and G_{12}, and strength of a continuous unidirectional fiber-reinforced composite (Figure 4.1). The derived properties are obtained by analyzing a representative volume element (Figure 4.1). Other approaches to the mechanical properties, such as the theory of elasticity, are available. However, the results from the mechanics of materials approach provide simple and practical equations that accurately predict experimental behavior (Jones 1999, Gibson 1994).

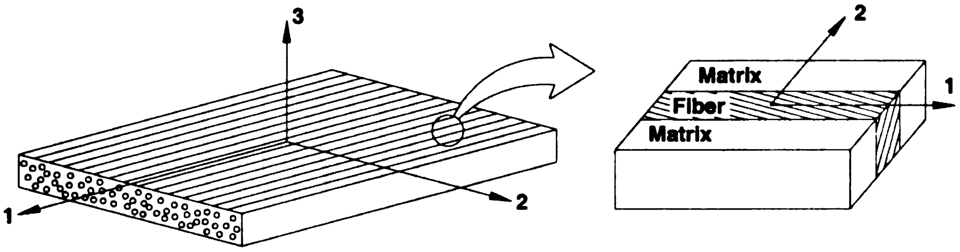

Figure 4.1. Orthotropic lamina, and representative volume element

4.2.1.1 *Properties for Continuous Fiber Composites: Stiffness*

Consider first the modulus of a unidirectional fiber-reinforced composite in the 1-direction (Figure 4.1). From Figure 4.2, the strain in the 1-direction is:

$$\varepsilon_1 = \frac{\Delta_L}{L}, \tag{4.2.1}$$

where the strain is the same in both the fiber and matrix. If both the fibers and matrix are elastic the stresses in the 1-direction are:

$$\sigma_f = E_f \varepsilon_1 \qquad \sigma_m = E_m \varepsilon_1 . \tag{4.2.2a,b}$$

In Figure 4.2 the stress σ_1 acts over the entire cross-sectional area A of the representative volume element, while σ_f acts over the cross-sectional area of the fibers A_f, and σ_m acts over the cross-sectional area of the matrix A_m. Accordingly, the resultant force in the representative volume element is:

$$P = \sigma_1 A = \sigma_f A_f + \sigma_m A_m . \tag{4.2.3}$$

Using Equation (4.2.2) with Equation (4.2.3), and recalling that $\sigma = E\varepsilon$, the elastic modulus in the 1-direction can be written as

$$E_1 = E_f \frac{A_f}{A} + E_m \frac{A_m}{A}. \tag{4.2.4}$$

Assuming no voids in the composite, the fiber volume fractions of the fibers and matrix can be written as

$$V_f = \frac{A_f}{A} \qquad V_m = \frac{A_m}{A}. \tag{4.2.5a,b}$$

Substituting Equation (4.2.5) into (4.2.4) leads to

$$E_1 = E_f V_f + E_m V_m, \tag{4.2.6}$$

which is known as the *rule of mixtures* for the apparent Young's modulus of the composite material in the 1-direction (Jones 1999).

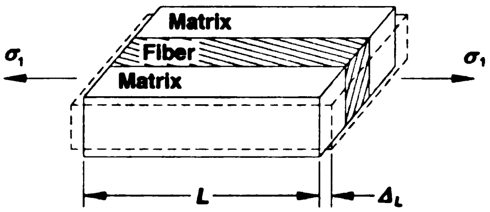

Figure 4.2. Representative volume element for loading in the 1-direction

The rule of mixtures predicts a linear variation of the modulus in the 1-direction for a given fiber volume fraction. Despite the simple form of Equation (4.2.6), its predictions agree well with experimental tensile tests (Jones 1999, Gibson 1994). The results from the rule of mixtures also agree well with the unidirectional carbon/unsaturated polyester material tested in the experimental program of this study (Figure 4.3).

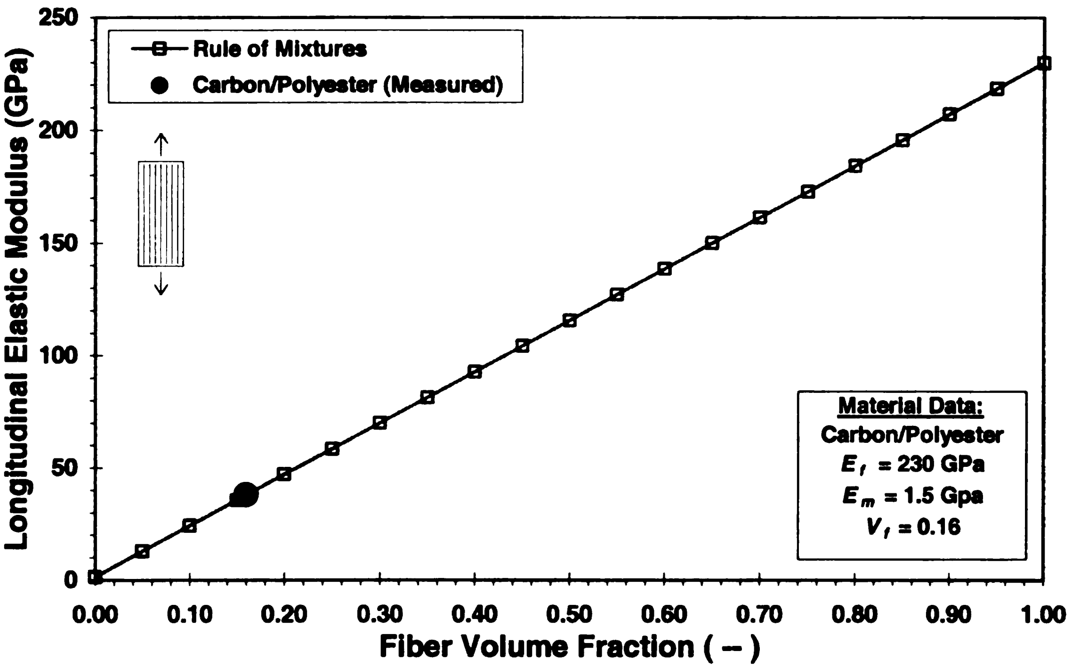

Figure 4.3. Predicted versus measured E_1

Consider next the apparent Young's modulus in the 2-direction (Figure 4.1). In the mechanics of materials approach the transverse stress, σ_2, is assumed to be applied to both the fiber and matrix (Figure 4.4). However, unlike the modulus in the 1-direction, it cannot be assumed that the strains in the fiber and matrix are the same. Thus, the strains in the fiber and matrix are found from the stresses, that is:

$$\varepsilon_f = \frac{\sigma_2}{E_f} \qquad \varepsilon_m = \frac{\sigma_2}{E_m}. \tag{4.2.7,b}$$

It is assumed that that transverse dimension over which, ε_f acts is $V_f W$, while ε_m acts on $V_m W$ (Figure 4.4). Accordingly, the total transverse deformation is:

$$\Delta W = \varepsilon_2 W = V_f W \varepsilon_f + V_m W \varepsilon_m, \tag{4.2.8}$$

or dividing through by the width W:

$$\varepsilon_2 = V_f \varepsilon_f + V_m \varepsilon_m. \tag{4.2.9}$$

Using Equation (4.2.9), and substituting Equation (4.2.7) for the fiber and matrix strains the total strain in the 2-direction becomes:

$$\varepsilon_2 = V_f \frac{\sigma_2}{E_f} + V_m \frac{\sigma_2}{E_m}. \tag{4.2.10}$$

Using Equation (4.2.10), and noting that

$$\sigma_2 = E_2 \varepsilon_2, \tag{4.2.11}$$

the stress in the 2-direction is:

$$\sigma_2 = E_2 \left(V_f \frac{\sigma_2}{E_f} + V_m \frac{\sigma_2}{E_m} \right). \tag{4.2.12}$$

By adding the bracketed terms and dividing through by σ_2, the apparent Young's modulus of the composite material in the 2-direction is:

$$E_2 = \frac{E_f E_m}{V_m E_f + V_f E_m}. \tag{4.2.13}$$

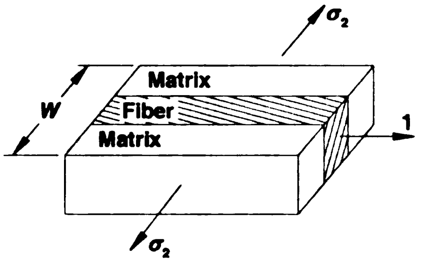

Figure 4.4. Representative volume element for loading in the 2-direction

Predicted results for both E_1 and E_2 are plotted with fiber volume fraction in Figure 4.5. It can be seen from Figure 4.5 that that fiber stiffness has very little effect on the modulus in the 2-direction. Notice that 55% fiber volume fraction is required to raise E_1/E_m to 2, while only 10% is needed to raise E_1/E_m to 2. Thus, the composite modulus E_2 is a matrix-dominated material property.

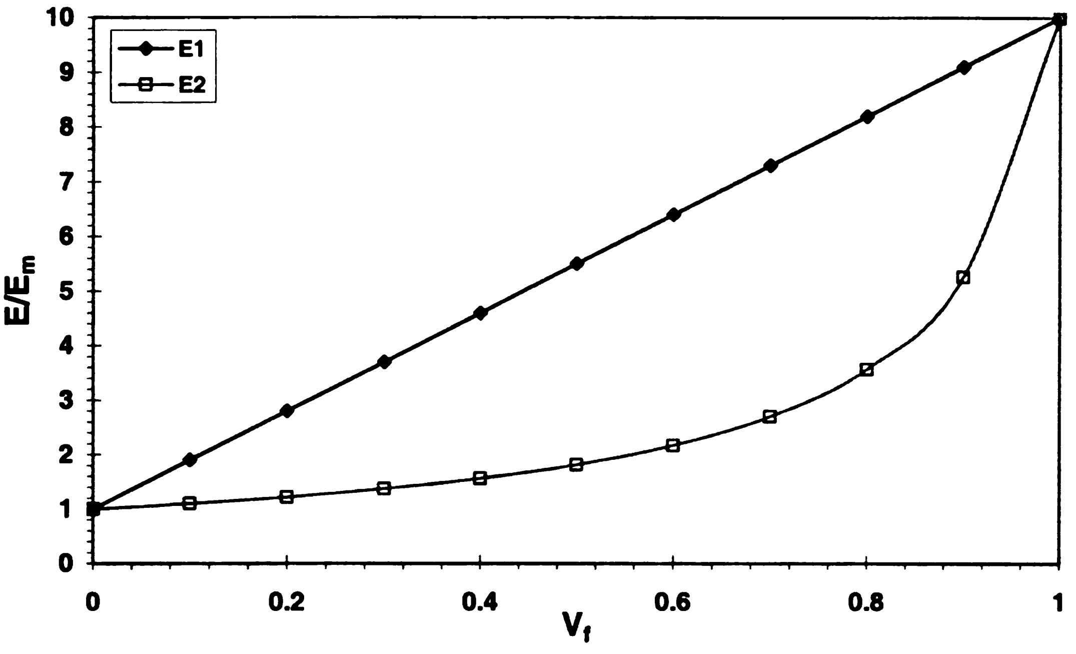

Figure 4.5. Variation of composite moduli with fiber volume fraction

Consider next the major Poisson's ration ν_{12} (Figure 4.1). The Poisson's ratio in the 12-direction is defined as:

$$\nu_{12} = -\frac{\varepsilon_2}{\varepsilon_1}, \tag{4.2.14}$$

for an applied stress σ_1 in the 1-direction, with all other stresses equal to zero. The major Poisson's ratio of the composite material can be obtained using an approach similar to the derivation used for E_1 (Figure 4.6). Again, the strains in the 1-direction are assumed to be equal in the fiber and matrix. For the representative volume element shown in Figure 4.6, the deformation in the transverse direction, Δ_W, is

$$\Delta_W = -W\varepsilon_2 = W\nu_{12}\varepsilon_1. \tag{4.2.15}$$

Also, on the microscopic level, the deformation in the transverse direction is

$$\Delta_W = \Delta_{mW} + \Delta_{fW}. \tag{4.2.16}$$

It is assumed that that transverse dimension over which, ε_f acts is V_fW, while ε_m acts on V_mW (Figure 4.6), as assumed in the derivation of E_2. Thus, the transverse deformations in the fiber and matrix are:

$$\Delta_{mW} = WV_m\nu_m\varepsilon_1 \qquad \Delta_{fW} = WV_f\nu_f\varepsilon_1 . \tag{4.2.17a,b}$$

Using Equations (4.2.15) – (4.2.17), and dividing through by $\varepsilon_1 W$ the major Poisson's ratio of the composite material is:

$$\nu_{12} = \nu_m V_m + \nu_f V_f . \tag{4.2.18}$$

The result is a rule of mixture for the major Poisson's ratio, which gives a linear variation with fiber volume fraction. Because the Poisson's ratio of the fiber ν_f and matrix ν_m are not considerably different, the major Poisson's ratio of the composite material is neither matrix, or fiber-dominated.

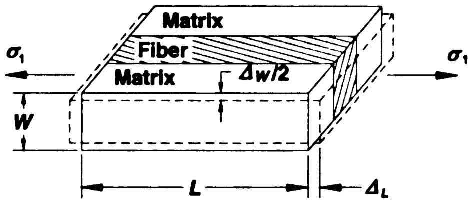

Figure 4.6. Representative volume element loaded in the 1-direction

Consider now the in-plane shear modulus, G_{12}, of the composite material. The shearing stresses on the on the fiber and matrix are the same. Because of the difference in shear modulus between the fiber and matrix the shear deformations occur as shown in Figure 4.7. Assuming a linear stress-strain behavior, the shear strains in the matrix and fiber are:

$$\gamma_m = \frac{\tau}{G_m} \qquad \gamma_f = \frac{\tau}{G_f} . \tag{4.2.19a,b}$$

Following the usual approach, the total shearing deformation is composed of approximately

$$\Delta_m = WV_m\gamma_m \qquad \Delta_{fW} = WV_f\gamma_f\,. \tag{4.2.20a,b}$$

Since the total deformation is $\Delta = \Delta_m + \Delta_f$, division by W gives:

$$\gamma = V_m\gamma_m + V_f\gamma_f\,, \tag{4.2.21}$$

or using Equation (4.2.19), and noting that

$$\gamma = \frac{\tau}{G_{12}}\,, \tag{4.2.22}$$

Equation (4.2.21) can be written as:

$$\frac{\tau}{G_{12}} = V_m\frac{\tau}{G_m} + V_f\frac{\tau}{G_f}\,. \tag{4.2.23}$$

Solving Equation (4.2.23) for G_{12}, the in-plane shear modulus of the composite material is:

$$G_{12} = \frac{G_fG_m}{V_mG_f + V_fG_m}\,, \tag{4.2.24}$$

which is similar to the expression found for the Young's modulus in the 2-direction E_2. Thus, as with E_2, the in-plane shear modulus G_{12} is a matrix-dominated composite material property.

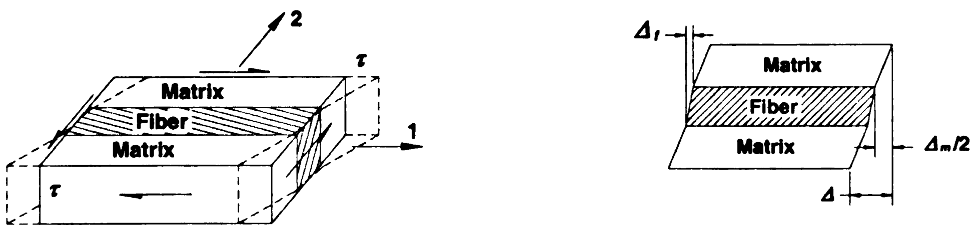

(a) Shear loading in the 12-direction (b) Shear deformations

Figure 4.7. Representative volume element loaded in shear

The results from the mechanics of materials approach to the four elastic moduli of a unidirectional continuous fiber reinforced lamina are shown in Table 4.1. The equations are simple in form and only depend on the moduli of the fiber and matrix, and the fiber volume fraction. These equations are based on the assumption that the fibers are continuous in length. Thus, to model composite materials reinforced with fibers that are discrete in length other models must be used. However, the continuous unidirectional equations are needed to model the face sheet materials used in the experimental studies of Chapters 2 and 3, i.e. the carbon and jute fiber mats, and to establish the upper limit for the short fiber models.

Table 4.1. Orthotropic moduli of a unidirectional fiber-reinforced composite by mechanics of materials

Property	*Expression*
Modulus in the 1-direction	$E_1 = E_f V_f + E_m V_m$
Modulus in the 2-direction	$E_2 = \dfrac{E_f E_m}{V_m E_f + V_f E_m}$
Major Poisson's ratio (12-direction)	$\nu_{12} = \nu_m V_m + \nu_f V_f$
In-plane shear modulus (12-directino)	$G_{12} = \dfrac{G_f G_m}{V_m G_f + V_f G_m}$

4.2.1.2 Properties for Continuous Fiber Composites: Strength

Consider now the strength of a continuous fiber-reinforced composite material in the direction of the fiber. In the mechanics of materials approach it is assumed that all fibers have the same strength and are relatively brittle in comparison to the matrix material, and both the fibers and matrix behave linear elastically (Jones 1999). If the composite material has more that a certain minimum volume fraction of fibers, the ultimate strength of the composite material is reached when the fibers are strained to their maximum stress, i.e.

$$\varepsilon_{c\max} = \varepsilon_{f\max}. \tag{4.2.25}$$

Because the fibers are usually more brittle than the matrix, they cannot elongate as much as the matrix, and thus become the weak component in the composite material. Thus, assuming the fiber strain is equal to the matrix strain in the direction of the fibers, the strength of the composite material is:

$$\sigma_{c\max} = \sigma_{f\max} V_f + E_m(\sigma_{f\max} / E_f) V_m, \tag{4.2.26}$$

where $\sigma_{f\max}$ is the strength of the fiber, E_m is the modulus of the matrix, E_f is the longitudinal modulus of the fiber, and V_f and V_m are the volume fractions of the fibers and matrix, respectively. Notice that the term $\sigma_{f\max}/E_f$ is equal to the failure strain in the fiber, $\varepsilon_{f\max}$, and that multiplying by E_m gives the stress in the matrix at the ultimate fibers strain.

In order for the fibers to have a strengthening effect on the composite material, the fiber volume fraction must be above the critical volume fraction (Jones 1999):

$$V_{fcritical} = \frac{\sigma_{m\max} - E_m(\sigma_{f\max} / E_f)}{\sigma_{f\max} - E_m(\sigma_{f\max} / E_f)}. \tag{4.2.27}$$

For fiber volume fractions below the critical value Equation (4.2.26) is no longer valid. The matrix is then the only contributor to the composite strength, and the fibers act as holes in the matrix. In this case, the strength of the composite is:

$$\sigma_{c\max} = \sigma_{m\max}(1 - V_f). \tag{4.2.28}$$

4.2.2 Aligned Short Fiber Composites

The elastic moduli of an aligned short fiber composite can be estimated using the Halpin-Tsai equations (1969) with a modification proposed by Halpin (1969) that accounts for the fiber aspect ratio (*l/d*). The stiffness in the fiber direction is given by:

$$\frac{E_1}{E_m} = \frac{1+\xi\eta V_f}{1-\eta V_f}, \tag{4.2.29}$$

where

$$\eta = \frac{E_f / E_m - 1}{E_f / E_m + \xi} \tag{4.2.30}$$

$$\xi = 2(l/d). \tag{4.2.31}$$

The predictions from these equations give good agreement with experimental data (Halpin 1969). Halpin concluded that the in-plane shear modulus is not significantly sensitive to the fiber aspect ratio, and may be approximated as:

$$\frac{G_{12}}{G_m} = \frac{1+\xi\eta V_f}{1-\eta V_f}, \tag{4.2.32}$$

where

$$\eta = \frac{G_f / G_m - 1}{G_f / G_m + \xi} \tag{4.2.33}$$

$$\xi = 1.$$

The same argument is made is made for the transverse modulus E_2, and the major Poisson's ratio ν_{12}. The transverse modulus is then approximated as:

$$\frac{E_2}{E_m} = \frac{1+\xi\eta V_f}{1-\eta V_f}, \tag{4.2.34}$$

where

$$\eta = \frac{E_f / E_m - 1}{E_f / E_m + \xi} \tag{4.2.35}$$

$$\xi = 2$$

The major Poisson's ratio is close to the result given by the rule of mixtures, and can be approximated using Equation (4.2.18).

The variation of the longitudinal modulus with fiber aspect ratio for a green hemp-polyester composite using the Halpin-Tsai equations is shown in Figure 4.8. For low fiber aspect ratios, there is a significant reduction in the longitudinal modulus, but as the aspect ratio increases the modulus approaches the rule of mixtures. For natural fibers, typical aspect ratios range from 50 to 500 depending on the length the fibers are chopped to during processing (Mohanty et al. 2000).

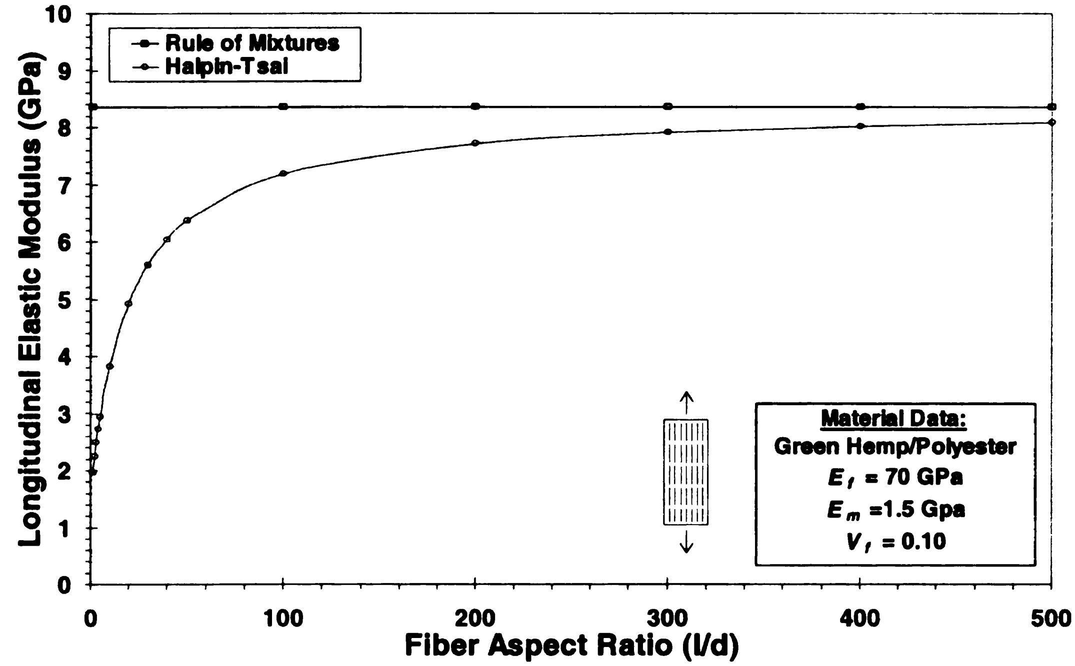

Figure 4.8. Variation of the longitudinal modulus of an aligned short fiber composite with fiber aspect ratio, using the Halpin-Tsai equation

The strength of an aligned short fiber composite can be estimated using the model by Piggott (1980), which accounts for the fiber aspect ratio and the fiber-matrix interfacial shear stress. Consider the geometry of deformation in the representative volume element shown in Figure 4.9. The stiffness mismatch between fiber and matrix

($E_m << E_f$) leads to large shear deformations near the fiber ends but no shear deformations at the mide of the fiber (Figure 4.9). The stress transfer between the matrix and fiber occurs primarily through interfacial shear, which is greatest near the fiber ends, and zero near the center (Figure 4.10). Conversely, the normal stress in the fiber ramps from a minimum near the ends to a maximum near the center of the fiber (Figure 4.10). Piggott developed prediction models for the strength of a short fiber composite and the stress-strain behavior considering these concepts.

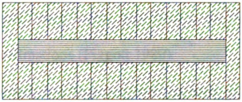

Before Deformation

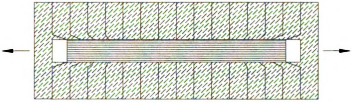

After Deformation

Figure 4.9. Schematic representation of matrix shear deformations in a short fiber composite

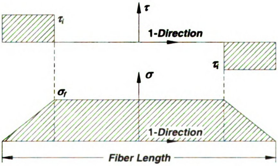

Figure 4.10. Single fiber composite element showing the fiber-matrix interfacial stress and the fiber internal stress for stress transfer by slip

As with the strength of a continuous fiber-reinforced composite, in order for the fibers to have a strengthening effect on the composite material the fiber volume fraction must be above a critical fraction. The critical fiber aspect ratio for the model by Piggott is given by:

$$s_c = \sigma_{f\max} / 2\tau_i, \tag{4.2.36}$$

where τ_i is the fiber-matrix interfacial shear stress. The interfacial shear stress may be assumed to be $\tau_i = \sigma_{m\max} / 2$ when experimental data is not available (Piggott 1980). This assumption for the interfacial shear stress may lead to an over estimate of the actual value, but is sufficient for estimations (Piggott 1980).

The composite strength for fiber volume fractions greater that or equal to the critical ratio is given by:

$$\sigma_{c\max} = \sigma_{f\max}[V_f(1 - s_c / 2s) + V_m E_m / E_f], \tag{4.2.37}$$

where s is the actual fiber aspect ratio l/d. For fiber aspect ratios less than the critical ratio, the composite strength is given by:

$$\sigma_{c\max} = V_f s \tau_i + V_m \sigma_{m\max}. \tag{4.2.38}$$

The variation of the longitudinal strength with fiber aspect ratio for a green hemp-polyester composite using Piggott's model is shown in Figure 4.11. For low fiber aspect ratios there is a significant reduction in the longitudinal strength, but as the aspect ratio increases the modulus approaches the rule of mixtures prediction.

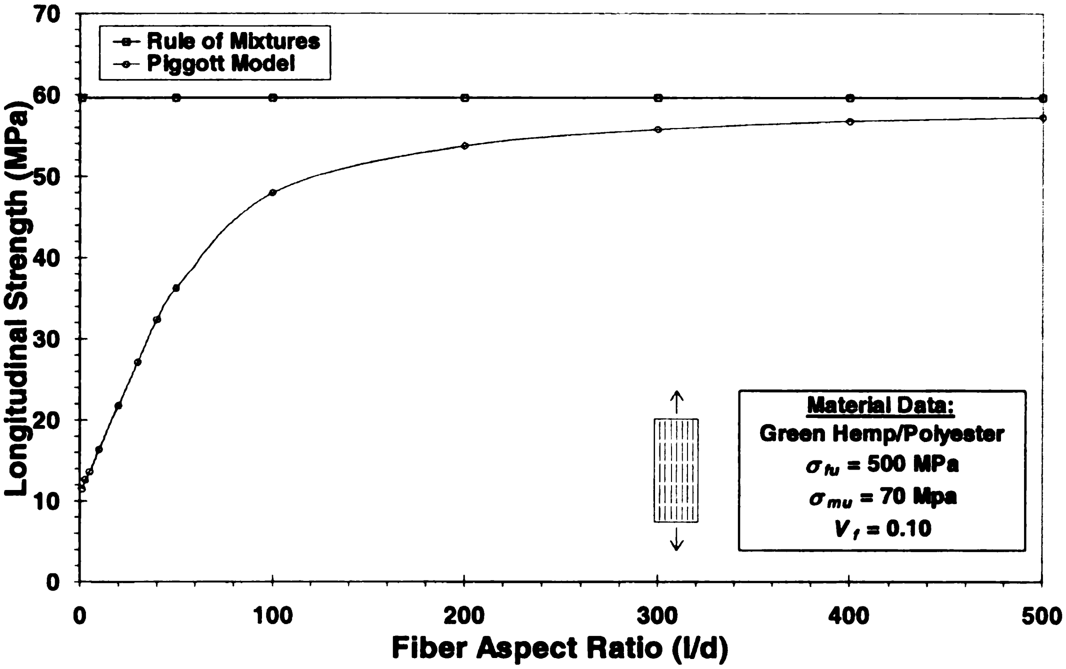

Figure 4.11. Variation of the longitudinal strength of an aligned short fiber composite with fiber aspect ratio, using the model by Piggott

Piggott also derived a model for the stress-strain curve of an aligned short fiber composite, which accounts for the fiber aspect ratio and the fiber-matrix interfacial slip. The stress-strain relation is given as:

$$\sigma_1 = (V_f E_f + V_m E_m)\varepsilon_1 - \frac{V_f E_f^2 \varepsilon_1^2}{4\tau_i s}, \qquad (4.2.39)$$

where σ_1 and ε_1 are the composite stress and strain in the longitudinal direction, respectively. Stress-strain curves for varying fiber aspect ratios are plotted in Figure 4.12. For lower fiber aspect ratios both strength and stiffness decrease, and the stress-strain curve becomes non-linear near failure due to slip between the fibers and matrix (Figure 4.12). For large aspect ratios (*l/d*>1000) the results approach a linear curve, as predicted by the rule of mixtures.

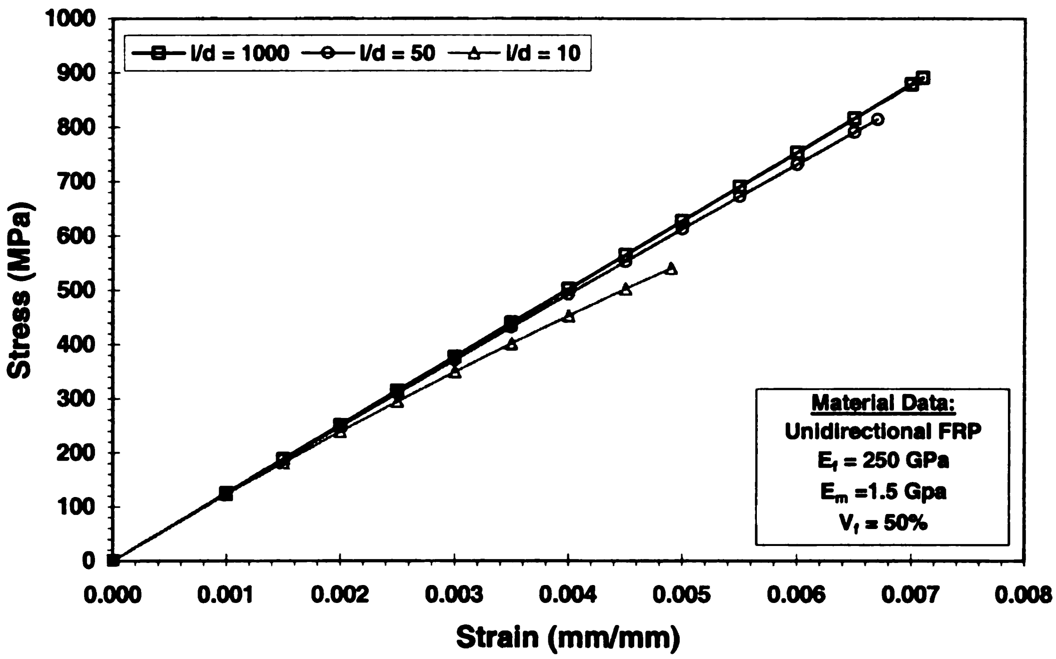

Figure 4.12. Effect of fiber aspect ratio on the stress-strain response of short fiber composites

4.2.3 Randomly Oriented Short Fiber Composites

The fiber alignment in a randomly oriented fiber composites can by truly random in a three-dimensional sense, or random in only two-dimensions. A three-dimensional orientation is likely to exist when the length is much less than the thickness of the part, or when low aspect ratio reinforcement such as whisker and microfibers are used. However, a two-dimensional fiber orientation is more common in many short fiber composites where the fiber length is much longer that the thickness of the part. In this situation fiber orientation in the thickness direction is not possible. The analysis of the isotropic elastic constants E, ν, G, and strength σ_c for the two-dimensional case will be presented, as biocomposite materials tested in the material experimental program fall into this category of fiber orientation.

4.2.3.1 Properties for Randomly Oriented Short Fiber Composites: Stiffness

Halpin and Pagano (1969) have obtained the isotropic elastic constants of a randomly oriented fiber composite by approximating the composite as a quasi-isotropic laminate. Using the invariant properties of the laminate stiffness matrix (Jones 1999), Halpin and Pagano expressed the elastic constants of the random fiber composite as:

$$E = 4U_5(U_1 - U_5)/U_1 \qquad (4.2.40)$$

$$\nu = (U_1 - 2U_5)/U_1 \qquad (4.2.41)$$

$$G = U_5, \qquad (4.2.42)$$

where the invariants are in terms of the engineering constants of the equivalent unidirectional material from which the laminate is constructed. The invariant terms are:

$$U_1 = (3Q_{11} + 3Q_{22} + 2Q_{12} + 4Q_{66})/8 \qquad (4.2.43)$$

$$U_5 = (Q_{11} + Q_{22} - 2Q_{12} + 4Q_{66})/8, \qquad (4.2.44)$$

with lamina stiffness coefficients:

$$Q_{11} = E_1/(1 - \nu_{12}\nu_{21}) \qquad (4.2.45)$$

$$Q_{22} = E_2/(1 - \nu_{12}\nu_{21}) \qquad (4.2.46)$$

$$Q_{12} = \nu_{12}Q_{22} = \nu_{21}Q_{11} \qquad (4.2.47)$$

$$Q_{66} = G_{12}, \qquad (4.2.48)$$

for an orthotropic material. The orthotropic elastic constants E_1, E_2, ν_{12}, and G_{12} of a randomly oriented fiber composite can be determined using a micromechanics approach. Thus, to model a randomly oriented short fiber composite, micromechanics equations that account for the fiber aspect ratio are used. Halpin and Pagano used the Halpin-Tsai equations to model the orthotropic elastic properties of a randomly oriented short fiber composite and found the predictions to be in good agreement with experimental results for a boron/epoxy composite.

Tsai and Pagano (1968) used Equations (4.2.40)-(4.2.42), and related them to the moduli of an orthotropic material to develop the following approximate expressions:

$$E = \frac{3}{8}E_1 + \frac{5}{8}E_2 \tag{4.2.49}$$

$$G_{12} = \frac{1}{8}E_1 + \frac{1}{4}E_2 . \tag{4.2.50}$$

These simple equations can be used with micromechanics equations for E_1, E_2, ν_{12}, and G_{12} that account for the fiber aspect ratio to model a randomly oriented short fiber composite.

The isotropic elastic modulus of a randomly oriented fiber composite can be modeled by assuming the composite consists of a large number of superimposed unidirectional layers. Each layer is characterized by its fiber orientation θ and the layer behavior is fully additive over all layers. Thus, the elastic modulus can be modeled by geometrically averaging the properties of the unidirectional layers over all the fiber orientations (Gibson 1994). This approach is equivalent to the "rule of mixtures" for a randomly oriented fiber composite. Using geometric averaging the modulus is given by

$$E = \frac{\int_0^{\pi/2} E(\theta)d\theta}{\int_0^{\pi/2} d\theta}, \tag{4.2.51}$$

where $E(\theta)$ is the one-dimensional elastic modulus of the θ-ply. Assuming a uniform distribution of fibers over all orientations, Equation (4.2.51) reduces to:

$$E = \frac{2}{\pi}\int_0^{\pi/2} E(\theta)d\theta . \tag{4.2.52}$$

For situations where the fiber orientation is known to be non-uniform, fiber orientation density functions have been developed for non-uniform orientations (Giurgiutiu and Reifsnider 1994). Using the one-dimensional macromechanics analysis of layered composites (Jones 1999), the off-angle lamina elastic modulus is:

$$E(\theta)=\left[\frac{1}{E_1}\cos^4\theta+\frac{1}{E_2}\sin^4\theta+\left(\frac{1}{G_{12}}-2\frac{\nu_{12}}{E_1}\right)\cos^2\theta\sin^2\theta\right]^{-1}, \qquad (4.2.53)$$

where the orthotropic moduli for short fiber composites can be used to model a randomly oriented short fiber composite.

While the previous approach to modeling a randomly oriented fiber composite as quasi-isotropic laminate led to practical equations, the geometric averaging approach leads to a complicated integral for composite stiffness. The integration of Equation (4.2.52) can be evaluated using mathematical software (e.g., MATLAB [2003], Mathcad [2001], Mathematica [2002], etc.). Despite this, geometric averaging can only be used to model the extensional elastic modulus of a randomly oriented fiber composite, and cannot model the shear modulus, G, or the Poisson's ratio, ν, as in the quasi-isotropic model.

Christensen and Waals (1972) also used the geometric averaging approach to develop closed form equations for the isotropic elastic constants for a randomly oriented fiber composite. Using a geometric averaging approach, Christensen and Waals found the elastic modulus and Poisson's ratio of the randomly oriented fiber composite to be:

$$E=\frac{1}{u_1}\left(u_1^2-u_2^2\right) \qquad (4.2.54)$$

$$\nu=\frac{u_1}{u_2}, \qquad (4.2.55)$$

where:

$$u_1 = (3/8)E_1 + \frac{G_{12}}{2} + \frac{(3+2\nu_{12}+3\nu_{12}^2)G_{23}K_{23}}{2(G_{23}+K_{23})} \tag{4.2.56}$$

$$u_2 = (1/8)E_1 - \frac{G_{12}}{2} + \frac{(1+6\nu_{12}+\nu_{12}^2)G_{23}K_{23}}{2(G_{23}+K_{23})}, \tag{4.2.57}$$

and G_{23} is the shear modulus in the 2-3 plane, and K_{23} is the bulk modulus in the 2-3 plane with $\varepsilon_{11} = 0$. Christensen and Waals used micromechanics equations based on composite cylinders to calculate G_{23}, and K_{23} as:

$$\frac{G_{23}}{G_m} = 1 + \frac{V_f}{\dfrac{G_m}{G_f + G_m} + \dfrac{[k_m + (7/3)G_m]V_m}{2(k_m + (4/3)G_m)}} \tag{4.2.58}$$

$$K_{23} = k_m + G_m/3 + \frac{V_f}{\dfrac{1}{k_f - k_m + (1/3)(G_f - G_m)} + \dfrac{V_m}{k_m + (4/3)G_m}}. \tag{4.2.59}$$

Equations (4.2.54) and (4.2.55), or the equations shown in the previous sections can be used to calculate the remaining elastic constants E_1 and ν_{12}. The shear modulus for the isotropic randomly oriented fiber composite can then be calculated using the extensional elastic modulus and the Poisson's ratio by the conventional elasticity relation (Jones 1999):

$$G = \frac{E}{2(1+\nu)}. \tag{4.2.60}$$

4.2.3.2 Properties for Randomly Oriented Short Fiber Composites: Strength

The geometric averaging approach was also used by Baxter (1992) to model the strength of a randomly oriented fiber composites. The model is based on the Tsai-Hill equation, which describes the strength of the θ-ply of an aligned fiber composite as:

$$\sigma(\theta)=\left[\frac{1}{\sigma_1^2}\cos^4\theta+\frac{1}{\sigma_2^2}\sin^4\theta+\left(\frac{1}{\tau^2}-\frac{1}{\sigma_1}\right)\cos^2\theta\sin^2\theta\right]^{-1/2} \tag{4.2.61}$$

where σ_1 is the strength in the fiber direction, σ_2 is the transverse strength, and τ is the shear strength of the composite. A short fiber composite can be modeled by using an equation for σ_1, which accounts for the fiber aspect ratio. The upper limit of composite strength is calculated by assuming a strong interfacial bond is formed such that the shear strength and interfacial shear strength are equal to the matrix shear strength:

$$\tau=\tau_i=\tau_m\,. \tag{4.2.62}$$

The same assumption is made for the transverse strength σ_2:

$$\sigma_2=\sigma_{m\,\max}\,. \tag{4.2.63}$$

A more realistic assumption for the transverse strength, which accounts for slip between the fibers and matrix, is to approximate the fiber as a cylindrical hole in the matrix:

$$\sigma_2=\sigma_{m\,\max}\left[1-2(V_f/\pi)^{1/2}\right]. \tag{4.2.64}$$

The strength of a randomly oriented short fiber composite is then calculated using Equations (4.2.62)-(4.2.64) and a geometric averaging approach similar to Equation (4.2.52). Thus, the strength is given by:

$$\sigma_c=\frac{2}{\pi}\int_0^{\pi/2}\sigma(\theta)d\theta\,. \tag{4.2.65}$$

The integration of Equation (4.2.65) can be evaluated using mathematical software (e.g., MATLAB [2003], Mathcad [2001], Mathematica [2002], etc.).

Lees (1968) also used the geometric averaging approach to develop models for the strength of randomly oriented fiber composites. Lees assumed there are three failure mechanisms according to the Maximum Stress Criterion, each operating over an angle range as follows:

$$\text{for } 0 \le \theta \le \theta_1: \qquad \sigma_c = \frac{\sigma_1}{\cos^2\theta}, \tag{4.2.66}$$

$$\text{for } \theta_1 \le \theta \le \theta_2: \qquad \sigma_c = \frac{\tau}{\sin\theta\cos\theta}, \tag{4.2.67}$$

$$\text{and for } \theta_2 \le \theta \le \pi/2: \qquad \sigma_c = \frac{\sigma_2}{\sin^2\theta}. \tag{4.2.68}$$

Lees then assumed that, for a randomly oriented fiber composite, the average strength over all angles is given by:

$$\sigma_c = \frac{2}{\pi}\left[\int_0^{\theta_1}\frac{\sigma_1}{\cos^2\theta}d\theta + \int_{\theta_1}^{\theta_2}\frac{\tau}{\sin\theta\cos\theta}d\theta + \int_{\theta_2}^{\pi/2}\frac{\sigma_2}{\sin^2\theta}d\theta\right]. \tag{4.2.69}$$

After evaluating the above integral, Lees found the composite strength to be:

$$\sigma_c = \frac{2\tau}{\pi}\left(1 + \frac{\sigma_2}{\sigma_{m\max}} + \ln\frac{\sigma_2\sigma_{m\max}}{\tau^2}\right). \tag{4.2.70}$$

Chen (1971) modified Lees' equation by using a strength efficiency factor to account for the effect of the fiber aspect ratio on the composite strength. The modified equation is:

$$\sigma_c = \frac{2\tau}{\pi}\left(1 + \frac{\sigma_2}{\sigma_{m\max}} + \ln\frac{\psi\sigma_2\sigma_{m\max}}{\tau^2}\right), \tag{4.2.71}$$

where the strength reduction factor ψ is the ratio of the strength of an aligned short fiber composite to the strength of an equivalent continuous unidirectional composite.

4.2.4 Comparison with Measured Material Properties

The randomly oriented short fiber composite models presented in the previous sections are used to model the properties of the biocomposite material systems tested in the material experimental program of Chapter 2. The stiffness of the biocomposite material systems was predicted using the following analytical models: (i) the Halpin-Pagano quasi-isotropic approximation, (ii)\ the Tsai-Pagano approximate equation, (iii) the geometric averaging approach, and (iv) the model by Christensen-Waals. For the stiffness models, the orthotropic elastic constants were calculated using the Halpin-Tsai equations to account for the fiber aspect ratio. The strength of the biocomposite material systems was predicted using the following analytical models: (i) geometric averaging approach, and (ii) the model by Lees. For the strength models, the strength in the fiber direction was calculated using the model by Piggott to account for the fiber aspect ratio.

The green hemp/polyester biocomposite material system from Chapter 2, which was manufacturing at three fiber volume fractions (10%, 13%, and 20%), was first used to evaluate the analytical models for stiffness and strength. Based on the performance of the analytical models, one model was selected and used to predict the properties of the biocomposite material systems.

4.2.4.1 Evaluation of Analytical Models: Stiffness

Results from the modulus of elasticity tests for the green hemp/polyester material system of Chapter 2 are compared with analytical predictions in Figure 4.13 and Figure 4.14. In general, the results from all analytical models are in agreement with the measured results (Figure 4.15) and show similar trends for increasing fiber volume fractions (Figure 4.13). More specifically, the prediction of the geometric averaging approach underestimates the measured results, whereas the predictions of the Christensen-Waals model overestimates the measured results. Both the Halpin-Pagano model and the Tsai-Pagano model agree well with the measured results, with the Halpin-Pagano model matching the best for all fiber volume fractions (Figure 4.15). Based on these results, the Halpin-Pagano model was chosen to model the modulus of elasticity the remaining biocomposite material systems from Chapter 2.

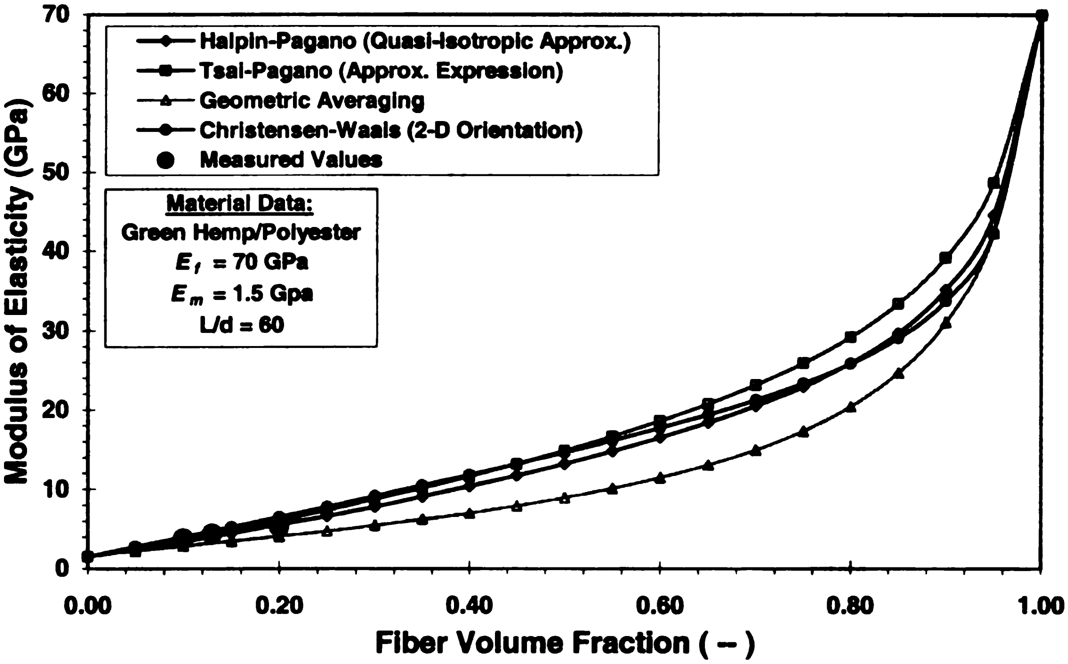

Figure 4.13. Comparison of measured elastic modulus of a green hemp/polyester biocomposite with analytical predictions

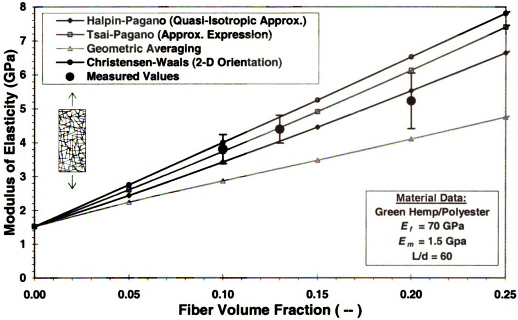

Figure 4.14. Comparison of measured elastic modulus of a green hemp/polyester biocomposite with analytical predictions, zoomed in view

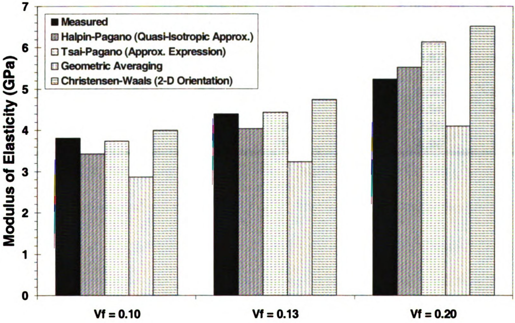

Figure 4.15. Results of the analytical models compared with the measured elastic modulus of a green hemp/polyester biocomposite

The Halpin-Pagano model was used with the Halpin-Tsai equations to predict the elastic modulus of the biocomposite material systems from Chapter 2. The measured and predicted results are provided in Table 4.2 and shown in Figure 4.16. The analytical predictions show good agreement with the measured results, except for the E-glass/polyester composite. The E-glass fibers used were sized (treaded for improved adhesion) for polyester, which may account for the underestimation by the analytical model. The analytical predictions also show some deviation from the results of the unprocessed green hemp/polyester and the raw hemp/polyester composites. These results may be due to inaccurate measurements of the fiber lengths and diameters, or the randomness in the properties of the natural fibers.

Table 4.2. Measured modulus of elasticity of biocomposite material systems compared with results from the Halpin-Pagano quasi-isotropic approximation

Sample	*E measured* (GPa)	*V_f* (%)	*L/d* (--)	*E predicted* (GPa)	*% Error* (%)
Green Hemp/UPE - 13wt.%	3.81	10	60	3.29	14%
Green Hemp/UPE - 17wt.%	4.40	13	60	3.87	12%
Green Hemp/UPE - 25wt.%	5.23	20	60	5.27	1%
Unprocessed Green Hemp/UPE	8.65	25	125	6.90	20%
Raw Hemp/UPE	6.15	15	100	4.54	26%
Flax/UPE	3.37	30	15	3.20	5%
E-Glass/UPE	7.80	15	467	4.96	36%

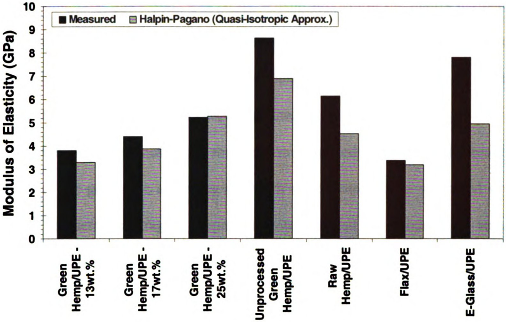

Figure 4.16. Measured modulus of elasticity of biocomposite material systems compared with results from the Halpin-Pagano quasi-isotropic approximation

4.2.4.2 Evaluation of Analytical Models: Strength

The results from the tensile strength tests of the green hemp/polyester material system of Chapter 2 are compared with analytical predictions using geometric averaging (Baxter 1992) and Lees' model (1968) in Figure 4.17. In general, the results show similar trends for increasing fiber volume fractions, but both analytical models overestimate the measured results (Figure 4.17). The overestimation in the strength may be due to defects in the surface of the samples, which can lead to premature failure. In addition, the measured tensile strength may be low due to impurities, such as the wood like core material present in the natural fibers. These impurities may also lead to premature failure, or poor fiber-matrix adhesion, which reduce the composite material strength. The overestimation of the analytical predictions may also be due to the value of the interfacial shear strength assumed in the model by Piggott. The shear strength at the fiber-matrix interface was assumed to be the tensile strength of the matrix divided by 2, as recommended by Piggott. However, this assumption may have overestimated the actual interfacial shear strength, which could lead to the overestimation in the tensile strength of the green hemp/polyester biocomposite.

Even though both analytical models overestimated the measured strength, the predictions of the geometric averaging approach were closest to the measured strength. Thus, the geometric averaging approach was selected to model the remaining biocomposite material systems from Chapter 2.

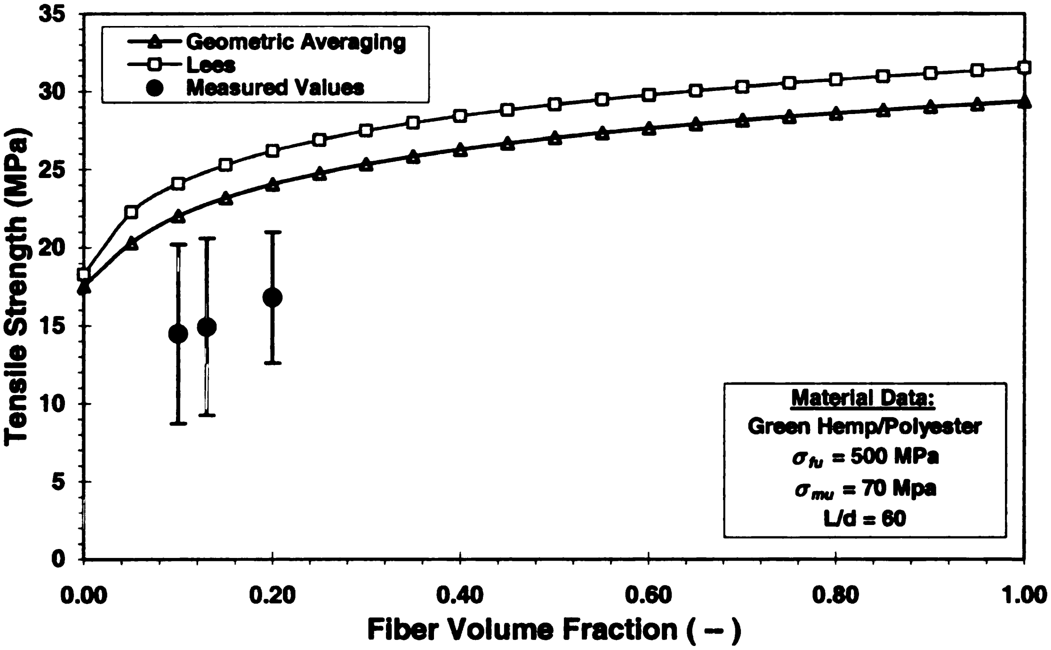

Figure 4.17. Comparison of measured strength of a green hemp/polyester biocomposite with analytical predictions

The geometric averaging approach was used with the Piggott model to predict the tensile strength of the biocomposite material systems from Chapter 2. The measured and predicted results are provided in Table 4.3 and shown in Figure 4.18. Again, the analytical predictions show overestimation of the measured results (Figure 4.18), as expected from the results for the green hemp/polyester results shown in Figure 4.17.

Table 4.3. Measured tensile strength of biocomposite material systems compared with results from geometric averaging

Sample	*σ_{ult} measured* (MPa)	*V_f* (%)	*L/d* (--)	*σ_{ult} predicted* (MPa)	*% Error* (%)
Green Hemp/UPE	14.47	10	60	22.03	52%
Green Hemp/UPE	14.91	13	60	22.77	53%
Green Hemp/UPE	16.79	20	60	25.06	49%
Unprocessed Green Hemp/UPE	10.08	25	125	24.86	147%
Raw Hemp/UPE	19.49	15	100	23.26	19%
Flax/UPE	13.31	30	15	22.55	69%
E-Glass/UPE	34.70	15	467	29.18	16%

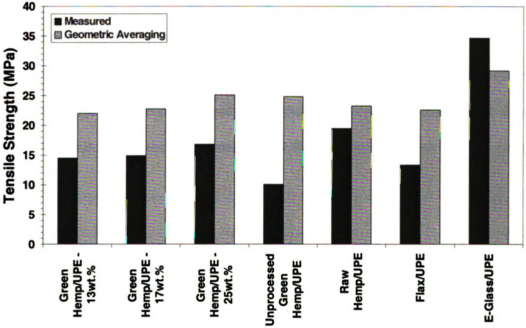

Figure 4.18. Measured tensile strength of biocomposite material systems compared with results from the geometric averaging approach

4.3 Cellular Sandwich Structures

The hierarchical, and hybrid sandwich structures tested in the structural experimental study (Chapter 3) were modeled analytically using conventional mechanics of materials, and the micromechanical models for the biocomposite material systems. In the following sections, the procedure for analyzing the cellular beams and plates is presented, followed by a comparison of the analytical results with the measured results.

4.3.1 Analysis of Cellular Sandwich Structures

The measured flexural stiffness (*EI*) of the cellular beams and pates is compared to analytical results, which are obtained using the micromechanical equations of section 4.2 and conventional mechanics of materials (see Hibbler 1994).

The measured flexural stiffness is first extracted from the measured load-displacement response. From the load-displacement response obtained in the flexural testing of the cellular beams and plates, the stiffness (force per unit displacement) is determined as

$$K = \frac{P}{\delta}, \qquad (4.3.1)$$

where P and δ are the load and displacement at the mid-span section. The measured stiffness can be related to the flexural stiffness using equations that relate displacement to force by the flexural stiffness and the loading geometry. The displacement of a beam loaded in four-point bending is (Hibbler 1994):

$$\delta = \frac{Pa}{48EI}(3L^2 - 4a^2), \qquad (4.3.2)$$

where L is the span length, a is the side span between the reaction and point load, and P is the sum of the two point loads. Solving Equation (4.3.2) for EI, and using Equation (4.4.1), the measured flexural stiffness can be calculated as:

$$EI = K\frac{a}{48}(3L^2 - 4a^2), \tag{4.3.3}$$

where K is measured from the load-displacement response, and L and a are known from the test setup geometry.

The same approach is used to calculate the flexural stiffness of the cellular plates. The displacement of a beam loaded in three-point bending is (Hibbler 1994):

$$\delta = \frac{PL^3}{48EI}. \tag{4.3.4}$$

Solving Equation (4.4.4) for EI and using Equation (4.4.1), the measured flexural stiffness of the cellular plates can be calculated as:

$$EI = K\frac{L^3}{48EI}. \tag{4.3.5}$$

The flexural stiffness was obtained analytically by separately calculating the modulus of elasticity of the material and the moment of inertia of the cross-section, and combining the two terms. The modulus of the biocomposite material systems were calculated using the Halpin-Pagano (1969) quasi-isotropic laminate approximation together with the Halpin-Tsai (1969) equations to determine the orthotropic elastic constants of the material (see Section 4.2).

The moment of inertia of the cellular beams and plates can be calculated using the moment of inertia of the gross cross-section, and subtracting the moment of inertia of the voids in the cellular structure using the parallel axis theorem:

$$I = \bar{I} + Ad^2. \tag{4.3.6}$$

The measured dimensions of the manufactured cellular beams and plates were used to calculate the moment of inertia of each test unit. The face sheet layers in the hybrid cellular plates were transformed to an equivalent biocomposite material for the moment of inertia calculations. The modulus of the face sheet materials was predicted using an appropriate micromechanics material model (e.g., rule of mixtures for the unidirectional carbon).

The analytical failure load for the cellular beams and plates was obtained using conventional mechanics of materials (Hibbler 1994).

The flexural formula can be used to relate the failure stress in the extreme fiber of the section to the failure moment at mid-span as follows:

$$\sigma_f = \frac{M_f y_m}{I}, \tag{4.3.7}$$

where σ_f is the failure stress, M_f is the moment capacity or failure moment, and y_m is the distance to the extreme fiber. Noting that $\sigma = \varepsilon E$, the failure strain in the extreme fiber is:

$$\varepsilon_f = \frac{M_f y_m}{EI}, \tag{4.3.8}$$

where EI can be calculated from the measured flexural test results, y_m can be measured from the test unit, and the failure strain can be obtained from the measured test results of Chapter 2 (see Table 2.9).

The moment in Equation (4.4.8) can then be related to the applied load using basic statics. For a simply supported beam loaded in three-point bending, the bending moment at mid-span is:

$$M = \frac{PL}{4}. \tag{4.3.9}$$

Rearranging the terms in Equation (4.4.9) and assuming linear-elastic behavior up to failure, the failure load is given by:

$$P_f = \frac{4M_f}{L}. \tag{4.3.10}$$

Combining Equations (4.4.8) and (4.4.10), the failure load for the cellular plates is

$$P_f = \varepsilon_f \frac{4EI}{Ly_m}. \tag{4.3.11}$$

For the cellular beams loaded in four-point bending, the bending moment at mid-span is

$$M = \frac{Pa}{2}, \tag{4.3.9}$$

where a is the side span between the reaction and point load, and P is the sum of the two applied point loads. Using the same approach followed to obtain Equation (4.4.11), the failure load for the cellular beams is:

$$P_f = \varepsilon_f \frac{2EI}{ay_m}. \tag{4.3.13}$$

4.3.2 Comparison with Measured Values

The measured and analytically predicted flexural stiffness of the cellular beams are provided in Table 4.4, while the measured and analytically predicted strengths are provided in Table 4.5. The analytical predictions for the flexural stiffness are in good agreement with the measured results. One source of error in the analysis in both the cellular beams and plates could be in the calculation of the moment of inertia. In the moment of inertia calculations it was assumed that the original cellular architecture remained centered, while the excess material was evenly distributed to the top and bottom of the section. This actually may not be the case, which would lead to errors in the calculated moment of inertia of the section. Additional errors could be due to the uncertainty in the analytical models used to predict the modulus of the biocomposite material systems.

Table 4.4. Measured versus predicted flexural stiffness of the biocomposite cellular beams

Material	*Beam ID*	*Fiber Wt. Fraction* (%)	*Measured EI* (GPa-mm^4)	*Predicted EI* (GPa-mm^4)	*Error* (%)
G.Hemp/UPE	CB1	10	188,886	179,805	5%
G.Hemp/UPE	CB2	10	250,557	231,178	8%
G.Hemp/UPE	CB3	10	217,058	219,180	1%

Table 4.5. Measured versus predicted flexural strength of the biocomposite cellular beams

Material	*Beam ID*	*Fiber Wt. Fraction* (%)	*Measured* P_{max} (N)	*Predicted* P_{max} (N)	*Error* (%)
G.Hemp/UPE	CB1	10	670	532	21%
G.Hemp/UPE	CB2	10	813	659	19%
G.Hemp/UPE	CB3	10	677	625	8%

The measured and analytically predicted flexural stiffness of the cellular plates are provided in Table 4.6, while the measured and analytically predicted strengths are provided in

Table 4.7. The results follow the same trend as in the cellular beam results, i.e., the flexural stiffness predictions are in agreement with the measured results but the strength predictions underestimate the measured results. The same sources of error in the cellular beams apply to the cellular plates.

Table 4.6. Measured versus predicted flexural stiffness of the cellular plates

Material	*Beam ID*	*Fiber Wt. Fraction (%)*	*Measured EI (GPa-mm^4)*	*Predicted EI (GPa-mm^4)*	*Error (%)*
G.Hemp/UPE	CP1	10	160,466	140,769	12%
G.Hemp/UPE - Top and Bot. Glass	CP1-G	10	126,358	137,602	9%
G.Hemp/UPE - Bottom Carbon	CP1-C	10	233,919	213,159	9%
G.Hemp/UPE - Top and Bot. Jute	CP1-J	10	122,007	106,633	13%
Raw Hemp/UPE	CP1	10	127,746	146,345	15%
Raw Hemp/UPE	CP2	10	198,210	199,746	1%
Raw Hemp/UPE - T&B Carbon	CP2-C	10	584,919	512,844	12%
Flax/UPE	CP1	20	77,643	79,871	3%
Flax/UPE - T&B Jute	CP1-J	20	102,523	97,205	5%

Table 4.7. Measured versus predicted flexural strength of the biocomposite cellular plates

Material	*Beam ID*	*Fiber Wt. Fraction (%)*	*Measured P_{max} (N)*	*Predicted P_{max} (N)*	*Error (%)*
G.Hemp/UPE	CP1	10	1,483	1,026	31%
G.Hemp/UPE - Top and Bot. Glass	CP1-G	10	2,237	2,759	23%
G.Hemp/UPE - Bottom Carbon	CP1-C	10	10,397	6,569	37%
G.Hemp/UPE - Top and Bot. Jute	CP1-J	10	2,197	1,479	33%
Raw Hemp/UPE	CP1	10	1,859	1,055	43%
Raw Hemp/UPE	CP2	10	2,557	1,308	49%
Raw Hemp/UPE - T&B Carbon	CP2-C	10	11,010	13,449	22%
Flax/UPE	CP1	20	1,172	686	41%
Flax/UPE - T&B Jute	CP1-J	20	1,980	1,335	33%

4.4 Flexural Performance

Engineering design generally seeks to maximize some aspect of performance. Here, performance will mean maximum flexural stiffness or strength for a given weight, but in general performance can be any combination of properties. The performance for a load-bearing component depends on three things: the mode of loading, i.e., tension, bending, twisting, the properties of the material, and the shape of the section (Ashby 1991).

Many materials are available for engineering design, each with a wide range of attributes. The performance of viable materials for a given design criteria can be compared by combining material properties to form *material indices.* Material indices are groupings of material properties which, when maximized, maximize some aspect of performance. The shape of a beam will affect the performance of the beam in bending. That is, hollow box or tube sections are more efficient than solid sections. The efficiency of different shapes can be quantified by defining a dimensionless *shape factor.* The value of the shape factor is not dependent on size, only on the shape of the section. Indices for selecting the performance-maximizing combination of material and shape are defined next using both material indices and shape factors.

In the following sections, material indices, shape factors (material indices that include shape), and micro-structural shape factors for bending stiffness and strength are derived. The derived factors are followed by the measured flexural performance of the cellular beams and tested in the experimental program.

4.4.1 Material Indices

Material properties can be combined to form *material indices,* which are groupings of material properties that, when maximized, maximize some aspect of performance. The indices are derived from the design requirements for a component based on the function, objective, and constraint.

Consider first the material index for a light, stiff beam of stiffness K_B, length l, and of minimum mass m. For the purposes of this derivation the section of the beam will be square (Figure 4.19). However, the results are applicable to any cross-section. The mass of a beam of length l and cross-sectional area A is

$$m = Al\rho, \tag{4.4.1}$$

where ρ is the material density.

The stiffness constraint requires that the bending stiffness of the beam be

$$K_B = \frac{F}{\delta} = \frac{C_1 EI}{l^3}, \tag{4.4.2}$$

where C_l is a constant that depends on the loading configuration, E is the elastic modulus, and I is the moment of inertia about the axis of bending. The moment of inertia of a square section is given by:

$$I = \int y^2 dA = \int_{-b/2}^{b/2} y^2 b \cdot dy = \frac{b^4}{12} = \frac{A^2}{12}. \tag{4.4.3}$$

The constraints are the specified stiffness K_B and length l, while the section area A is free to change.

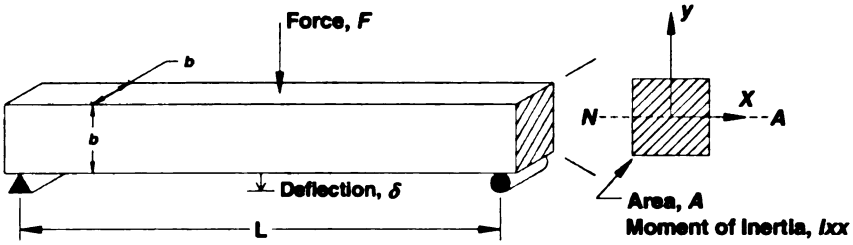

Figure 4.19. A beam of square section, loading in bending about the *x*-*x* axis

The mass of the beam can be reduced by reducing A, but only as long as the stiffness constraint is met. Using Equations (4.4.2) and (4.4.3) to eliminate A in Equation (4.4.1) gives:

$$m = \left(\frac{12K_B}{C_1 l}\right)^{1/2} l^3 \left(\frac{\rho}{E^{1/2}}\right). \tag{4.4.4}$$

In Equation (4.4.4) the first bracketed term is a functional requirement. The next term is the specified geometry (the length l of the beam). The last bracketed term defines the material properties. The most efficient materials for a light, *stiff* beam are those with large values of the material index (Ashby 1999):

$$M_B^e = \frac{E^{1/2}}{\rho}, \tag{4.4.5}$$

where the superscript e denotes elastic and the subscript B denotes bending.

Now, consider the material index for a light, strong beam of length l and minimum mass m to support a specified load F without failing (Figure 4.19). The maximum bending stress is given by

$$\sigma = \frac{My_m}{I}, \tag{4.4.6}$$

where M is the bending moment, I is the moment of inertia of the section about the axis of bending, and y_m is the distance from the neutral axis to the extreme fiber of the beam. The beam will fail when the stress in the extreme fiber exceeds the strength of the material σ_f. Using Equation (4.4.6), the bending moment when the failure stress is reached is given by:

$$M_f = \frac{I\sigma_f}{y_m}. \tag{4.4.7}$$

Noting that the bending moment is equal to the applied load times the length of the beam divided by a constant that accounts for the loading configuration,

$$M_f = \frac{F_f l}{C_2},$$

the failure load is:

$$F_f = C_2 \frac{I\sigma_f}{y_m l}, \tag{4.4.8}$$

where C_2 is a constant that depends on the loading configuration. For the case shown in Figure 4.19, $C_2 = 4$, and $y_m = b/2$. Using Equations (4.4.8) and (4.4.3) to eliminate the area A from Equation (4.4.1) gives:

$$m = \left(\frac{6}{C_2} \frac{F_f}{l^2} \right)^{2/3} l^3 \left(\frac{\rho}{\sigma_f^{\,2/3}} \right). \tag{4.4.9}$$

This is the mass of the beam required to support the failure load. Again, the first bracketed term contains the functional requirements (F_f and l), the middle term represents the specified geometry, and the third bracketed term contains the material properties. The most efficient materials for a light, *strong* beam are those with large values of the material index (Ashby 1999):

$$M_B^f = \frac{\sigma_f^{2/3}}{\rho}, \tag{4.4.10}$$

where the superscript f denotes failure and the subscript B denotes bending.

A comparison of the performance of common materials in bending is given in Table 4.8. Other material design criteria, such as cost, fatigue, and energy absorption, lead to many other indices (Ashby 1999). The material indices work well for comparing materials, but they ignore the shape of the component. Thus, for materials with different cross-sectional shapes other factors must be used to quantify efficiency.

Table 4.8. Material properties and material indices for minimum weight

	Density	*Modulus*	*Strength*	$E^{1/2}/\rho$	$\sigma_f^{2/3}/\rho$
Material	ρ (Mg/m^3)	E (GPa)	σ_f (MPa)		
Wood (spruce)	0.49	15	45	7.9	25.8
Concrete	2.30	25	30	2.2	4.2
Carbon FRP	1.60	100	450	6.3	36.7
Glass FRP	1.78	28	300	3.0	25.2
Steel	7.85	210	1100	1.8	13.6
Aluminum	2.70	69	130	3.1	9.5

4.4.2 Shape Factors

Sections of *shaped* material carry load more efficiently than solid sections do. Here, shaped means that the cross-section is formed in a tube, a box, an I-section, or the like. Efficient means that for a given loading condition the section uses as little material as possible, and is therefore as light as possible. To measure the shape and efficiency of a section, for a given mode of loading, *shape factors* have been developed by Ashby (1999). A shape factor is a dimensionless number that characterizes the efficiency of the shape of a section, regardless of scale, for a given mode of loading.

Consider first the shape factor for the elastic bending of a beam. For a beam of length l and elastic modulus E, the bending stiffness is:

$$K_B = \frac{C_1 EI}{l^3}, \tag{4.4.11}$$

where C_l is a constant that depends on the loading configuration. The shape of the sections influences Equation (4.4.11) through the second moment of area, I, about the axis of bending, or more commonly know as the moment of inertia.

Ashby (1999) defines the shape factor for elastic bending as the ratio of the stiffness K_B of the shaped beam to that of a solid circular section K_B^o (with moment of inertia I^o) with the same cross-section A, and thus the same mass per unit length. Using Equation (4.4.11) the shape factor is given by:

$$\phi_B^e = \frac{K_B}{K_B^o} = \frac{I}{I^o}.$$

For a solid circular section of area A the moment of inertia is:

$$I^o = \frac{\pi r^4}{4} = \frac{A^2}{4\pi}. \tag{4.4.12}$$

Thus, using Equation (4.4.12), the shape factor for elastic bending is:

$$\phi_B^e = \frac{4\pi I}{A^2}, \tag{4.4.13}$$

where the superscript *e* denotes elastic and the subscript *B* denotes bending.

Now, consider the shape factor for failure in bending. Failure of a material can have many definitions. For a ductile material, failure may occur at the onset of plasticity, when the material first reaches its yield strength σ_y. For a brittle material failure occurs when the stress exceeds the fracture strength σ_{fr}. When fatigue is an issue, failure occurs when the endurance limit σ_e is exceeded. The shape factor for failure in bending covers all three modes of failure. Thus, the symbol σ_f will be used to denote the failure stress for yielding, fracture, or fatigue failure.

In bending, the stress is largest in the extreme fiber of the beam, y_m, which is the surface of the beam that lies furthest from the neutral axis. The maximum bending stress is given by

$$\sigma = \frac{My_m}{I} = \frac{M}{S}, \tag{4.4.14}$$

where *M* is the bending moment and *I* is the moment of inertia of the section about the axis of bending. The shape enters Equation (4.4.14) through the section modulus, $S = I/y_m$. If the maximum stress in the beam exceeds the failure stress of the material, the beam will fail. The bending moment when the failure stress is reached is given by:

$$M_f = Z\sigma_f. \tag{4.4.15}$$

Ashby (1999) defines the shape factor for failure in bending as the ratio of the failure moment M_f of the shaped section to that of a solid circular section with the same cross sectional area *A*. Thus, the shape factor is

$$\phi_B^f = \frac{M_f}{M_f^o} = \frac{S}{S^o}. \tag{4.4.16}$$

For a solid circular section of area A the section modulus is

$$S^o = \frac{\pi}{4} r^3 = \frac{A^{3/2}}{4\sqrt{\pi}}. \tag{4.4.17}$$

Thus, using Equation (4.4.16) the shape factor for failure in bending is:

$$\phi_B^f = \frac{4\sqrt{\pi}S}{A^{3/2}}, \tag{4.4.18}$$

where the superscript f denotes failure and the subscript B denotes bending. The two expressions for ϕ_B^e, and ϕ_B^f have the same form, and are often similar in value.

Both shape factors are dimensionless, and depend only on shape. That is, large and small beams have the same shape factor value if their sections have the same shape, and are proportional. Solid, symmetric sections (circles, squares, etc.) will have shape factors close to 1, but elongated or I-shapes can have shape factor values of 15 or more (Table 4.9). These shaped sections are more efficient than the solids shapes in that less material is required to achieve the same bending stiffness and strength.

Table 4.9. Section shape factor (sections of equal area)

Shape	Φ_B^e	Φ_B^f
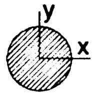	1.0	1.0
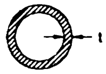	17.4	6.2
	1.1	1.2
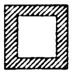	13.8	6.3
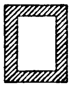	18.0	6.8
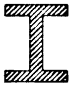	17.0	7.8

- Hollow sections: thickness (t) is constant
- Asymmetrical sections: long axis is 1.5x the short axis

4.4.3 Performance Indices with Shape Factors

The performance-maximizing combination of material and shape for a given mode of loading involves both the material indices and shape factors. Ashby (1999) derived indices for comparing the performance of beams of different materials and shapes.

Consider first the selection of a material for a light stiff beam of stiffness K_B, length l, and minimum mass m, allowing the section-shape to be variable. Using the bending stiffness given in Equation (4.4.11) and replacing I by the shape factor ϕ_B^e in Equation (4.4.13) gives:

$$K_B = \frac{C_1}{4\pi} E \phi_B^e \frac{A^2}{l^3}. \tag{4.4.19}$$

Using Equation (4.4.19) to replace A in Equation (4.4.1) gives the mass of the beam as:

$$m = \left(\frac{4\pi K_B}{C_1 l}\right)^{1/2} l^3 \left(\frac{\rho^2}{\phi_B^e E}\right)^{1/2}. \tag{4.4.20}$$

Thus, the best material-shape combination for a light stiff beam is that with the greatest value of the index

$$M_1 = \frac{\left(E\phi_B^e\right)^{1/2}}{\rho}. \tag{4.4.21}$$

Notice that, for sections of the same shape (i.e. constant ϕ_B^e) the best choice for the lightest beam is the material with the largest value of $E^{1/2}/\rho$, as shown in section 4.4.1.

Consider now the selection of a material for a light strong beam of length l and minimum mass m, to support a specified load F without failing, allowing the section-shape to be variable. Using the failure moment in Equation (4.4.15) and replacing S by the shape factor ϕ_B^f in Equation (4.4.18) gives:

$$M_f = \frac{\sigma_f}{4\sqrt{\pi}} \phi_B^f A^{2/3}. \tag{4.4.22}$$

Using Equation (4.4.22) to replace A in Equation (4.4.1) gives the mass of the beam as:

$$m = \left(4\sqrt{\pi}\frac{M_f}{l^3}\right)^{2/3} l^3 \left(\frac{\rho^{3/2}}{\phi_B^f \sigma_f}\right)^{2/3}. \tag{4.4.23}$$

Then, the best material-shape combination for a light, strong beam is that with the greatest value of the index:

$$M_2 = \frac{\left(\sigma_f \phi_B^f\right)^{2/3}}{\rho}. \tag{4.4.24}$$

For sections of the same shape (i.e. constant ϕ_B^f) the best choice for the lightest beam is the material with the largest value of $\sigma_f^{2/3}/\rho$, as shown in section 4.4.1.

4.4.4 Micro-structural Shape Factors

The efficiency of a macroscopic shape can be improved by introducing shape at a small scale, *microscopic shape*. For example, a rectangular section made of a cellular material (microscopic shape) will have higher efficiency than a solid rectangular section (macroscopic shape). The additional efficiency of the micro-structural shape is characterized by *micro-structural shape factors* (Ashby 1999).

Microscopic shape can be achieved through cellular structures, which are solids made up of an interconnected network of solid struts. The most important characteristic of a cellular structure affecting its mechanical properties is the relative density, ρ^*/ρ_s, i.e. the density of the cellular material, ρ^*, divided by the density of the solid from which the cell walls are made, ρ_s (Gibson and Ashby 1988). The higher the relative density for a cellular structure, the more solid material in the structure, resulting in increased mechanical properties at an increased weight.

Consider first the micro-structural shape factor for bending stiffness. Ashby (1999) defines the micro-structural shape factor ψ similar to the macroscopic shape factor ϕ. If the beam in Figure 4.19 is composed of a micro-structured material, the second moment of the area is:

$$I = \frac{\rho^*}{\rho_S} \int_{-b/2}^{b/2} y^2 b \cdot dy = \frac{\rho^*}{\rho_S} \frac{b^4}{12}, \tag{4.4.25}$$

where a differential element of area dA contains an area of solid materials $(\rho^* / \rho_S) bdy$. The total shape factor that includes both the micro-structural and macro-structural shape of the beam is thus:

$$\left(\phi_B^e\right)^{TOT} = \frac{4\pi I}{A^2} = \left(\frac{\pi}{4}\right)\left(\frac{1}{\rho^*/\rho_S}\right), \tag{4.4.26}$$

where the area of the micro-structured material is $A = (\rho^*/\rho_S)b^2$. The term in the first brackets in Equation (4.4.26) is simply the shape factor ϕ_B^e for the macro-structure of the beam. The second term in brackets is the micro-structural shape factor for bending stiffness:

$$\psi_B^e = \frac{\rho_s}{\rho^*}. \tag{4.4.27}$$

In other words, the micro-structural shape factor here is the inverse of the relative density. Note that, in the limit, for a solid micro-structure ($\rho^* = \rho_S$), ψ_B^e takes the value of 1 as it clearly should. Also, notice the total shape factor is the product of the macro-structural and micro-structural shape factors:

$$\left(\phi_B^e\right)^{TOT} = \phi_B^e \cdot \psi_B^e. \tag{4.4.28}$$

Consider now the micro-structural shape factor for bending strength. If the beam in Figure 4.19 is composed of a micro-structured material, the section modulus is:

$$S = \frac{I}{y_m} = \frac{\rho^*}{\rho_S}\frac{b^4}{12 \cdot b/2} = \frac{1}{6}\frac{\rho^*}{\rho_S}b^3. \tag{4.4.29}$$

where the moment of inertia I is given in Equation (4.4.25). The total shape factor that includes both the micro-structural and macro-structural shape of the beam is thus:

$$\left(\phi_B^e\right)^{TOT} = \frac{4\sqrt{\pi}S}{A^{3/2}} = \frac{2}{3}\sqrt{\pi}\left(\frac{\rho_S}{\rho^*}\right)^{1/2}, \tag{4.4.30}$$

where the area of the micro-structured material is $A = (\rho^*/\rho_S)b^2$. The term in the first brackets in Equation (4.4.30) is simply the shape factor ϕ_B^f for the macro-structure of the beam. The second term in brackets is the micro-structural shape factor for bending strength:

$$\psi_B^f = \left(\frac{\rho_s}{\rho^*}\right)^{1/2}. \tag{4.4.31}$$

The micro-structural shape factor here is proportional to the inverse of the relative density. In the limit, for a solid micro-structure ($\rho^* = \rho_S$), ψ_B^f takes the value of 1, as it should. As with the case of bending stiffness, the total shape factor is the product of the macro-structural and micro-structural shape factors:

$$\left(\phi_B^f\right)^{TOT} = \phi_B^f \cdot \psi_B^f. \tag{4.4.32}$$

Both stiffness and strength micro-structural shape factors show that by introducing micro-structure to a solid shape the performance is increased, resulting in a lighter more efficient structure. This idea of micro-structuring could be extended further by introducing cell walls that are themselves micro-structured, thus creating a structural hierarchy. Such efficient structural hierarchy can be found in nature (Gibson and Ashby 1988, Gunderson and Thorp 1993), but there are limits on the level of hierarchy that can be achieved in man-made structures due to manufacturing difficulties and the accompanying manufacturing costs. Nevertheless, the use of hierarchical structures can further improve the performance of a structural member resulting in light efficient structures.

The effect of micro-structure can also be shown by including the microscopic shape factor into the material performance indices. Considering a cellular structure and using the micro-structural shape factor, the performance index for maximum stiffness of a given weight for a cellular beam is given by Equation (4.4.5) to give:

$$M_B^e = \frac{E^{1/2}}{\rho} = \frac{(E^*)^{1/2}}{\rho^*} = \frac{E_s^{1/2}}{\rho_s}\left(\frac{\rho_s}{\rho^*}\right), \qquad (4.4.33)$$

where the modulus of the cellular material is equal to the modulus of the cellular material times the relative density (Huang and Gibson 1995).

4.4.5 Measured Flexural Performance

The relative performance index of a micro-structured beam using Equation (4.4.33) divided by the performance of a beam of solid material is shown in Figure 4.20. The figure shows the theoretical curve for the biocomposite material system, and is accompanied by the experimental data from the biocomposite cellular beam tests (Chapter 3). Due to manufacturing constraints in the experimental studies, the relative densities studied were very similar. Thus, the experimental data points are only in a limited region of the analytical curve. Nonetheless, the data is consistent with the predicted performance, and shows that it is possible to produce cellular beams with higher values of the performance index than beams of solid material. Further improvements in the mechanical efficiency of cellular beams (and plates) can be achieved at lower relative densities (Figure 4.20). For example, at a relative density of 0.20, the performance index of a cellular beam to a fully dense beam is $(E^{1/2}/\rho)/(E_S^{1/2}/\rho_S) = 2.2$.

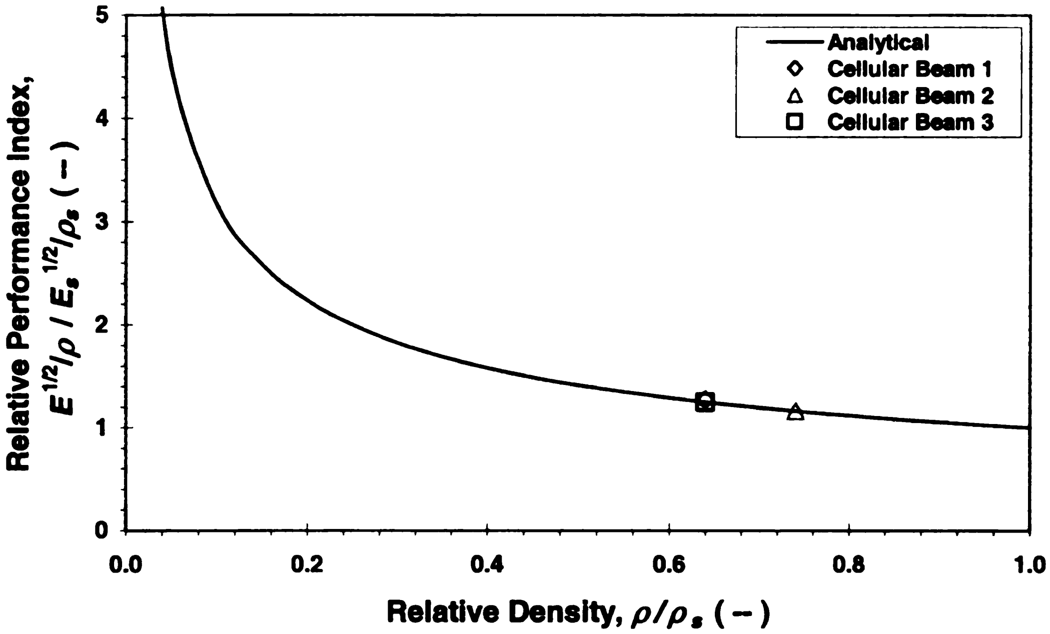

Figure 4.20. Effect of relative density on the relative performance

The measured material performance index, shape factor, and performance index with shape factor for minimum weight, for a given flexural stiffness is shown in Table 4.10. The measured values show the effect of the hierarchical distribution on the performance of the cellular beams. Recall that, cellular beam 1 (CB1) was manufactured with a periodic cellular architecture, while cellular beams 2 and 3 (CB2, and CB3) were manufactured with hierarchical cellular architectures (see Figure 3.4). Again, the manufacturing constraints limited the design of the hierarchical architectures. Thus, the flexural performance is similar for the three cellular beams. Nonetheless, the data shows an improvement in the flexural performance achieved by using efficient cellular structures.

The most efficient cellular beam tested (in terms of flexural stiffness) was CB3, which had a material index of 2.67, shape factor of 0.67, and a material index with shape factor of 2.18. The other hierarchical cellular beam tested, CB2, showed the lowest flexural performance. The results indicate that the hierarchical architecture of CB3 was more efficient than CB2 in concentrating material near the top and bottom of the beam. Thus, the use of hierarchical structures can improve the flexural performance of a cellular beam, provided the hierarchical architecture is correctly designed.

Table 4.10. Measured flexural performance of the biocomposite cellular beams

Material	ID	Fibers by Wt. (%)	$E^{1/2}/\rho$ ($GPa^{1/2}/Mg/m^3$)	Shape Factor ϕ (--)	$(\phi E)^{1/2}/\rho$ ($GPa^{1/2}/Mg/m^3$)
G.Hemp/UPE	CB1	10	2.64	0.65	2.14
G.Hemp/UPE	CB2	10	2.33	0.51	1.66
G.Hemp/UPE	CB3	10	2.67	0.67	2.18

4.5 Hierarchical Cellular Structures

An analysis procedure for the analysis of hierarchical cellular structures was developed through discretization of the material continuum present in the cellular structure. As show in Figure 4.21, a biocomposite hierarchical cellular plate can be thought of as being composed of a series of bonded layers, or lamina, each of them featuring a particular material cellular architecture. Thus, the properties of the entire hierarchical cellular plate, or laminate, can be determined by integrating the properties of each one of the representative cellular material lamina. Each of the cellular lamina layers is considered to feature a governing cellular architecture such that its properties can be determined. The properties of a two-dimensional cellular material can be determined form the cellular microstructure, which includes the material properties of the solid material making the cellular solid and the architecture of the cells. Finally, the properties of the solid biocomposite material can be determined using the properties of randomly oriented short fiber composites. The properties of the biocomposite will depend on the individual properties of the fibers and resin, and the percentage of fibers to resin in the composite.

The structural performance of biocomposite hierarchical cellular plates can thus be determined by integrating the above mentioned levels of analysis (Figure 4.21). This analysis may be used in lieu of the methods presented in section 4.3. However, due to manufacturing constrains that limited the level of hierarchical structure that could be achieved in the cellular beams and plates (Chapter 3), the proposed analysis method could not be verified.

In the subsequent sections a summary of each analysis level is presented beginning with the analysis biocomposite material systems, followed by mechanics of cellular solids, micro-mechanics of a lamina, and lamination theory. The limitations of the analysis procedure are also discussed.

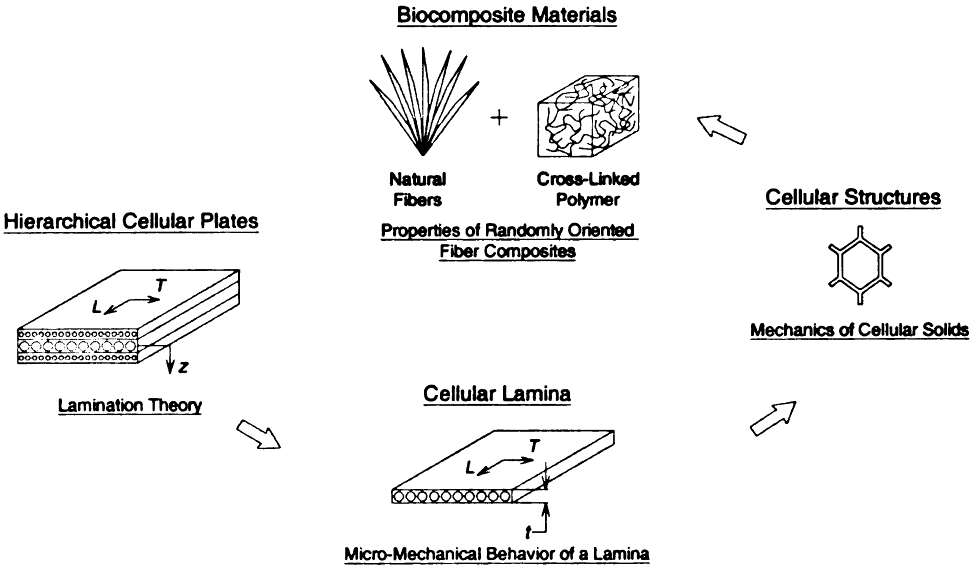

Figure 4.21. Overview of the analysis process for hierarchical hybrid cellular biocomposite beams and plates

4.5.1 Analysis

The proposed analysis procedure begins at the material level with the analysis of the biocomposite material system. The analysis of randomly oriented short fiber composites presented in Section 4.2 can be used to model the biocomposite material system. Based on the comparison with measured results, the quasi-isotropic laminate approximation by Halpin and Pagano (1969) can be used with the Halpin-Tsai (1969) equations to determine the elastic constants of the biocomposite materials.

The next level of analysis is at the microstructural level, where mechanics of cellular solids are used to model the properties of the cellular material layers within the hierarchical structure. While there are several approaches to the mechanics of cellular solids, Gibson and Ashby (1988) have effectively shown that the mechanical properties of cellular solids can be effectively described using structural mechanics to determine their properties such as stiffness and strength.

The properties of a 2-D honeycomb can be described by analyzing the response of a unit hexagonal cell (Figure 4.22). The mechanical response of the cellular solid can then be studied by consideration of its interconnected array of one-dimensional members (Figure 4.22). By loading the unit cell and calculating the resulting deformations in the cell walls Gibson and Ashby (1988) derived equations for the elastic constants of a cellular material. The results are provided in the following equations, where the superscript * refers to the cellular material and the subscript S refers to the solid material from which it is made:

$$E_1^* = E_S \frac{\rho^*}{\rho_S} \approx E_S \frac{t}{l} \qquad (4.5.1)$$

$$E_2^* = E_S\left(\frac{t}{l}\right)^3 \frac{\cos\theta}{(h/l+\sin\theta)\sin^2\theta} \tag{4.5.2}$$

$$E_3^* = E_S\left(\frac{t}{l}\right)^3 \frac{(h/l+\sin\theta)}{\cos^2\theta} \tag{4.5.3}$$

$$\nu_{12}^* = \nu_S \tag{4.5.4}$$

$$\nu_{21}^* = \nu_{12}^* \frac{E_2^*}{E_1^*} \tag{4.5.5}$$

$$G_{12}^* \approx G_S 0.577\left(\frac{t}{l}\right) \tag{4.5.6}$$

The most important characteristic of a cellular structure affecting its mechanical properties is its relative density, ρ^*/ρ_S, i.e., the density of the cellular material, ρ^*, divided by the density of the solid material from which the cell walls are made, ρ_S. The higher the relative density for a cellular structure, the more solid material in the structure, resulting in increased mechanical properties, albeit with increased mass.

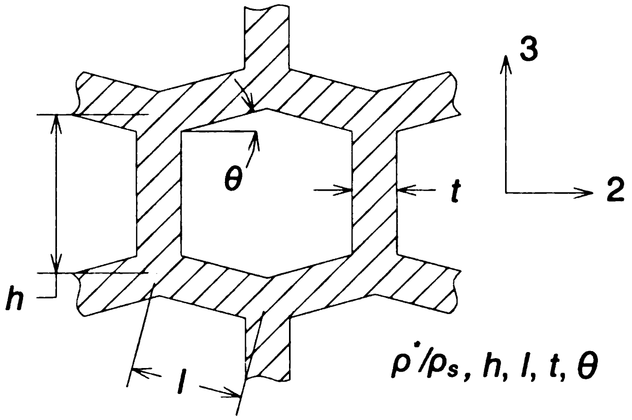

Figure 4.22. Unit cell model for the mechanical behavior of cellular solids

Beams and plates structures with repeating layers of cellular material can be treated as laminated structures (Huang and Gibson 1995) where each layer maybe defined by a characteristic cell architecture. This idealization applies to cellular beams and plates with periodic cells that are oriented in different directions about the longitudinal axis of the element and/or hierarchical cellular structures that feature different levels of cellular architectures along the member depth.

Assuming a plane stress condition for each characteristic layer of cellular material, a lamina of cellular material can be described using the equivalent properties obtained from the mechanics of cellular solids equations proposed by Gibson and Ashby (1988), as previously discussed. The stress-strain relation for the single cellular material layer (lamina) with respect to the material 1-2-3 coordinate system, assuming that the response is at most orthotropic is given by (Jones 1999):

$$\begin{Bmatrix} \sigma_1 \\ \sigma_2 \\ \tau_{12} \end{Bmatrix} = \begin{bmatrix} Q_{11}^* & Q_{12}^* & Q_{16}^* \\ & Q_{22}^* & Q_{26}^* \\ Symm. & & Q_{66}^* \end{bmatrix} \begin{Bmatrix} \varepsilon_1 \\ \varepsilon_2 \\ \gamma_{12} \end{Bmatrix}, \tag{4.5.7}$$

where

$$Q_{11}^* = \frac{E_1^*}{(1-\nu_{12}^*\nu_{21}^*)} \qquad Q_{22}^* = \frac{E_2^*}{(1-\nu_{12}^*\nu_{21}^*)}$$

$$Q_{12}^* = \frac{\nu_{21}^* E_1^*}{(1-\nu_{12}^*\nu_{21}^*)} \qquad Q_{66}^* = G_{12}^*. \tag{4.5.8}$$

The structural properties of a hierarchical cellular beam or plate can then be found by adding the individual stiffnesses of the different characteristic cellular material layers over the depth of the structure. Each layer may have different material properties due to their constituent material, or different cellular architecture or cell orientation. In order to be able to add the stiffnesses of each layer, their properties with respect to a common structural coordinate system (*x*-*y*-*z*) must be determined. This is done by rotating the base material properties given by Equation (4.5.8) through a transformation matrix. Thus, the material response for the layer about any coordinate system $\left[\overline{Q}^*\right]$ within the plane is defined by:

$$\begin{Bmatrix} \sigma_{xx} \\ \sigma_{yy} \\ \tau_{xy} \end{Bmatrix} = \begin{bmatrix} \overline{Q}_{11}^* & \overline{Q}_{12}^* & \overline{Q}_{16}^* \\ & \overline{Q}_{22}^* & \overline{Q}_{26}^* \\ Symm. & & \overline{Q}_{66}^* \end{bmatrix} \begin{Bmatrix} \varepsilon_{xx} \\ \varepsilon_{yy} \\ \gamma_{xy} \end{Bmatrix}, \tag{4.5.9}$$

where

$$\left[\overline{Q}^*\right] = \left[T_2'\right]^T \left[Q^*\right] \left[T_2'\right] \tag{4.5.10}$$

and

$$\left[T_2'\right] = \begin{bmatrix} \cos^2\theta & \sin^2\theta & -2\cos\theta\sin\theta \\ \sin^2\theta & \cos^2\theta & 2\cos\theta\sin\theta \\ \cos\theta\sin\theta & -\cos\theta\sin\theta & (\cos^2\theta - \sin^2\theta) \end{bmatrix}. \tag{4.5.11}$$

Addition of all the layer stiffnesses over the section depth through classical lamination theory (Jones 1999) leads to the section properties of the laminated plate, or the so called [A,B,D] matrix:

$$A_{ij} = \sum_{k=1}^{n} (\overline{Q}_{ij}^*)_k (z_k - z_{k-1}) \tag{4.5.12}$$

$$B_{ij} = \frac{1}{2} \sum_{k=1}^{n} (\overline{Q}_{ij}^*)_k (z_k^2 - z_{k-1}^2) \tag{4.5.13}$$

$$D_{ij} = \frac{1}{3} \sum_{k=1}^{n} (\overline{Q}_{ij}^*)_k (z_k^3 - z_{k-1}^3). \tag{4.5.14}$$

where i = 1, 2, 3 and k = 1, 2, 3...n, for n number of layers. The geometry of the laminate structure is shown in Figure 4.23. In the [*A*,*B*,*D*] matrix [*A*] is the extensional stiffness, [*B*] is the bending-extension coupling stiffness, and [*D*] is the bending stiffness. Note that the terms are plate stiffnesses, so that in order to obtain the flexural stiffness for a beam the stiffness terms must be multiplied by $(1 - \nu^2)$.

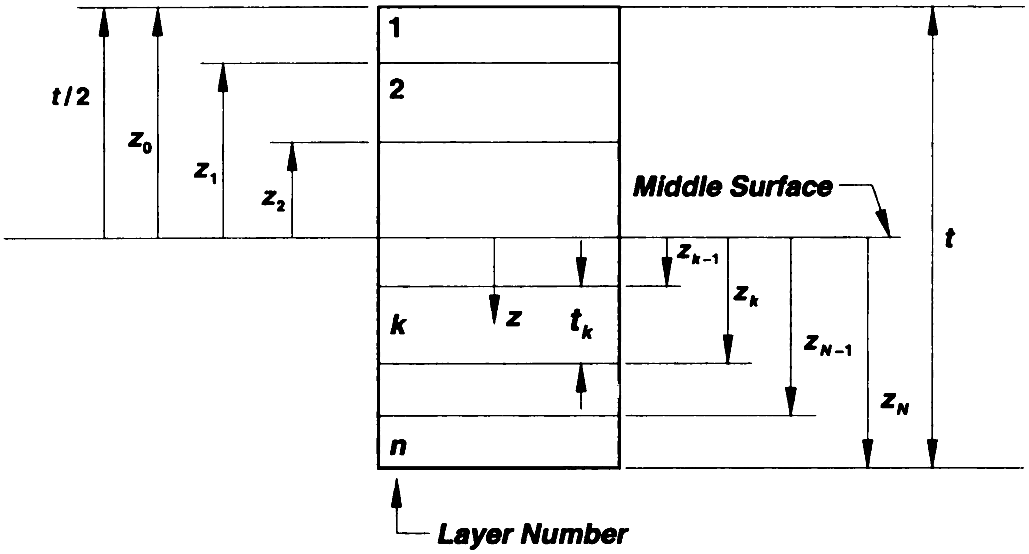

Figure 4.23. Section geometry of a general laminate

The section properties for hierarchical cellular structures can thus be obtained by considering the different scales of the material continuum, form the microstructural mechanics of the randomly oriented short fiber reinforced biocomposite to the cellular material arrangement, to the arrangement in the hierarchical structure. The analysis method was integrated into a custom program and can be used in optimization strategies to determine efficient hierarchical structures for improved efficiency of biocomposite cellular structures. However, this approach could not be verified with the experimental data from the cellar beams and plates (Chapter 3) because of limitations in the procedure, as discussed next.

4.5.2 Limitations

The proposed analysis procedure for hierarchical cellular structures is limited by assumptions made in the cellular material equations. The mechanics of cellular solids equations for the elastic constants of a cellular material are based on analyzing a unit cell and assuming average properties. This assumption is reasonable when there are many layers of cellular lamina in the hierarchical structure. However, when there is a small number of cellular lamina in the structure the averaged cellular material does not account for the actual distribution of material through the section. This issue leads to errors in the moment of inertia of the lamina, and hence the flexural stiffness of the hierarchical structure. This concept is illustrated in (Figure 4.24).

In Figure 4.24 the flexural stiffness of cellular structures with varying numbers of cellular lamina was calculated using the proposed analysis procedure (EI_{analysis}), and using the conventional mechanics of materials approach of Section 4.3 ($EI_{\text{mechanics}}$). The flexural stiffness using mechanics of materials divided by the flexural stiffness using the proposed analysis procedure is plotted against the number of layers of cellular lamina in the hierarchical structure (Figure 4.24). The results show that for hierarchical structures with four or more layers the proposed analysis procedure agrees with the results from mechanics of materials, but for less that four layers the proposed procedure is inaccurate. Thus, the proposed analysis procedure is limited to cases of hierarchical cellular structures with four or more layers. Because this was not the case in the cellular beams and plates tested in the structural experiment study (Chapter 3) the proposed analysis procedure could not be used. Nevertheless, the proposed analysis procedure is still a viable option for performing parametric, and optimization studies, where hierarchical cellular structures may be discretized with many different layers of cellular material.

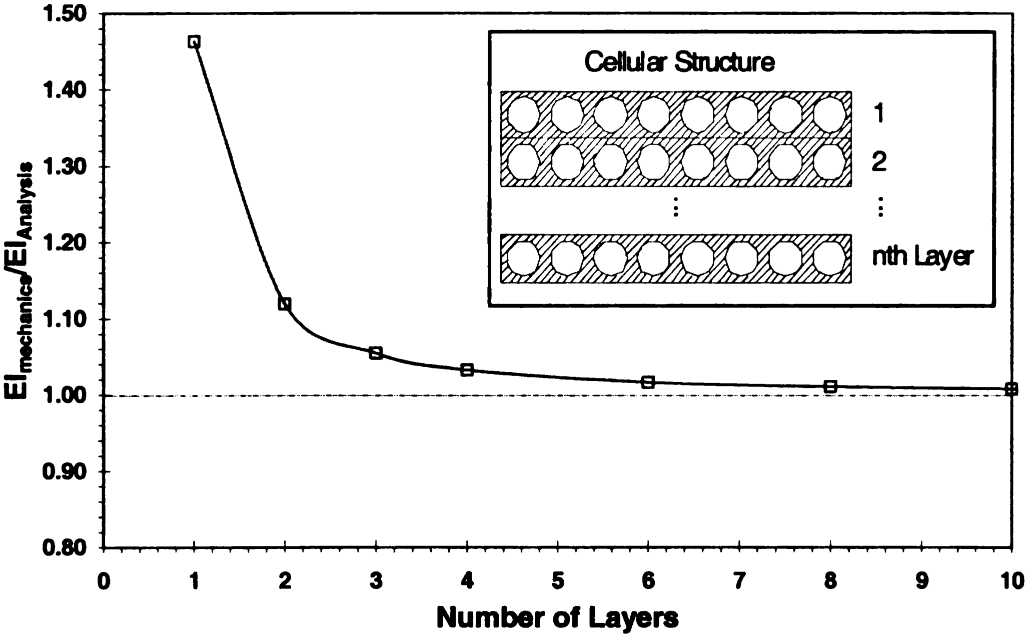

Figure 4.24. Accuracy of the proposed analysis procedure for varying number of cellular layers

4.6 Prestressed Hybrid Sandwich Structures

Thermal induced deformations can occur in composite materials where two or more materials are co-cured and then cooled down to service conditions. The different materials bond together at a high temperature. After curing, the composite is cooled to service temperatures. The temperature change induces residual deformations (strains) in the structure as a consequence of the different "effective" thermal coefficients of expansion between the materials constituting the composite. The difference in "effective" thermal coefficients of expansion can be due to material composition or the material relative orientation. These temperature induced deformations create stresses and strains in the section with no application of external load, thus creating a prestress state.

Temperature induced strains (and stresses) are typically a negative effect and their effect is minimized through design, i.e. careful arrangement of the material and its orientation. However, this effect can be beneficial if strategic material arrangement can lead to an advantageous prestressed state, i.e. opposite to the stress state induced by mechanical loads. Thus, when mechanical (external) loads are applied to the structure, the materials must release the temperature strains and then undergo deformation in the opposite stress-strain regime. This increases the strain range the material in the structure must deform through before failure, thus increasing the capacity of the structure.

The biocomposite hybrid cellular plates manufactured with carbon fiber face sheets are susceptible to temperature induced deformations due to the small coefficient of thermal expansion of the carbon fibers compared to the biocomposite material system and the integral bond between the two fiber-reinforced composites. In the following sections analytical models are provided, which can be used to calculate the temperature induced deformations, stresses, and strains. The prediction models are compared with the measured deflection in the hybrid cellular plate with a bottom carbon face sheet, and used to investigate the prestressing effects in the hybrid cellular plates with carbon face sheets tested in the structural experimental program (Chapter 3). The temperature prestress effects are then investigated analytically for a full-scale hybrid cellular plate to evaluate its potential benefit to structural performance.

4.6.1 Thermal Effects in Hybrid Cellular Plates

When laminates of two different materials with significantly different coefficients of thermal expansion experience a change in temperature the laminate will deflect and bend at a given radius of curvature as shown in Figure 4.25. This was the case for the biocompostie hybrid cellular plates that were manufactured with carbon fiber face sheets.

To illustrate this concept, consider two cases: (i) two unbonded materials and (ii) two bonded materials with different coefficients of thermal expansion as shown in Figure 4.25 (where $\alpha_2 > \alpha_1$). For the first case, at curing temperature T_o the two materials have the same length. When the two materials cool to room temperature T, both materials will shrink different amounts. For the second case, at curing temperature T_o the two materials have the same length. When the bonded materials are cooled to room temperature T the top material wants to shrink more than the bottom material. However, the two materials are bonded, thus introducing bending. The thermal deformations will cause compression in the bottom material that wants to expand, but is restrained by the bond with the top material. Conversely, the thermal deformations will cause tension in the top material that wants to shrink, but is restrained by the bond with the bottom material. Note that the temperature induced, or residual, stresses and strains exist in the section with no application of external load, thus creating a state of prestress.

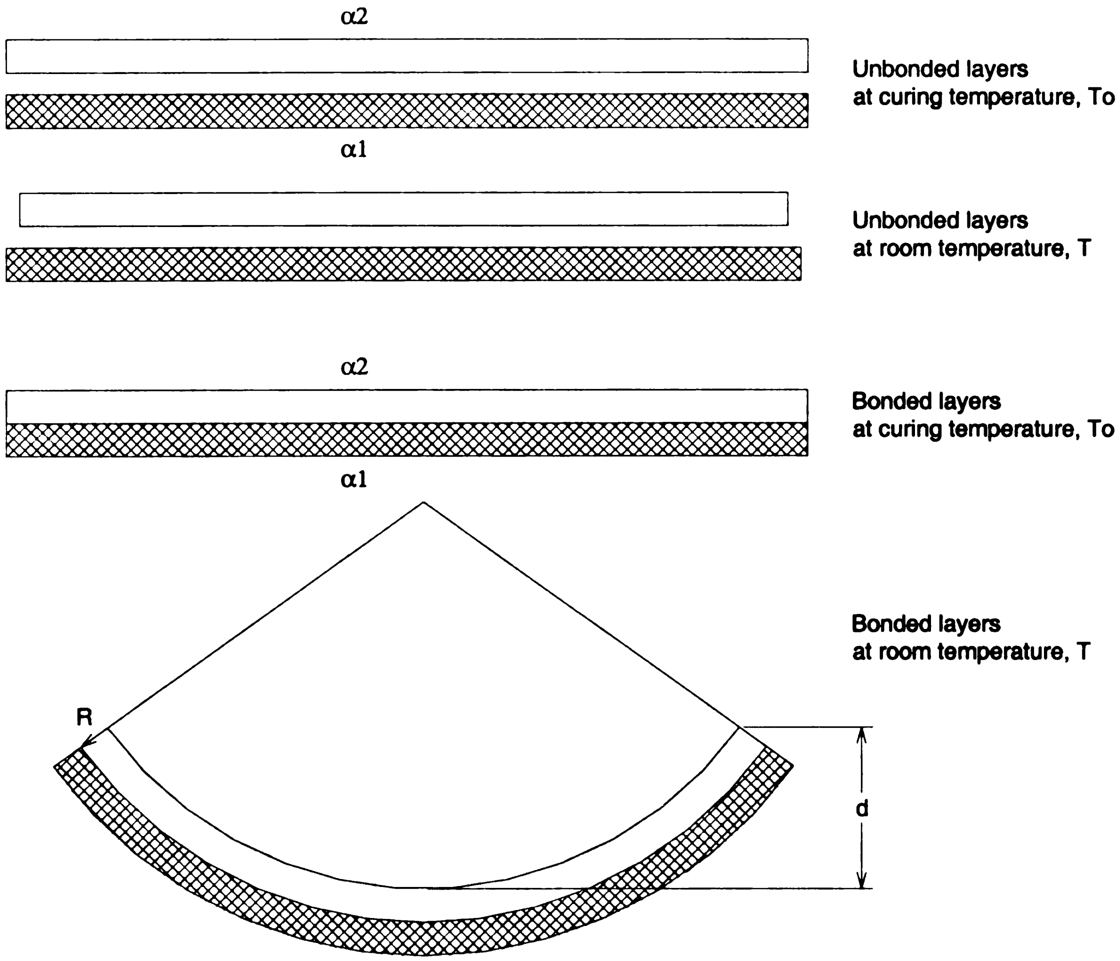

Figure 4.25. Temperature deformations in unbonded and bonded materials with $\alpha_2 > \alpha_1$

The case described above is similar to the case of the biocomposite hybrid cellular plates with carbon fiber face sheets. The carbon fiber face sheets have a much lower coefficient of thermal expansion than the biocomposite material system, which leads to temperature induced stresses and strains in the section. In the following section, analytical models that can be used to calculate the temperature deformations are presented.

4.6.1.1 Analytical Models for thermal effects in Hybrid Cellular Plates

Two analytical methods were used to calculate the curvature and the deflection of the biocomposite cellular plate with a bottom layer of carbon fiber fabric. The first method uses discrete equations (Ghali and Neville 1997, Barker and Puckett 1997) to calculate the axial strain and curvature in the plate due to temperature effects. The stresses in the plate are then calculated using the axial strain and curvature profile. The second method is based on a solution using the theory of elasticity as presented by Timoshenko (1925). The deflection of the plate was then calculated using the curvatures calculated using both methods and simple geometric relations.

The temperature induced deformations due to nonlinear temperature gradients can be determined by integrating the gradient effect over the cross-section of the member. This analysis approach is presented by Ghali and Neville (1997) and is commonly used for bridge design where nonlinear temperature gradients are encountered. However, if the temperature gradient is linear and the cross-section is made of distinct materials with different coefficients of thermal expansion, the integration can be modeled by piece-wise linear functions (Barker and Puckett 1997).

As shown by Ghali and Neville (1997), the axial strain due to a nonlinear temperature gradient is given by:

$$\varepsilon_o = \frac{\alpha}{A}\int Tb\,dy = \frac{\alpha}{A}\int T\,dA\,. \tag{4.6.1}$$

If the temperature gradient varies at most linearly through the section depth, then the cross-section can be discretized into layered segments and Equation (4.6.1) can be simplified to a discrete summation (Barker and Puckett 1997). Consider the segment shown in Figure 4.26 subjected to a linearly varying temperature gradient. Although the segment shown is rectangular, the segment shape may be arbitrary. The segment elastic centroidal axis is located at a distance $\bar{y}_i$ from the section neutral axis, and y is the location of the differential segment area dA. The area of the segment and its second moment of area are denoted by A_i and I_i, respectively. Also, note that $y_i = y - \bar{y}_i$. Thus, the temperature at location y is:

$$T = T(y) = T_{ai} + \frac{\Delta T_i}{d_i} y_i = T_{ai} + \frac{\Delta T_i}{d_i}(y - \bar{y}_i), \tag{4.6.2}$$

where T_{ai} is the temperature at the segment centroid, ΔT_i is the temperature difference from the bottom of the element to the top ($\Delta T_i = T^i_{bot} - T^i_{top}$), and d_i is the depth of the segment.

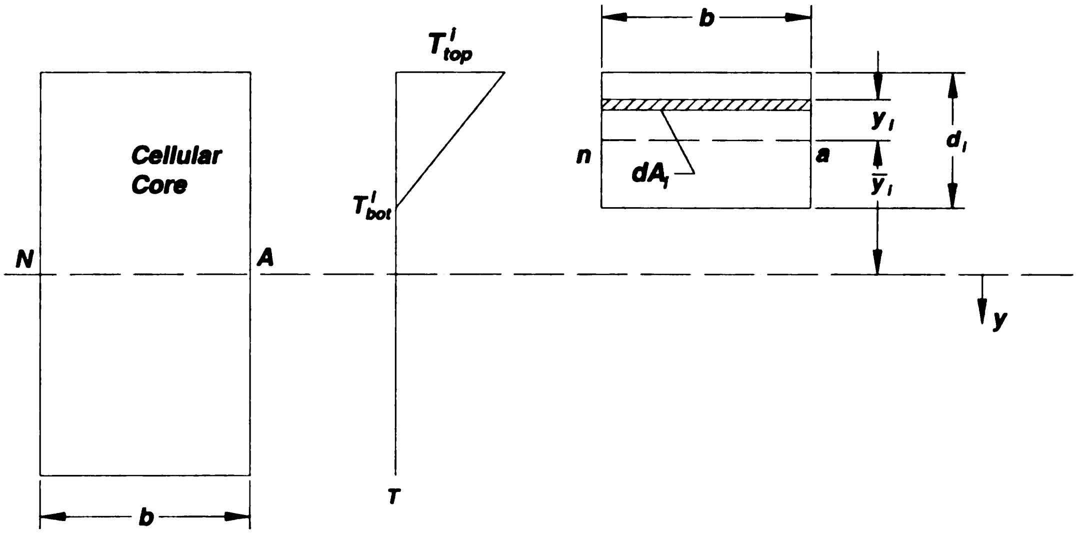

Figure 4.26. Example cross-section with discrete element

Substitution of Equation (4.6.2) into Equation (4.6.1) yields:

$$\varepsilon_o = \frac{\alpha}{A} \sum \int \left[T_{ai} + \frac{\Delta T_i}{d_i}(y - \bar{y}_i) \right] dA_i \, , \tag{4.6.3}$$

where the summation is over all the segments in the cross-section and the integration is over the domain of the discrete segment. Integration over each term in Equation (4.6.3) leads to:

$$\varepsilon_o = \frac{\alpha}{A}\sum\left[T_{ai}\int dA_i + \frac{\Delta T_i}{d_i}\int y dA_i - \frac{\Delta T_i}{d_i}\int dA_i\right]. \tag{4.6.4}$$

Recognizing that $A_i = \int dA_i$ and $\bar{y}_i A_i = \int y dA_i$, and substituting into Equation (4.6.4) results in:

$$\varepsilon_o = \frac{\alpha}{A}\sum\left[T_{ai}A_i + \frac{\Delta T_i}{d_i}\bar{y}_i A_i - \frac{\Delta T_i}{d_i}\bar{y}_i A_i\right]. \tag{4.6.5}$$

Noting that the second and third terms sum to zero, Equation (4.6.5) simplifies to

$$\varepsilon_o = \frac{\alpha}{A}\sum[T_{ai}A_i]. \tag{4.6.6}$$

Because the coefficient of thermal expansion may vary for the elements in the hybrid cellular plate, α is moved into the summation:

$$\varepsilon_o = \frac{1}{A}\sum\alpha_i[T_{ai}A_i], \tag{4.6.7}$$

which is the discrete form for Equation (4.6.1).

The temperature induced curvature is now considered. The curvature, ϕ, due to the temperature gradient is (Ghali and Neville 1997):

$$\phi = \frac{\alpha}{I}\int Tbydy = \frac{\alpha}{I}\int TydA, \tag{4.6.8}$$

where I is the second moment of area of the entire cross-section about the elastic centroidal axis. Substituting Equation (4.6.2) into Equation (4.6.8) yields:

$$\phi = \frac{\alpha}{I}\sum\left[T_{ai}\int y_i dA_i + \frac{\Delta T_i}{d_i}\int(y^2 - \bar{y}_i y)dA_i\right], \tag{4.6.9}$$

where again, the summation is over all the segments in the cross-section and the integration is over the domain of the discrete segment. Evaluating the integration in Equation (4.6.9) leads to:

$$\phi = \frac{\alpha}{I}\sum\left[T_{ai}\bar{y}_i A_i + \frac{\Delta T_i}{d_i}\int y^2 dA_i - \frac{\Delta T_i}{d_i}\bar{y}_i\int y dA_i\right] \tag{4.6.10}$$

$$\phi = \frac{\alpha}{I}\sum\left[T_{ai}\bar{y}_i A_i + \frac{\Delta T_i}{d_i}I_i - \frac{\Delta T_i}{d_i}\bar{y}_i^2 A_i\right]. \tag{4.6.11}$$

Recalling the parallel axis theorem to relate the cross-section properties in Equation (4.6.11):

$$I_i = \bar{I}_i + A_i\bar{y}_i^2, \tag{4.6.12}$$

and solving for $\bar{I}_i$ yields:

$$\bar{I}_i = I_i - A_i\bar{y}_i^2. \tag{4.6.13}$$

Using Equation (4.6.13) with Equation (4.6.11) results in:

$$\phi = \frac{\alpha}{I}\sum\left[T_{ai}\bar{y}_i A_i + \frac{\Delta T_i}{d_i}\bar{I}_i\right]. \tag{4.6.14}$$

Again, because the coefficient of thermal expansion may vary for the elements in the hybrid cellular plate, α is moved into the summation:

$$\phi = \frac{1}{I}\sum\alpha_i\left[T_{ai}\bar{y}_i A_i + \frac{\Delta T_i}{d_i}\bar{I}_i\right], \tag{4.6.15}$$

which is the discrete form of the integral given in Equation (4.6.8).

The analysis of the deflection of a bimetal strip was first developed by Timoshenko (1925), who presented a simple derivation using the theory of elasticity. This analysis was derived for bimetal strips, but is equally applicable to bimaterial strips.

The general equation for the curvature radius of a bimaterial strip under uniform temperature change from T_o to T in the absence of any external forces is given by:

$$\frac{1}{R} = \phi = \frac{6(1+m)^2(\alpha_2 - \alpha_1)(T - T_o)}{t[3(a+m)^2 + (1+mn)(m^2 + 1/mn)]}, \qquad (4.6.16)$$

where: α_1 = coefficient of thermal expansion of the low expansive material

α_2 = coefficient of thermal expansion of the high expansive material

n = E_1/E_2 , with E_1 and E_2 the elastic moduli of each material

m = t_1/t_2, with t_1 and t_2 are the thickness of each layer

t = $t_1 + t_2$ the thickness of the strip,

and the width of the strip is taken as unity.

Once the curvature of the plate is calculated, using either of the above methods, the deflection at the center of the beam can be calculated using geometric relations. Using Pythagoras' Theorem the following relation can be made from a right triangle between the end of the plate, the middle of the undeformed plate, and the center of the curvature of the plate:

$$(R - t_1)^2 = (R - d - t_1)^2 + (L/2)^2. \qquad (4.6.17)$$

Expanding Equation (4.6.17) and solving for the curvature of the plate we get:

$$\frac{1}{R} = \frac{8d}{L^2 + 4d^2 + 8dt_1}. \qquad (4.6.18)$$

Making the assumption that the deflection, d, and the thickness, t, are less than 10% of the length of the plate the terms $8dt_1$ and $4d^2$ may be neglected and the expression reduces to:

$$d = \frac{L^2}{8R}. \qquad (4.6.19)$$

The axial shrinkage is also assumed to be small and thus neglected in the calculation of the deflection of the center of the beam.

4.6.1.2 Results

The hybrid cellular plate with green hemp/polyester and a bottom layer of carbon fabric was analyzed using both analytical models detailed in the previous section. The elastic modulus of the unidirectional carbon layer was taken to be 77.3 GPa, assuming a fiber volume fraction of 30%, and the coefficient of thermal expansion was taken as 7.24 $\times 10^{-6}/^{o}C$. For the green hemp biocomposite material system, the elastic modulus was taken as 5.0 GPa, and the coefficient of thermal expansion was taken as $50\times 10^{-6}\ /^{o}C$. The assumed values are in agreement with the values measured in the material experimental program (Chapter 2). The change in temperature was taken as –120°C, which is the change in temperature from final curing conditions (150°C) to room temperature (30°C). The mid-span deflection of the plate was measured using calipers accurate to 0.01 mm. Because the deflection was relatively small compared to the width of the plate (101.6 mm) it was not possible to measure the deflection at the center of the plate. Thus, the deflection was measured at the edges of the plate and averaged. The measured deflection at the mid-span of the plate was 4.46 mm.

The discrete equations (Equations 4.6.7, 4.6.15, and 4.6.19) were used to calculate the axial strain, curvature, and mid-span deflection, *d*, of the hybrid cellular plate as shown in Table 4.11. The mid-span deflection of the plate was calculated as 3.50 mm, which is within 22% of the measured deflection (Table 4.11). The assumed properties of the biocomposite section and the carbon layer may have lead to errors in the calculated deflection. The measurement method used to determine the mid-span deflection of the plate may have also lead to errors in the measured deflection.

Table 4.11. Temperature deflection calculations of the biocomposite cellular plate with bottom carbon layer (CP1-C) using discrete equations

PROPERTY	SECTION 1 Bio	SECTION 2 Carbon*	TOTAL*
E_i (GPa)	5.0	77.3	--
E_i (ksi)	725	11209	--
α_i (1/°C)	5.00E-05	7.24E-06	--
d_i (mm)	15.84	0.42	16.26
A_i (mm^2)	1039	6583	7621.9
$I_{bar\ i}$ (mm^4)	2.86E+04	9.61E+00	1.04E+05
$y_{bar\ i}$ (mm)	-8.39	0.54	15.5
Ta_i (°C)	-120	-120	--
ΔT_i (°C)	0	0	--

*Carbon transformed to properties of the biocomposite

$L =$ 304.8 mm

$\varepsilon_o =$ -1.57E-03 mm/mm

$\phi_o =$ 3.10E-04 1/mm

$d =$ 3.50 mm

$d_{measured} =$ 4.46 mm

Based on the hypothetical free strains in the section if the layers were unbonded, and the calculated temperature-induced axial strain and bending curvature of the bonded section, the strain and stress distributions in the section were calculated (Figure 4.27). The resulting stress distribution shows the top layer of the biocomposite material is in tension due to temperature effects, while the carbon layer is in compression.

The stresses due to thermal effects (Figure 4.27) create a state of prestress in the section that is opposite to the stress state in positive bending to be imposed by the mechanical loads (3-point bending, see Section 3.3.4). In other words, the bottom of the beam, which is to be subjected to tensile stress due to bending, is initially in a compressed state, while the top of the beam, which is to be subjected to compressive stresses due to bending, is initially in a state of tension. Thus, the bending stresses must overcome the prestressed state in the section prior to creating tensile stresses at the bottom of the section, or compressive stresses at the top of the section.

The strain in the bottom carbon layer due to thermal effects is 0.47e-3 mm/mm in compression (Figure 4.27), which, based on the measured ultimate tensile strain of 1.67e-2 mm/mm for the carbon material (see section 2.4.4.4, page 51), is 0.7% of the failure strain. In order to fail, the carbon layer must deform through the compressive strain of 0.47e-3 mm/mm to reach zero strain in the layer, and then deform to its ultimate tensile strain of 1.67e-2 mm/mm. Thus, the range of tensile strain the carbon layer must go through before failure is increased by 0.47e-3 mm/mm, or 0.7%.

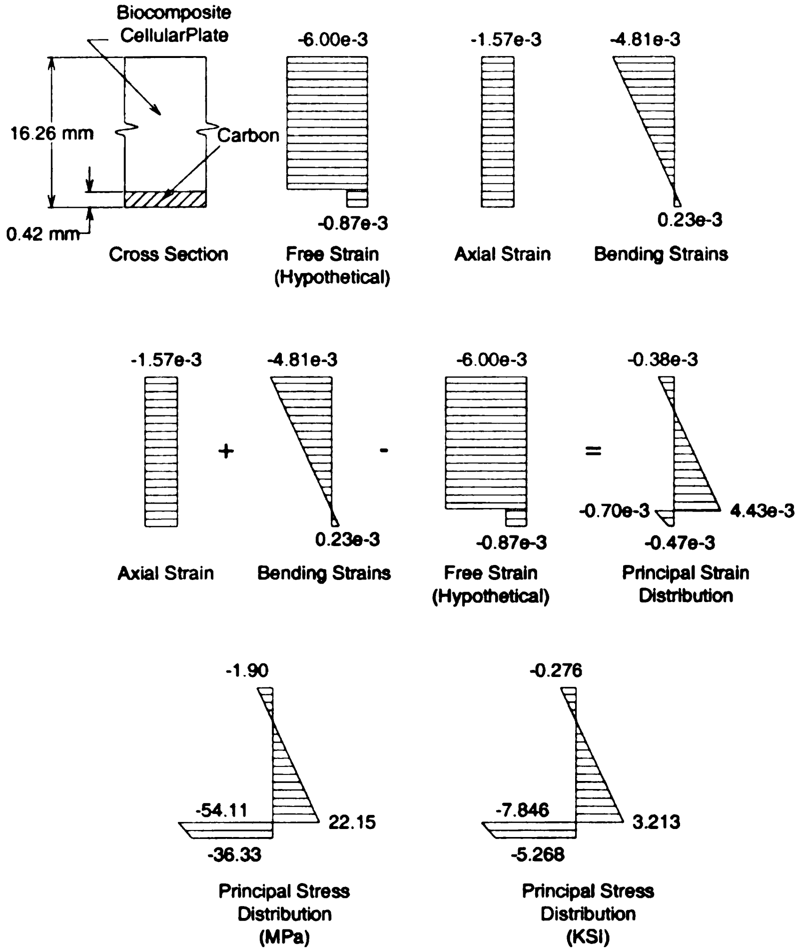

Figure 4.27. Calculated stress and strain distributions due to thermal effects in the biocomposite cellular plate with bottom carbon layer (CP1-C)

The elasticity solution by Timoshenko (1925) was used to calculate the curvature, and mid-span deflection, *d*, of the cellular plate as show in Table 4.12. The calculated deflection of 3.51 mm is within 21% of the measured deflection of 4.46 mm (Table 4.12). Again, the assumed properties of the biocomposite section and the carbon layer may have lead to errors in the calculated deflection.

Table 4.12. Temperature deflection calculations of the biocomposite cellular plate with bottom carbon layer (CP1-C) using the elasticity solution

PROPERTY		PROPERTY	
α_1 (1/°C)	7.24E-06	t_1 (mm)	0.42
α_2 (1/°C)	5.00E-05	t_2 (mm)	15.84
E_1 (GPa)	77.3	t (mm)	16.26
E_1 (ksi)	11209	n	15.46
E_2 (GPa)	5.0	m	0.0265
E_2 (ksi)	725		

$L =$ 304.8 mm

$\phi_o =$ 3.02E-04 1/mm

$d =$ 3.51 mm

$d_{measured} =$ 4.46 mm

Both analytical models used to calculate the temperature deformations in the hybrid biocomposite cellular plate gave similar results and agreed well with the measured deflection of the beam. The curvatures calculated using both methods also agree well with each other (see Table 4.11 and Table 4.12). The results of the analytical analyses may be improved with more accurate values for the elastic modulus and coefficients of thermal expansion for the biocomposite and carbon fiber materials.

Based on the agreement of results for both methods for calculating deflections due to thermal effects, the discrete equations were used to analyze the hybrid cellular plate with raw hemp/polyester and top and bottom carbon layers. The measured dimensions of the hybrid cellular plate were used, and the properties for the biocomposite material system and carbon layers in the previous analyses were taken equal to the previous analysis.

The properties used for the analysis are shown in Table 4.13, and the resulting stress and strain distributions are shown in Figure 4.28. Notice that because the section is symmetric there are no bending deformations in the section (Figure 4.28). However, the top layer (carbon layer) is subjected to compression, which is undesirable for a section that is to be subjected to positive bending.

Table 4.13. Temperature deflection calculations of the biocomposite cellular plate with top and bottom carbon layers (CP2-C) using the discrete equations

PROPERTY	SECTION 1 Carbon*	SECTION 2 Bio	SECTION 3 Carbon*	TOTAL*
E_i (GPa)	77.3	5.0	77.3	--
E_i (ksi)	11209	725	11209	--
α_i (1/°C)	7.20E-06	2.50E-05	7.20E-06	--
d_i (mm)	0.42	17.46	0.42	18.30
A_i (mm^2)	658.3	1039.0	658.3	1697.3
$I_{bar\,i}$ (mm^4)	9.61E+00	4.12E+04	9.61E+00	9.39E+04
$y_{bar\,i}$ (mm)	-8.94	0.00	8.94	15.50
Ta_i (°C)	-120	-120	-120	--
ΔT_i (°C)	0	0	0	--

*Carbon transformed to properties of the biocomposite

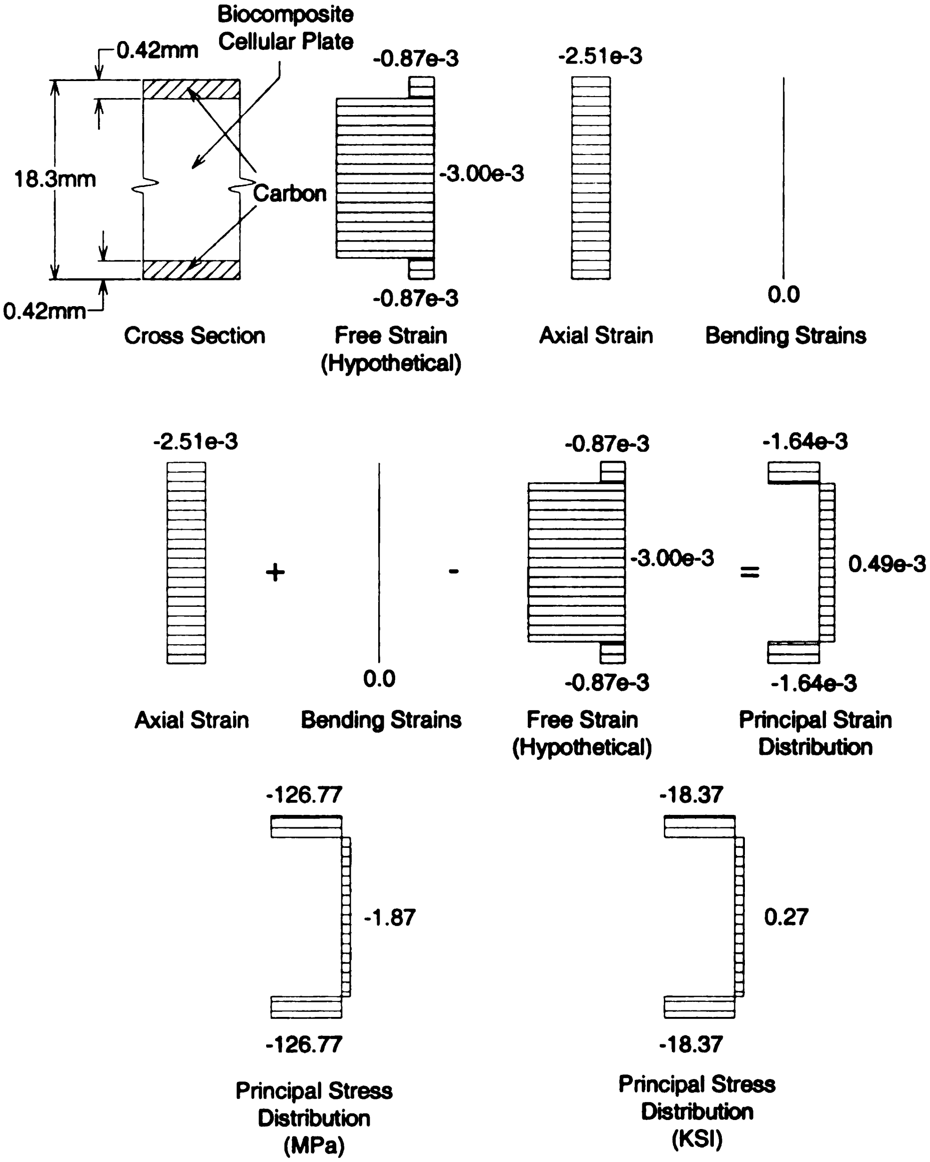

Figure 4.28. Calculated stress and strain distributions due to thermal effects in the biocomposite cellular plate with top and bottom carbon layers (CP2-C)

4.6.2 Temperature Prestress Effects

The temperature prestress effects on the two hybrid cellular plates with carbon fiber face sheets tested in the structural experimental program (Chapter 3) are illustrated in Figure 4.29 and Figure 4.30. The load-displacement response of the two cellular plates was used to calculate the force-strain response in the bottom carbon face sheet. The force-strain response was then corrected to account for the thermal strains in the section, which created a state of prestress prior to testing. For both hybrid plates, the thermal strains in the bottom face sheet were compressive, which is opposite to the tensile strains from the applied loading in the flexural test. Thus, the thermal strains were subtracted from the measured strains. The resulting force-strain response for the hybrid plate with bottom carbon only is shown in Figure 4.29, while the response for the hybrid plate with top and bottom carbon is shown in Figure 4.30. The discontinuity in the hybrid plate with top and bottom carbon (Figure 4.30) is due to the change in the section properties (namely the moment of inertia) that occurs when the top face sheet buckled (Section 3.5.1). The section properties change because the buckling of the top carbon layer causes the neutral axis to shift towards the bottom carbon layer.

The corrected force-strain results provided in Figure 4.29 and Figure 4.30 show the corrected failure strains in the carbon face sheets are in agreement with the failure stains measured in the material experimental program (see Table 2.9). Notice that for both hybrid plates the measured failure strain in the carbon face sheet is larger than the actual failure strain of the material. This apparent increase in the failure strain is due to the temperature prestressing effect, which allows the material to go through a larger range of strain before failure. This increase in capacity due to temperature prestress can thus be taken advantage in the design of hybrid structures.

The beneficial effects of prestressing were small for the tested laboratory-scale hybrid cellular beams and plates. This is due to the small dimensions of the cross-section. The effects on full-scale components were found to be more attractive as described in the next section.

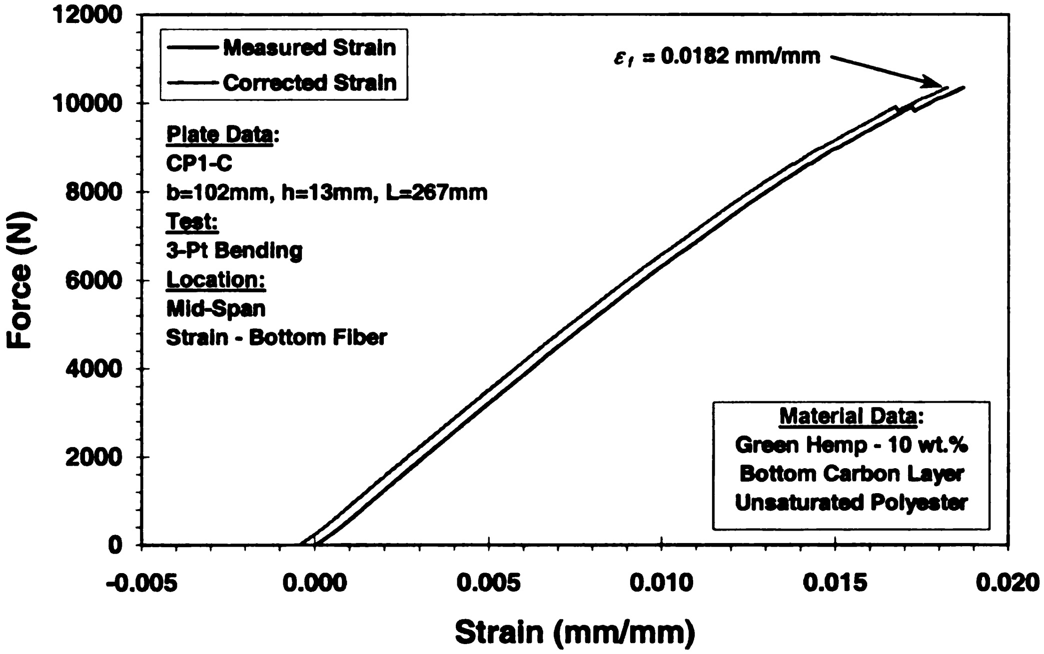

Figure 4.29 Force-strain response of the biocomposite hybrid cellular plate with a bottom carbon face sheet, with correction for temperature prestress effects

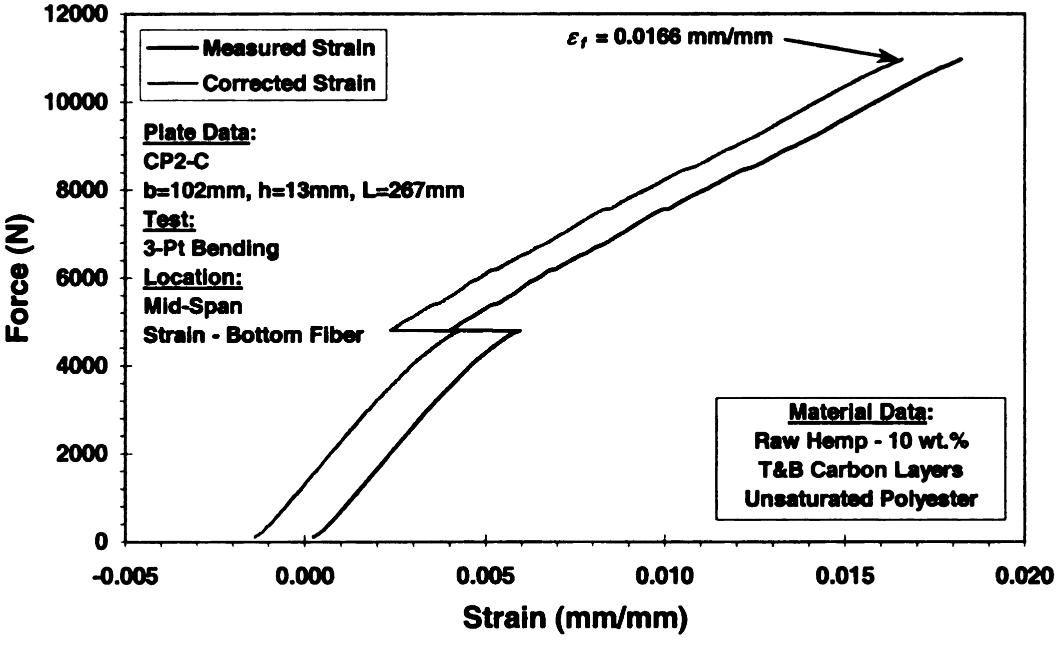

Figure 4.30. Force-strain response of the biocomposite hybrid cellular plate with top and bottom carbon face sheets, with correction for temperature prestress effects

4.6.3 Prestressing Effects in Full-Scale Panels

The temperature prestressing effects on a full-scale cellular plate with integrated carbon fiber fabric were determined and compared with the effects on the small laboratory-scale cellular plate. The full-size cellular plate was taken as a 152.4 mm deep by 1219.2 mm wide cellular plate with two layers of carbon fabric on the bottom, which have a total thickness of 0.84 mm. The relative density of the full-scale plate was taken to be the same as the laboratory-scale plate, $\rho^*/\rho_s = 0.588$. The same material properties were used for both plates. Calculations and results for the full-scale cellular plate are shown in Figure 4.31.

The results show that the curvature for the full-scale hybrid cellular plate, 7.9e-8 1/mm (Figure 4.31), is very small compared to the curvature in the laboratory-scale plate, 3.1e-4 1/mm (Figure 4.27). Thus, thermal effects in the full-scale cellular plate may not cause the large curvatures and deflections seen in the laboratory-scale plates. Despite the small curvature in the full-scale hybrid cellular plate, the axial strain, 5.08e-3 mm/mm (Figure 4.31), is large compared to the lab scale plate, 1.57e-3 mm/mm (Figure 4.27). Because of the large axial strain in the full-scale plate, the stresses are much higher. In the full-scale plate the residual strain in the carbon layer is 41% of its failure strain, while in the laboratory-scale plate the strain in the carbon layer was only 0.7% of its failure strain. Thus, the prestressing thermal effects in the full-scale plate considerably increase the range of strain the carbon layer must go through before failure, and consequently increase the capacity of the section.

PROPERTY	SECTION 1 Bio	SECTION 2 Carbon*	TOTAL*
E_i (GPa)	5.0	77.3	--
E_i (ksi)	725	11209	--
α_i (1/°C)	5.00E-05	7.24E-06	--
d_i (mm)	151.61	0.84	152.45
A_i (mm^2)	71977.3	15799.3	87776.1
$I_{bar\,i}$ (mm^4)	2.62E+08	9.24E+02	3.45E+08
$y_{bar\,i}$ (mm)	-17.19	62.50	89.53
Ta_i (°C)	-120	-120	--
ΔT_i (°C)	0	0	--

*Carbon transformed to properties of the biocomposite

$L =$ 1219.2 mm

$\varepsilon_o =$ -0.00508 mm/mm

$\phi_o =$ 7.87E-08 1/mm

$d =$ 0.01778 mm

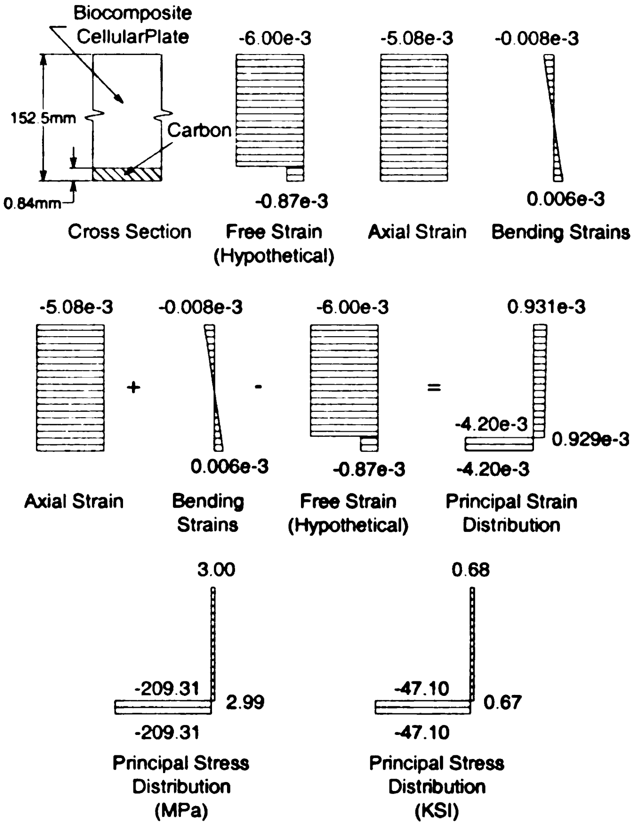

Figure 4.31. Strain and stress calculations and distributions due to temperature effects in a full-scale biocomposite cellular plate

4.7 Performance and Feasibility Studies

The results from the flexural tests of the biocomposite cellular beams (Chapter 3) were compared with beams of equal size made of conventional construction materials (Figure 4.32). The conventional materials used for the comparison were wood (Douglas Fur), and reinforced concrete. The reinforced concrete beam (3% steel reinforcement ratio) was analyzed both cracked and uncracked. However, reinforced concrete beams typically crack under service loads, reducing the stiffness of the component.

The results in Figure 4.32 show that the bio-beams compared very favorably with the beams from conventional construction materials. The specific stiffness of the hierarchical bio-beam outperforms both the cracked and uncracked concrete beams. Their performance, however, falls short from that of the wood beam. The specific stiffness of the wood beam is very large because of the low density, and the moderate elastic modulus of Douglas Fur. The cellular bio-beam with a periodic cell arrangement shows a lower specific stiffness than the hierarchical bio-beam but still outperforms the cracked concrete member.

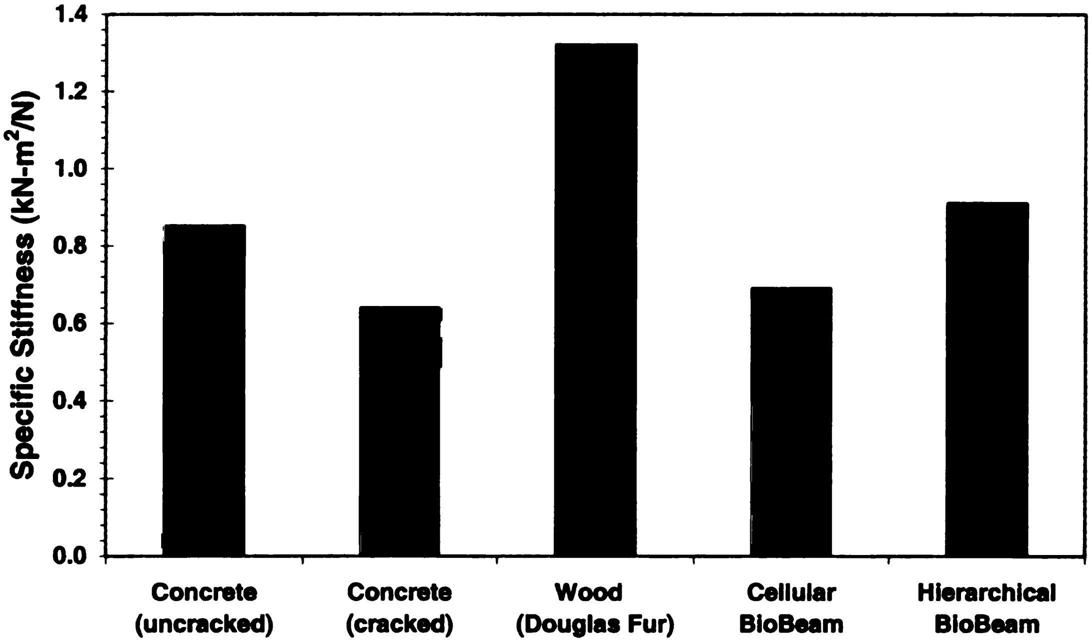

Figure 4.32. Performance biocomposite cellular beams with beams of conventional construction materials

The results from the experimental studies on the biocomposite cellular plates were extrapolated to evaluate the performance of full-scale structural components and compare them with conventional flooring systems used in the construction industry. The allowable pressure versus the simply supported span length for panel systems is shown in Figure 4.33. The allowable pressure is the loading the component can withstand while maintaining an industry-standard allowable deflection (*L*/180). For this application, the deflection is the critical design criteria and the strength requirements are met for all span lengths shown.

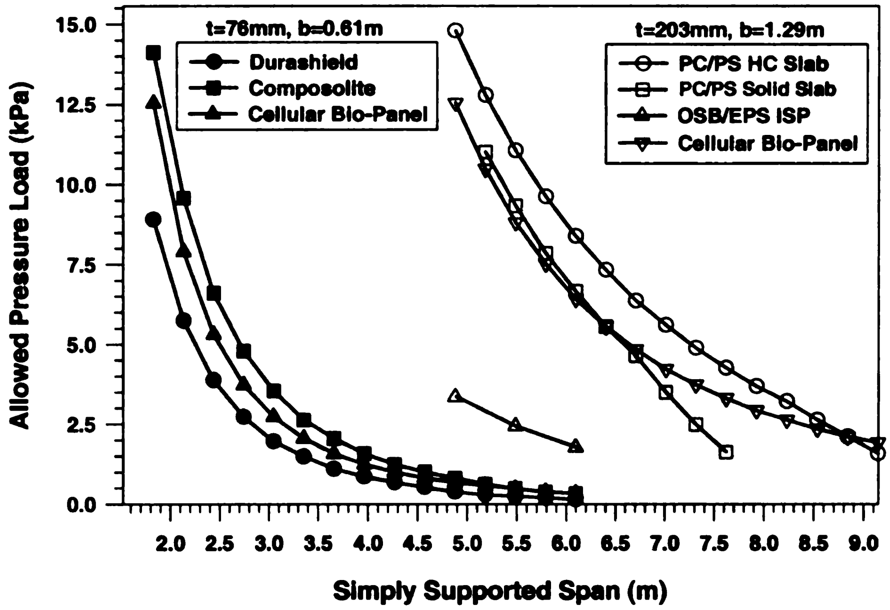

Figure 4.33. Performance of full scale biocomposite cellular panels versus conventional flooring systems

Figure 4.33 compares panels grouped into two categories. The first set of curves is for a panel size of 76 mm by 0.61 m, which is a size typically used in commercial building construction. For this group, the Bio-Panel is compared with commercially available fiberglass sandwich panel systems (Durashield and Composolite [Strongwell 2003], Table 4.14). The second set of curves is for a panel size of 203 mm by 1.29 m, which is a size typically used for conventional materials in commercial construction. For this group, the bio-panel is compared with a precast prestressed hollow core concrete slab (PC/PS HC slab, Table 4.15), a precast prestressed solid concrete slab (PC/PS solid slab, Table 4.15), and an oriented wood strand board ISP (insulated structural panel [Insulspan 2003], Table 4.16). The PC/PS HC slab, and PC/PS solid slab are standard building components found in the PCI Design Handbook (1999). A green hemp/polyester cellular biocomposite plate (cellular bio-panel) with a fiber volume fraction of 30% and a relative density of 0.56 was used for the comparison in both panel size groups.

Table 4.14. Pultruded fiberglass panel data

Panel	*Resin Type*	*Depth (mm)*	*Width (mm)*	*Flexural Strength (MPa)*	*Flexural Modulus (GPa)*
Composolite	Vinyl Ester	76	0.61	168.9	6.10
Durashield	Vinyl Ester	76	0.61	103.4	2.17

Table 4.15. Precast prestressed concrete panel data

Panel	*Depth (mm)*	*Width (mm)*	*Compressive Strength (MPa)*	*Number of Strands*	*Strand Size (mm)*
Precast Prestress Hollow Core Slab	203	1.29	34.5	6	9.5
Precast Prestressed Solid Slab	203	1.29	34.5	6	9.5

Table 4.16. Oriented strand board/expanded polystyrene core – insulated structural panel data

Panel	*Depth (mm)*	*Width (mm)*	*OSB Thickness (mm)*	*OSB Stiffness (GPa)*	*EPS Core Depth (mm)*
OSB/Expanded Polystyrene core - Insulated Structural Panel	203	1.29	11.1	6.5	180.8

The results in Figure 4.33 show that the cellular bio-panels compete well with all of the conventional panels for both categories, and can even outperform some conventional flooring systems. In the first category, the bio-panel competes well with the Composolite panel and outperforms the Durashield panel. For example, for a span of 2.0 m the Composolite panel has an allowable pressure of 14 kPa and the Durashield panel has an allowable pressure of 9 kPa, while the bio-panel has an allowable pressure of 12.5

kPa. In the second category, the bio-panel substantially outperforms the OSP/EPS ISP panel for all span lengths, and outperforms the PC/PS solid slab for spans above 6.75 m. The bio-panel compares well with the PC/PS HC slab for large spans (>8 m), but for shorter spans the PC/PS HC slab outperforms the bio-panel. It should be noted that the above comparison is for an all-biocomposite panel system, thus the performance of hybrid and hierarchical panels is expected to be even better.

The results from the experimental studies on biocomposite cellular plates and the analysis procedures presented in Section 4.3 were used to extrapolate the performance of full-scale structural components for different applications. The full-scale performance was used to select dimensions of biocomposite cellular panels for the following applications: (i) highway bridge decks, (ii) commercial building floor panels, and (iii) residential flooring systems. A three-lane bridge with a girder spacing of 2.13 m (7-ft) was used for the highway bridge application. The American Association of State Highway and Transportation Official-Load and Resistance Factor Design (AASHTO-LRFD 1998) specifications were used for the bridge loading and allowable deflection criteria. A one-way slab with a span of 6.10 m (20-ft) was used for the commercial flooring system. The International Building Code (IBC 2000) specifications were used for the slab loading and the allowable deflection criteria. For the residential flooring system, a one-way floor system was used with a span of 0.61 m (2-ft) was considered. The IBC (2000) specification was again used for the loading and allowable deflection criteria.

For the cellular panels, a green hemp/polyester with a fiber volume fraction of 30% and a relative density of 0.56 was taken as the material system. A hybrid system with top and bottom layers of carbon was also considered for the bridge and commercial flooring applications. For the face sheets, a carbon/polyester material system with a fiber volume fraction of 50% was used as the material system.

The dimensions of the biocomposite cellular panel are shown in Figure 4.34, where the top and bottom flanges are solid material, and the core is assumed to have a periodic cellular architecture. The selection of dimensions was based on the allowable deflection limits for each application. Strength requirements were also considered and found to be much larger that the demand, however no resistance factors exist for design biocomposite materials. Thus, strength requirements for the bio-panels could not be properly evaluated. For the analysis and dimensioning of the bio-panels a unit strip method was used.

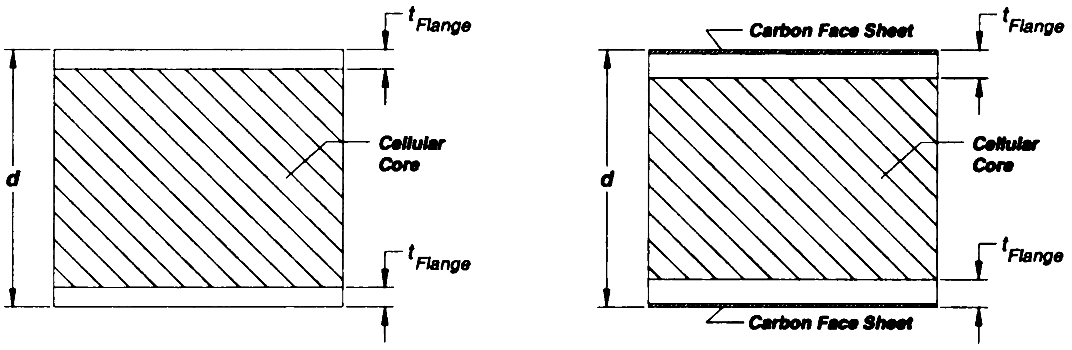

(a) Bio-panel

(b) Hybrid bio-panel

Figure 4.34. Schematic of the dimensions selected for the bio-panel structural components

The dimensions of the bio-panels for structural applications are provided in Table 4.17 (SI units) and Table 4.18 (US units). For the highway bridge deck, the depth of the bio-panel may be too thick for practical applications. However, the depth of the hybrid bio-panel is more reasonable, and falls within the thickness of typical highway bridge decks, which range from 180-230 mm (7-9 inches). In addition to providing increased stiffness and strength to the hybrid bio-panel, the carbon face sheets also act as a barrier to the biocomposite material providing protection from weather effects. For pedestrian bridge applications, where the loads are not as high, the use of an all bio-panel may be a viable solution. However, for highway bridge applications, hybrid bio-panels, or the use of all-bio-panels on bridge systems with closer girder spacings is better suited.

For commercial building slabs, the depth of both the bio-panels and the hybrid bio-panels are slightly larger than conventional reinforced concrete slabs, which have a typical depth of 152 mm (6 inches). This suggests that hybrid bio-panel may be needed for building slab applications. However, if the height between floors is not a major issue in the building construction, as is the case in low rise building construction, it may be possible to use all bio-panels for flooring systems.

For residential flooring systems the dimensions of bio-panels are practical and compare well with the dimensions of commercial panels (Figure 4.33). Clearly, from a structural standpoint, a hybrid bio-panel is not need for residential applications.

Table 4.17. Dimensions of bio-panels for structural applications (SI units)

System	*Section dimensions: Bio-Panel*			*Section Dimensions: Hybrid Bio-Panel*		
HIGHWAY BRIDGE DECK:						
	d =	305	mm	d =	229	mm
	t_{flange} =	13	mm	t_{flange} =	25	mm
COMMERICAL BUILDING SLAB:						
	d =	229	mm	d =	178	mm
	t_{flange} =	13	mm	t_{flange} =	13	mm
RESIDENTAL FLOOR:						
	d =	51	mm	d =	Not	mm
	t_{flange} =	6	mm	t_{flange} =	Needed	mm

Table 4.18. Dimensions of bio-panels for structural applications (US units)

System	*Section dimensions: Bio-Panel*			*Section Dimensions: Hybrid Bio-Panel*		
HIGHWAY BRIDGE DECK:						
	d =	12	in	d =	9	in
	t_{flange} =	0.5	in	t_{flange} =	1.0	in
COMMERICAL BUILDING SLAB:						
	d =	9	in	d =	7	in
	t_{flange} =	0.5	in	t_{flange} =	0.5	in
RESIDENTAL FLOOR:						
	d =	2	in	d =	Not	in
	t_{flange} =	0.25	in	t_{flange} =	Needed	in

CHAPTER 5 RESULTS, FEASIBILITY AND RECOMMENDATIONS

5.1 Overview

The findings from the material and structural experimental programs, and the analytical studies are summarized and used to assess the feasibility of using biocomposites for load-bearing structural components. In addition to the findings in this study, issues of processing and implementation in design procedures are also discussed in assessing the feasibility of load-bearing biocomposite components. Based on the feasibility assessment and the findings in this study, future work is recommended for the use and development of biocomposite material systems and structural forms.

5.2 Experimental Studies Summary

The results from the material and structural experimental studies are summarized in the following sections. The material experimental study included testing of all-biocomposite material systems and hybrid material systems with natural fiber core and fiber mat face sheets for tensile properties, impact strength, coefficient of thermal expansion and moisture absorption. The structural experimental study included testing of laboratory-scale biocomposite cellular beams and plates with varying cellular topologies and hybrid material systems. Focus is given to results that give insight to the use of biocomposite materials for load-bearing structural components.

5.2.1 Material Systems

The material experimental studies verified that the tensile properties of biocomposite materials could compete with E-glass fiber reinforced composites. In addition, the use of hybrid material systems with synthetic or aligned natural fiber face sheets and a chopped natural fiber core dramatically improved the mechanical properties over the all-natural fiber and all-E-glass composites. The hybrid material systems with E-glass face sheets also improved the moisture absorption response, which was comparable to the all-E-glass material system tested.

The experimental studies also showed that biocomposite material systems have a much higher coefficient of thermal expansion than conventional structural materials (approximately 3 times). This difference in thermal expansion must be considered if biocomposites are to be used with conventional structural materials. The moisture absorption of the tested biocomposites was also much higher than of the tested E-glass composite (approximately 4 times). The absorption of moisture into the biocomposite material may lead to swelling and durability issues. These properties were not studied in this research but are important characteristics for structural applications.

The material experimental studies also found the biocomposite material systems to be very brittle. This is due to the short natural fibers and the brittleness of the polyester resin used. The brittle behavior of the biocomposite material systems is undesirable for structural applications. Thus, improvements on the ductility of biocomposites should be investigated.

5.2.2 Structural Forms

The results from the structural experimental study verfied that the use of hierarchical cellular structures can improve the performance of biocomposite beams and plates. This suggests that hierarchical cellular structures should be studied further to develop efficient structural forms for biocomposite materials. The structural experimental study also shows that using jute, glass strand mat, and carbon face sheets can improve the stiffness and strength of biocomposite structures. These improvements can widen the range of structural applications in which biocomposite cellular structures can be used.

5.3 Analytical Studies Summary

The findings from the analytical studies are summarized for material systems and structural forms in the following sections. The analytical studies on material systems included performing a survey of available models to predict the stiffness and strength of biocomposite material systems and evaluating their performance with measured results. The studies on structural forms included the use of models to analyze the cellular beams and plates of the structural experimental study. Performance factors that measure the efficiency of structures in bending for minimum weight were also considered to study the effect of cellular microstructure on the performance of structural components.

5.3.1 Material Systems

The stiffness constants of biocomposite material systems can be predicted using the Halpin-Pagano laminate method, which approximates a randomly oriented fiber composite material as a quasi-isotropic laminate. The unidirectional properties of the composite material should be modeled using micromechanics models such as the Halpin-Tsai equations, which account for the reinforcement fiber aspect ratio. Prediction of the elastic modulus using this combination of models agreed well with the material experimental results.

The strength of biocomposite material systems can be predicted using the geometric averaging method, where the properties of a randomly oriented fiber composite are modeled by averaging the strength of an off-axis lamina over all fiber orientations. The unidirectional strength of the composite material can be modeled using Piggott's model, which accounts for the fiber aspect ratio. Strength predictions using these models overestimated the strength of the biocomposite material systems. The overestimation may be due to the assumed value used for the interfacial shear strength of the fiber and matrix. The interfacial shear strength should be measured for improved performance of the prediction models.

5.3.2 Structural Forms

Cellular, hierarchical, and hybrid cellular structures can be modeled using the material prediction models previously described in combination with fundamental mechanics concepts. The flexural stiffness and strength predicted using these tools agreed well with the experimental results.

A more robust analysis procedure was proposed for analyzing hierarchical and hybrid cellular structures by discretizing the structure into cellular lamina and using lamination theory to analyze the discretized structure. This analysis procedure can be used to analyze hierarchical cellular structures, hybrid structures, and thermal effects. However, the proposed procedure could not be verified with the experimental studies since the modeling is limited to hierarchical cellular structures with four or more layers of distinct cellular material.

Thermal effects in structures with hybrid material systems can create a prestressed state in the section. When a hybrid structural member is properly designed, thermal-induced strains can increase the section capacity. For example, it was found that using only a bottom layer of carbon resulted in pre-compression of the bottom layer of the hybrid cellular plate and pre-tension in the top layer, while using top and bottom carbon layers resulted in pre-compression of both the top and bottom layer of the hybrid cellular plate. Pre-compression of the top layer is, however, undesirable for positive bending.

5.4 Feasibility Assessment

The results from the reported studies have shown that hybrid cellular bio composite beams and plates not only have the potential to serve as primary load bearing structural components, but that they can compete with conventional structural materials. In civil construction, biocomposite structural components can be used as flooring systems and pre-fabricated components in residential and commercial construction, deck systems in highway bridges, and complete superstructures of small pedestrian bridges.

A main obstacle facing the use of biocomposite materials (and advanced composite materials in general) in civil structures is the lack of design procedures. One way in which designers account for the variability and uncertainty in material properties is through safety factors. In the load and resistance factor design (LRFD) methods (AASTHO LRFD 1998), strength reduction and load factors are used to account for the variability in the capacity of the structural material and the load demands, respectively. Karbhari and Seible (2000) have proposed strength reduction factors for composite materials that account for variations due to the material system, processing method, level of cure, performance level in processing, and degradation in material properties over time due to environmental effects. Thus, variations in all of these design characteristics must be studied and understood in order to develop appropriate strength reductions factors for design.

Another problem facing biocomposite materials for use in civil applications is the lack standard material systems and structural components that can be easily selected by designers. At this stage in the development of biocomposite materials and structural components, it is not feasible to develop standard materials and sections. However, once these materials have been developed, the development of standard sections and materials will facilitate and promote the use of biocomposite components.

Before biocomposite structural components can be implemented in the construction industry, automated manufacturing methods must be developed. In the following section various manufacturing processes that have been used for natural fiber composites are discussed (Brouwer 2000).

5.4.1 Automated Manufacturing

In general, the processing techniques for biocomposites are similar to those for glass fiber composites. Several processes are available such as compression molding, sheet-molding compound, and resin transfer molding (Brouwer 2000, Drzal et al. 2002). However, vacuum assisted resin transfer molding VARTM has be shown to be an effective process for manufacturing cellular structures using both glass fibers, and natural fibers (Shenton et al. 2002, Stoll and Banerjee 2001, Berenberg 2003).

VARTM is a clean, closed mold process that can be used to manufacture biocomposites (Brouwer 2000). The process involves placing the dry fibers in a mold, closing the mold with a thin bagging film, and injecting resin. The resin is forced through the sample using a vacuum pump. Thus, the VARTM process allows manufacturing of very large parts with high mechanical properties and complex shapes, which is ideal for manufacturing large structural components. A common problem with natural fibers is the springy character of the fibers. One solution is to pre-form the fibers into pressed mats for a more compact and manageable shape.

VARTM manufacturing was studied experimentally by manufacturing and testing cellular plates similar to those used in the structural experimental program. The results of the manufacturing study are provided in the following sections.

5.4.2 VARTM Cellular plates

The automated manufacturing of cellular plates using VARTM method was studied experimentally with the aim of showing the viability of using this method for the manufacturing of biocomposite cellular components. The study included manufacturing and testing of laboratory-scale cellular plates with varying material systems. A diagram of the overall VARTM manufacturing process used in the experimental study is shown in Figure 5.1. Selective material systems from the material experimental program (Chapter 2) and the cellular plate molds from the structural experimental program (Chapter 3) were used. The workability of the natural fiber material systems was improved for VARTM manufacturing by developing novel hybrid bio-fiber pre-form fabrics, which consisted of a chopped bio-fiber core with synthetic or natural fabric face sheets. The hybrid material system was bound together by compression.

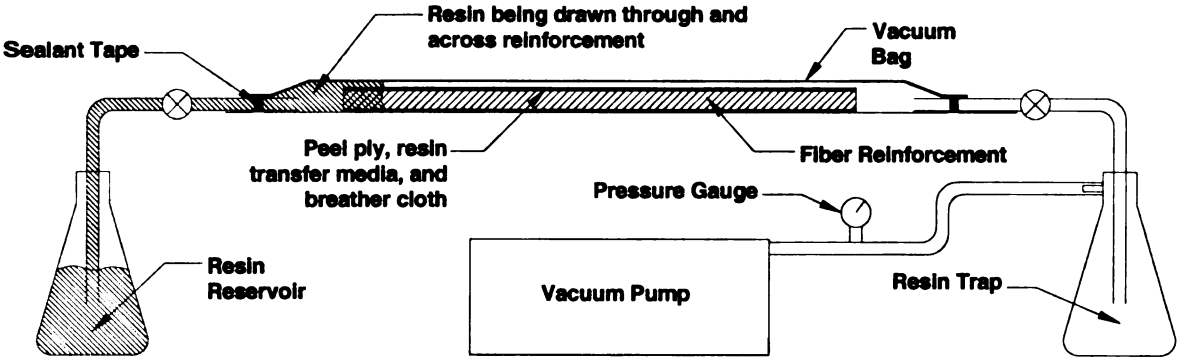

Figure 5.1. Schematic of the VARTM manufacturing process

It should be noted that the scope of the experimental study was aimed towards showing the feasibility of this manufacturing method for automated manufacturing of cellular plates. Thus, multiple tests of equal samples were not considered and optimization of the manufacturing procedure was not explored.

5.4.2.1 Materials and Constituents

The VARTM cellular plates were manufactured with hybrid fabric pre-forms consisting of a chopped raw hemp fiber core and face sheets of either woven jute, randomly orientated glass, or unidirectional carbon fabrics. Two types of pre-forms were used for the VARTM program: (i) raw hemp core with jute face sheets (Figure 5.2), and (ii) raw hemp fiber core with hybrid chopped glass strain mat and unidirectional carbon face sheets (Figure 5.3). The pre-form with a raw hemp core and glass/carbon face sheets was designed such that when placed in the cellular plate mold the carbon layers would only be on the top and bottom of the plate (Figure 5.3). A polyester resin system similar to that of the experimental program in Chapter 2 was used, with the exception that 10% styrene monomer was added to reduce the viscosity for infusion. Thus, the fibers, fabrics, and resin system used for the VARTM cellular plates were essentially the same as those used in the material experimental study described in Chapter 2.

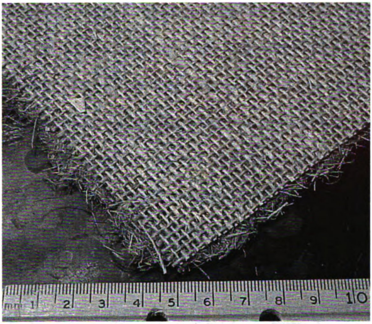

Figure 5.2. Hybrid pre-form fabric: raw hemp core with jute face sheets

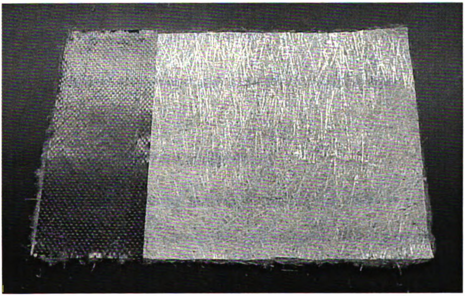

Figure 5.3. Hybrid pre-form fabric: raw hemp core with glass face sheets and top and bottom carbon

The springy nature of the raw hemp fibers (and natural fibers in general) made the hybrid pre-form fabric thick (Figure 5.4a) and difficult to handle and fold when placing the fabric in the cellular plate mold. Thus, to improve workability, the pre-form fabrics were compressed prior to manufacturing under 550 kPa of pressure at 100°C for 5 minutes (Figure 5.4b). The pre-compression of the pre-form fabric decreased the thickness (Figure 5.4c), bound the materials together, and made handing, folding, and placement of the fabric more convenient. All the hybrid pre-form fabrics used for the VARTM experimental program were pre-compressed, as previously described.

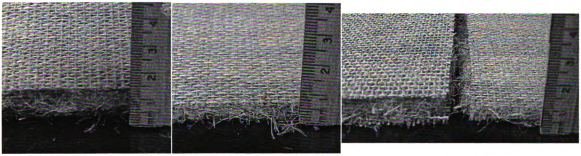

(a) Uncompressed dry hybrid pre-form, with hemp core and jute fabric face sheets

(b) Dry hybrid pre-form compressed at 100°C under 80 psi for 5 minutes

(c) Thickness comparison of dry hybrid pre-forms

Figure 5.4. Pre-compression of the hybrid fabric pre-forms

5.4.2.2 Manufacturing of VARTM Cellular Plates

The VARTM manufacturing process of the cellular plates is divided into three main steps: (i) placement of the vacuum bagging materials and dry pre-form fabric, (ii) vacuum bagging of the setup, and (iii) resin infusion. Each of these steps is detailed in the following paragraphs with descriptions and photographic summaries.

The VARTM setup was prepared on a movable cart with a vacuum pump on the bottom of the cart, and the mold and sample on the top surface. The vacuum bagging materials were placed in the same cellular plate mold that was used in the structural experimental program (Chapter 3). First, a non porous Teflon release ply was placed in the bottom of the mold to prevent the sample from sticking to the mold after curing (Figure 5.5a). A breather ply was then placed on top of the Teflon ply to absorb excess resin for the sample (Figure 5.5b). Resin transfer media (high density polyethylene, green house shade cloth) was placed on top of the breather ply to promote uniform flow of the resin over the sample (Figure 5.5c). A porous bleeder ply (polyester cloth) was placed on top of the resin transfer media to achieve a smooth surface after curing and absorb excess resin from the sample (Figure 5.5d). A layer of porous peel ply was then placed on top of the bleeder ply to allow excess resin to be squeezed out of the sample (Figure 5.5). The vacuum bagging materials were placed so that they can be wrapped around the entire samples once the fibers are in place. With the vacuum bagging materials in place, the pre-form bio-fabric was then placed in the mold (Figure 5.5f)

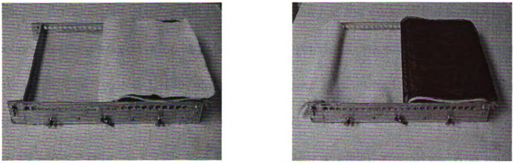

(a) Non-porous release ply (b) Breather ply

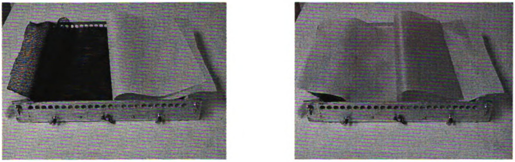

(c) Resin transfer media (d) Bleeder ply

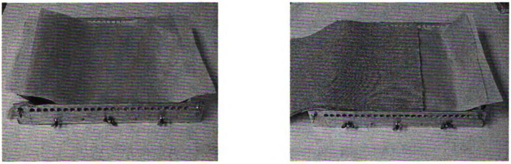

(e) Porous release ply (f) Dry pre-form fabric

Figure 5.5. Preparation vacuum bagging materials

Two methods were used for placing the pre-form fabric in the cellular plate mold. The first method used three discontinuous fabrics to comprise the top and bottom face sheets, and the core cells were achieved by a sinusoidal layout of the fiber fabric around the mold rods (Figure 5.6a). The second method used one continuous fabric to comprise the entire unit continuing the top and bottom face sheets into the sinusoidal core layout (Figure 5.6b). The first procedure for placing the pre-form fabric lead to open side walls and general difficulty in placing the fabrics, especially at the ends of the sinusoidal core. The second method was developed to improve the previous procedure for placing the pre-form fabric. The typical fabric placement process is summarized in the photograph sequence shown in Figure 5.7. A continuous pre-form fabric was used to first create the bottom face sheet (Figure 5.7a). The fabric was then wrapped around the first rod in the plate mold to create the side wall (Figure 5.7b), and wrapped through the remaining rods to create the sinusoidal core (Figure 5.7c-d). The fabric was then wrapped over the final rod to create the side wall and top face sheet (Figure 5.7e). Both procedures used the same vacuum bagging material layout.

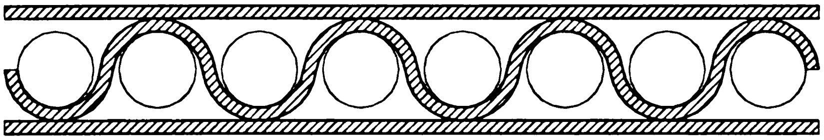

(a) Wrapping procedure using three discontinuous pre-form fabrics

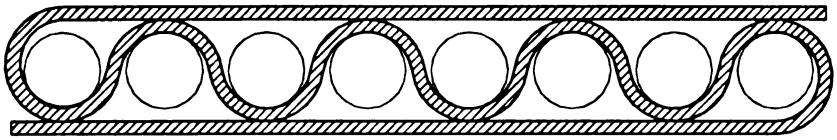

(b) Wrapping procedure using one continuous pre-form fabric

Figure 5.6. Placement of pre-form bio-fabric in the cellular plate mold

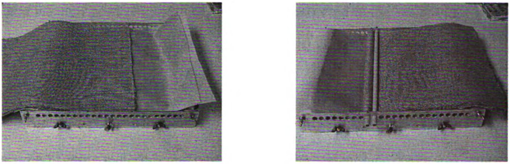

(a) Dry fiber sample: bottom layer

(b) Wrapping of fabric core

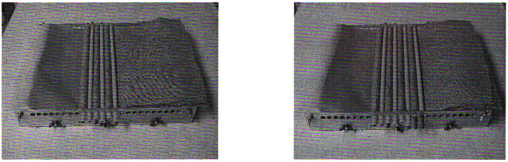

(c) Wrapping of fabric core

(d) Wrapping of fabric core

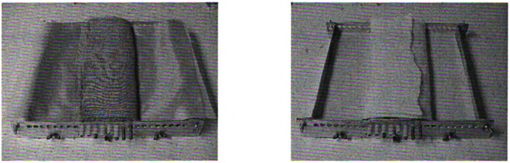

(e) Dry fiber sample: top layer

(f) Vacuum bagging materials wrapped over the dry fabric pre-form

Figure 5.7. Preparation of dry pre-form fabric and vacuum bagging materials

Once the dry fabric pre-form and vacuum bagging materials were set in the cellular plate mold, a strip of sealant tape was placed around the edge of the sample, over the faceplate, and under the rods (Figure 5.8a). Another strip of sealant tape was placed between the faceplate and the body of the mold to create an airtight seal between them. Breather cloth was placed over the ends of the rods to prevent the inner steel rods from puncturing the vacuum bag when under pressure (Figure 5.8a). The resin ports (Figure

5.8b) and vacuum ports (Figure 5.8c) were then connected to the sealant tape by splicing the tape cover and attaching the tubes with additional sealant tape. The resin and vacuum ports were covered with additional resin transfer media and breather cloth to improve resin transfer and prevent the vacuum bag from blocking the ports (Figure 5.8a). With the vacuum bagging materials and ports in place, the sealant tape cover was removed and the vacuum bag was attached to the mold (Figure 5.8a). The Polyester resin system was added to the resin reservoir (Figure 5.8d) and the resin trap was connected to a pressure gauge, which was connected to a cryogenic trap (Figure 5.8e). A valve was used between the resin reservoir and the sample to control the flow of the resin during the resin infusion process (Figure 5.8d). The cryogenic trap was filled with dry ice and acetone to condense and trap any vapors (styrene) from traveling into the pump. The typical vacuum bagging procedure is summarized in the photograph sequence shown in Figure 5.8.

(a) Vacuum bagging

(b) Resin ports

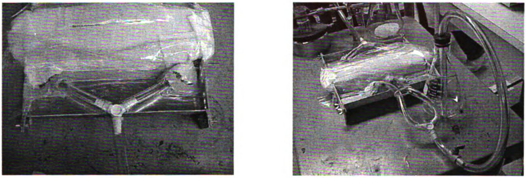

(c) Vacuum ports

(d) Resin reservoir and valve

(e) Resin trap and cryogenic trap

(f) Completed VARTM setup

Figure 5.8. Sample with vacuum bag, resin ports, and vacuum ports

The resin infusion process began by compressing the sample under vacuum pressure (Figure 5.9a) before resin was injected into the system. Once the sample was under vacuum pressure, the valve between the resin reservoir and the sample was opened to allow the resin to be pulled into the mold (Figure 5.9b). The initial resin flow front followed a fan-like pattern from the resin ports towards the vacuum ports (Figure 5.9b-f).

Once the sample was completely impregnated with resin, the valve between the resin reservoir and the sample was closed so that no additional resin would be pulled into the system and any excess resin could be removed. The system was kept under vacuum pressure for approximately one hour to allow the resin to gel and avoid air voids that could be created from the "springy" short natural fibers.

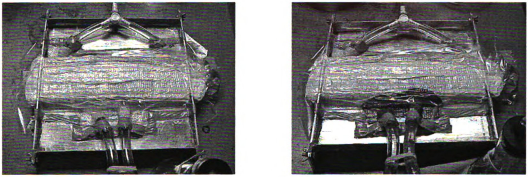

(a) Sample under vacuum pressure (b) t = 1 minute

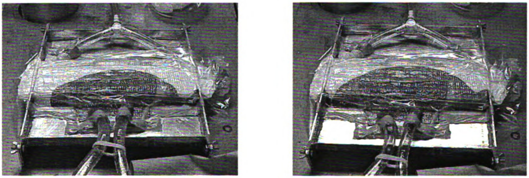

(c) t = 2 minutes (d) t = 3 minutes

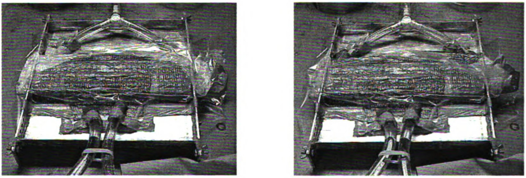

(e) t = 5 minutes (f) t = 12 minutes

Figure 5.9. Resin flow front movement (total time to complete impregnation = 12 minutes)

Once the sample had gelled under vacuum pressure, the pressure pump was turned off and the ports were detached from the mold. The sample was then oven cured with the mold and vacuum bagging materials. The sample was cured for 6 hours at 100°C. A lower curing temperature was used to avoid melting the resin transfer media, which is made of high density polyethylene. Steel plates were placed on the sample during curing to improve the density and quality of the sample.

To evaluate if the cellular plates made by VARTM were properly wet out through their entire depth, a cellular plate was cut open to inspect the core material (Figure 5.10). Inspection of the sample showed that the entire depth of the sample had been properly infused with resin.

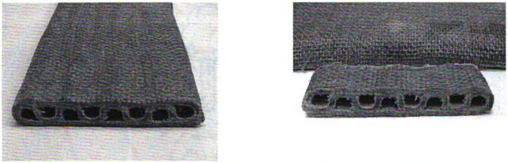

(a) Cut through the sample

(b) Wet-out through the entire depth

Figure 5.10. Cut through VARTM cellular plate showing fiber wet-out through the entire depth

5.4.3 Testing of VARTM Cellular Plates

The VARTM manufactured cellular plates were tested in three-point bending using the same setup described in section 3.3.4. Three VARTM cellular plates were tested, as shown in Table 5.1 and Figure 5.11 through Figure 5.13.

All test units were of cellular plate type 1 (Figure 3.4) with a relative density of 0.56. A polyester resin system with 10% styrene monomer was used as the matrix for all test units. Notice that with VARTM manufacturing it was possible to achieve much higher fiber weight fractions that by hand layup (Table 5.1). The increase in fiber weight fraction by VARTM manufacturing is mainly due to the use of dense bio-fiber pre-form fabrics, which avoid the manufacturing issues encountered with the loose springy natural fibers in the experimental studies of Chapter 3.

Table 5.1. VARTM cellular plate test matrix

Pre-Form Fabric Type	*Placement Method*	*Test Unit ID*	*Fiber Weight Fraction (%)*
Raw hemp fiber core, jute fabric face sheets	Non-wrapped	CP1-01	40%
Raw hemp fiber core, jute fabric face sheets	Wrapped	CP1-02	36%
Raw hemp fiber core, glass strand mat face sheets, top and bottom carbon layers	Wrapped	CP1-C	47%

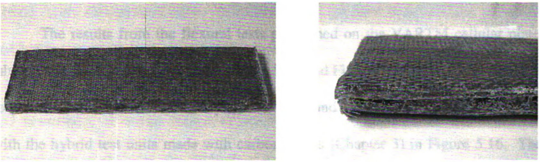

(a) Overall view of the sample

(b) View of the side wall

Figure 5.11. VARTM cellular plate with a non-wrapped jute fabric/raw hemp core pre-form (40% fibers by weight)

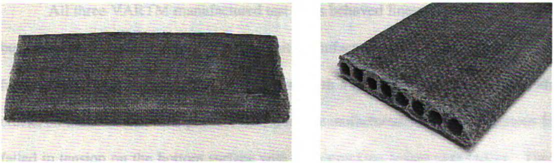

(a) Overall view of the sample

(b) View of the side wall

Figure 5.12. VARTM cellular plate with a wrapped jute fabric/raw hemp core pre-form

(36% fibers by weight)

(a) Overall view of the sample

(b) View of the side wall

Figure 5.13. VARTM cellular plate with a warpped glass strand mat/raw hemp core pre-form and top and carbon layers (47% fibers by weight)

5.4.3.1 Flexural Test Results and Observed Behavior

The results from the flexural tests performed on the VARTM cellular plates are tabulated in Table 5.2 and shown in Figure 5.14 and Figure 5.15. The force-displacement response of the hybrid VARTM plate with top and bottom carbon layers is compared with the hybrid test units made with carbon layers (Chapter 3) in Figure 5.16. The test results of the VARTM cellular plates are compared with the results from all the cellular plates made by hand layup tested in the structural experimental program (Chapter 3) in Table 5.3.

All three VARTM manufactured test units behaved linear-elastically up to failure but failed in different modes. The test unit manufactured with three separate pre-form fabrics failed by delamination of the top layer with a loud snapping noise and no visible cracks on the exterior of the plate. The test unit manufactured with one continuous fabric failed in tension on the bottom surface with fiber cracking noises near failure. The unit maintained a nominal load, at approximately 10% of the peak load, after tension failure in the bottom layer. The test unit manufactured with the top and bottom carbon layers failed in buckling of the top carbon layer. After buckling of the top carbon layer the sample did not retain significant stiffness from the bottom carbon layer and rapidly lost its load carrying capacity (Figure 5.14).

All VARTM cellular plates had a higher stiffness compared to the samples made by hand layup (Table 5.3). For example, the VARTM cellular plate with the woven pre-form had a stiffness of 582 N/mm while the green hemp cellular plate with top and bottom jute fabric layers had a stiffness 309 N/mm (Table 5.3), an improvement of 88%. This improved stiffness is mainly due to the higher fiber content achieved using the VARTM process (Table 5.1). The hybrid VARTM cellular plate with top and bottom carbon fabric also showed improved stiffness over the hand layup cellular plate with top and bottom carbon layers. The VARTM cellular plate with top and bottom carbon had a stiffness of 1,605 N/mm while the hand layup cellular plate with top and bottom carbon had a stiffness of 1,480 N/mm (Table 5.3), an improvement of 8%. Despite the improvement in stiffness, the strength of the VARTM cellular plate with top and bottom carbon (5,596 N) was much lower that the hand layup cellular plate (11,010 N), see Figure 5.16. The reduction in strength in the VARTM cellular plate is due to delamination of the top layer of the pre-form fabric after buckling of the top carbon layer. Because the pre-form fabric is only bonded to the core in a limited number of locations (see Figure 5.6) the plate is more susceptible to delamination than the hand layup sample, which has the carbon layer built integrally with the core.

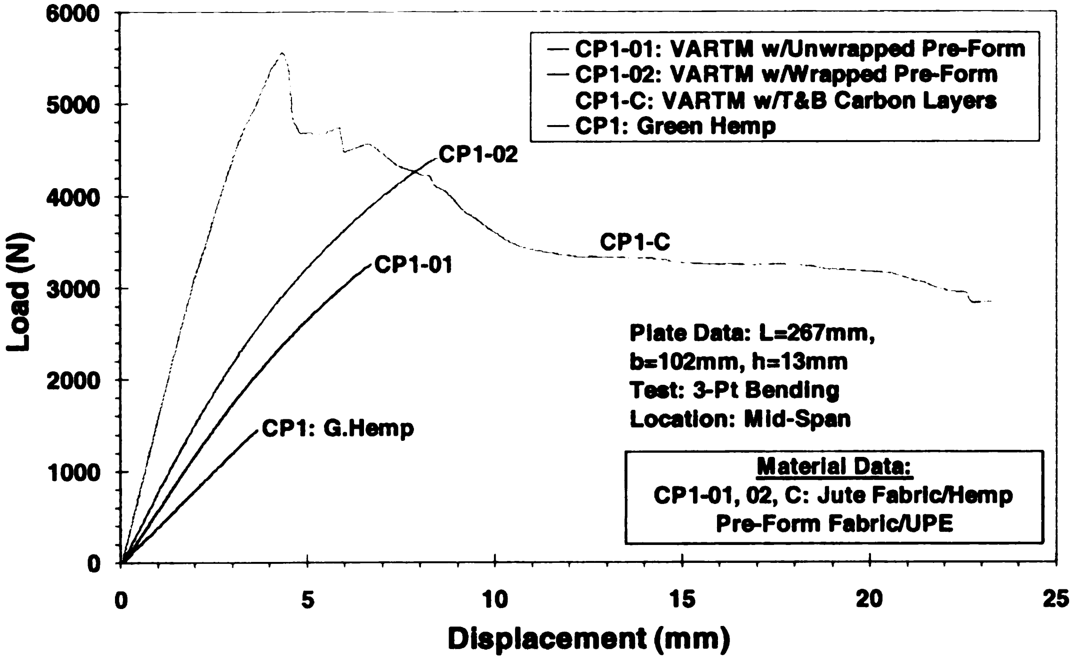

Figure 5.14. Force versus displacement response at mid-span of VARTM cellular plates, compared with a green hemp plate made by hand layup

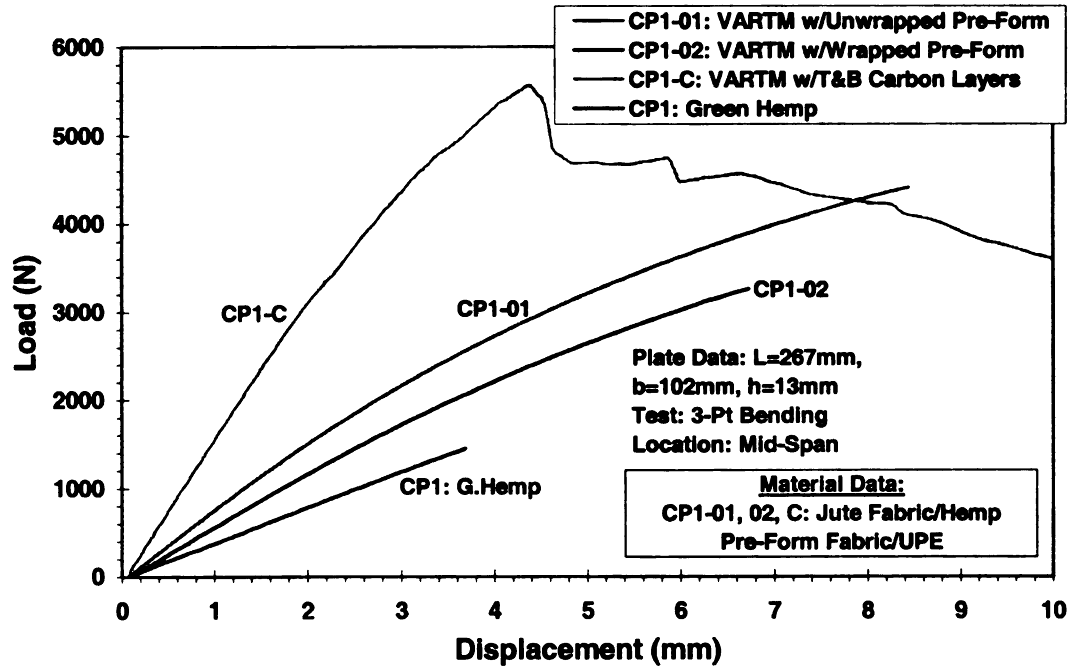

Figure 5.15. Zoomed-in view of the force displacement response of VARTM cellular plates

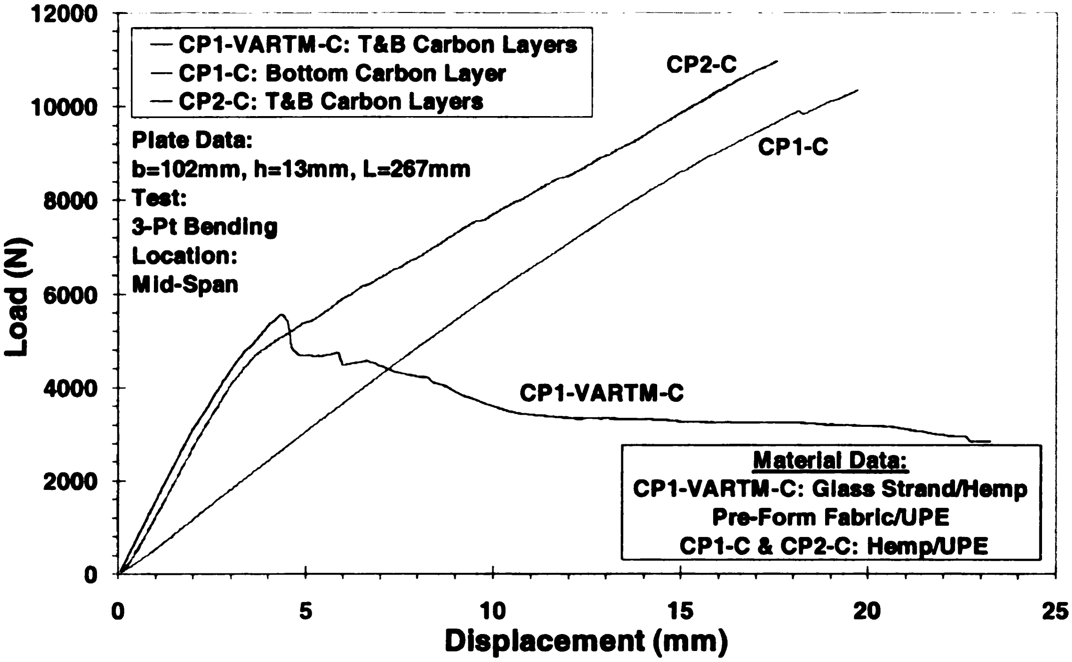

Figure 5.16. Comparison of the force versus displacement response at mid-span of the VARTM plate with top and bottom carbon versus the hand layup cellular plates with carbon face sheets

Table 5.2. Flexural test results summary of VARTM cellular plates

Material	*Fibers by Wt. (%)*	*ID*	*Max Load (N)*	*Max Displ. (mm)*	*Stiffness (N/mm)*
Jute/Chopped Hemp Fabric (non-wrapped)	40	CP1-01	3655	5.99	729
Jute/Chopped Hemp Fabric (wrapped)	36	CP1-02	3287	8.44	582
Glass/Chopped Hemp Fabric T&B Carbon	47	CP1-C	5596	23.25	1605

Table 5.3. Flexural test results of the VARTM plates with all cellular plates tested in Chapter 3

Material	*Fibers by Wt.* (%)	*ID*	*Max Load* (N)	*Extensometer Max Displ.* (mm)	*Stiffness* (N/mm)
G.Hemp/UPE	10	CP1	1483	3.65	406
G.Hemp/UPE - T&B Glass	10	CP1-G	2237	8.42	320
G.Hemp/UPE - Bottom Carbon	10	CP1-C	10397	19.70	592
G.Hemp/UPE - T&B Jute	10	CP1-J	2197	6.95	309
Raw Hemp/UPE	10	CP1	1859	5.67	323
Raw Hemp/UPE	10	CP2	2557	5.39	502
Raw Hemp/UPE - T&B Carbon	10	CP2-C	11010	17.56	1480
Flax/UPE	20	CP1	1172	6.16	196
Flax/UPE - T&B Jute	20	CP1-J	1980	7.77	259
Polyester	0	CP1	1764	9.45	186
Jute/Chopped Hemp Fabric (non-wrapped)	40	CP1-01	3655	5.99	729
Jute/Chopped Hemp Fabric (wrapped)	36	CP1-02	3287	8.44	582
Glass/Chopped Hemp Fabric T&B Carbon	47	CP1-C	5596	23.25	1605
Douglas Fur	--	DF-P	3495	11.19	629
Orientated Strand Board	--	OSB-P	917	5.56	196
Particle Board	--	PB-P	694	6.15	123

5.5 Recommendations for Future Work

Recommendations for future work based on the findings of this study are provided for both the biocomposite material systems and the structural forms in which the biocomposite materials can be used. The future work for the material systems mainly lies in the optimization of treatments for the fibers and resin, which can improve physical and mechanical properties needed for structural applications Future work in structural forms lies in optimization of the hierarchical structure and automated manufacturing of full-scale components. Once the material system, structural form, and manufacturing procedure have been optimized, probabilistic studies should be performed to define strength reduction factors for design purposes. For design using the LRFD approach the variations due to the material system, processing method, level of cure, performance level in processing, and degradation in material properties over time and due to environmental effects are needed in order to determine an overall safety factor (Karbhari and Seible 2000). Thus, the deviations in material properties and the processing effects must be studied and measured.

5.5.1 Material Systems

Future work is needed in the characterization of biocomposite materials for physical properties such as durability, weathering, creep, and susceptibility to fire, as these properties are important for structural applications. In addition, the compression behavior of biocomposite materials remains to be characterized. Once these properties are assessed, future work is needed in the study of optimal fiber and resin treatments for enhancement of the properties of biocomposite material systems. Possible treatments include chemical treatments of the fibers for improved fiber-matrix adhesion, sizing of fibers for the resin, improved processing of fibers, and the use of nano-reinforcement in the resin (Vaia 2002). Treatments should be targeted for mechanical and physical properties that may limit the use of biocomposites in load-bearing applications. The treatments considered should also be economical to keep the low cost appeal of biocomposites.

5.5.2 Structural Forms

Future work is needed in the optimization of hierarchical structures for biocomposite cellular beams and plates. Optimization studies of hierarchical structures can be performed using the analysis procedure proposed in Section 4.5. The studies should not only be aimed at efficient structures in flexure, but other properties such as thermal conductivity, blast, impact, and their combinations, to provide efficient structural forms for biocomposite materials. In addition, three-dimensional cellular structures and micro-sandwiching of the cell walls may be considered in the optimization of hierarchical structures.

Full-scale manufacturing of biocomposite structural components must also be studied in the future. Based on the results from the research work reported here, VARTM is recommended for full-scale manufacturing of cellular biocomposite structural components. The manufacturing procedure should be optimized for obtaining high fiber volume fractions and fast production cycles for high-volume manufacturing in the construction industry. Collaboration with industry may be helpful in developing the manufacturing procedure.

CHAPTER 6 CONCLUSIONS

Results from the reported studies has shown that hybrid cellular biocomposite beams and plates not only have the potential to serve as primary load bearing components, but that they can compete with conventional structural materials. In particular, the findings in this study have led to the following conclusions regarding the biocomposite material systems:

- The mechanical properties of biocomposite materials can compete with E-glass fiber reinforced composites.
- Biocomposite material systems have deficiencies with respect to impact strength, and moisture absorption.
- The use of hybrid material systems with synthetic or aligned fiber face sheets and chopped natural fiber cores dramatically improve the mechanical properties of biocomposites.
- Hybrid material systems with fabric face sheets and chopped natural fiber cores can serve as novel engineered pre-forms, or micro-sandwiches, for VARTM manufacturing.

The findings in this study have also led to the following conclusions regarding the biocomposite structural systems:

- Cellular biocomposite structures can serve as load bearing structural components, and compete with conventional solutions.

- The use of hierarchical cellular structures improves the structural performance of biocomposite beams and plates.
- The use of jute, glass strand mat, and carbon face sheets can dramatically improve the stiffness and strength of cellular biocomposite structural components.
- Vacuum assisted resin transfer molding (VARTM) is a viable method for automated manufacturing of biocomposite cellular structures.

In civil construction, biocomposite structural components can be used as flooring systems and pre-fabricated components in residential and commercial construction, deck systems in highway bridges, and complete superstructures for small pedestrian bridges. Further research, development, and collaboration between researchers and industry are needed in order for biocomposite structural components to become a reality in load-bearing applications. However, the availably of low cost structural components based on renewable resources will be a great asset for current and future structural applications.

REFERENCES

REFERENCES

AASHTO-LRFD Bridge Design Specifications. American Association of State Highway and Transportation Officials, 1998, Washington, D.C.

Allen, H.G. Analysis and Design of Structural Sandwich Panels, Pergamon Press, 1969, Oxford.

APA Engineered Wood Association. Company Homepage [online] Available: <http://www.apawood.org/> (Accessed July 2003).

Ashby, M.F. Materials Selection in Mechanical Design. Butterworth Heinemann, 1999, Oxford, UK.

Ashby, M.F. (1991). "Materials and Shape." *Acta Metallugical et Materialia*, 39, 1025-1039.

Barbero, E. and GangaRao, H.V.S. (1991). "Structural Applications of composites in Infrastructure: Part I." *SAMPE Journal*, Vol. 27, No. 6, 9-16.

Barbero, E. and GangaRao, H.V.S. (1992). "Structural Applications of composites in Infrastructure: Part II." *SAMPE Journal*, Vol. 28, No. 1, 9-15.

Barker, R.M and Puckett, J.A. Design of Highway Bridges: Based on AASHTO LRFD, Bridge Design Specifications. John Wiley, 1997, New York, NY.

Baxter, W.J. (1992). "The Strength of Composites with Randomly Oriented Short Fibers." *Proceedings of the ASC 7th Annual Technical Conference*, University Park, Pa, 615-623.

Berenberg, B. (2003). "Manufacturers Welcome New Reinforcement Forms." *Composites Technology*, April, 12-16.

Biswas, S., Mittal, A. and Srikanth, G. (2002). "Composites: A Vision for the Future." *Proceedings of the International Conference and Exhibition on Reinforced Plastics*, Indian Institute of Technology, Madras, 26-36.

Biswas, S., Srikanth, G. and Nangia, S. (2001). "Development of Natural Fibre Composites in India." *Proceedings of the Composites Fabricators Association's Conference*, Tampa, FL.

Brouwer, W.D. (2000). "Natural Fibre Composites: Where Can Flax Compete with Glass?" SAMPE Journal, Vol. 36, No. 6, 18-23.

Christensen, R.M. and Waals, F.M. (1972). "Effective Stiffness of Randomly Oriented Fibre Composites." *Journal of Composite Materials*, 6, 518-532.

Ghali, A. and Nevill A.M. Structural Analysis: A Unified Classical and Matrix Approach. 4th edition, E&FM Spon, 1997, London, UK.

Gunderson, S.L. and Thorp, K.E.G. (1993). "Natural Cellular and Sandwich Structures for Innovative Design Concepts." *Proceedings of the ASC 8th Annual Technical Conference*, Cleveland, OH, 431-440.

Chen, P.E. (1971). "Strength Properties of Discontinuous Fiber Composites." Polymer Engineering and Science, Vol. 11, No. 1, 51-56.

Daimler Chrysler Corporation (2001). "Daimler Chrysler 2001 Environmental Report." Auburn Hills, MI.

Drzal, L.T., Mohanty, A.K., Mehta, G. and Misra M. (2002). "Low-Cost, Bio-Based Materials for Housing Applications." *International Conference on Advances in Building Technology*, Hong Kong, China, 225-232.

Gibson, L.J. and Ashby, M.F. Cellular Solids: Structure and Properties. 1st edition, Pergamon Press, 1988, Oxford, UK.

Gibson, R.F. Principles of Composite Material Mechanics. McGraw-Hill, 1994, New York, NY.

Giurgiutiu, V. and Reifsnider, K.L. (1994). "Development of Strength Theories for Random Fiber Composites." *Journal of Composites technology and Research*, Vol. 16, No. 2, 103-114.

Gunderson, S.L. and Thorp, K.E.G. (1993). "Natural Cellular and Sandwich Structures for Innovative Design Concepts." *Proceedings of the ASC 8th Annual Technical Conference*, Cleveland, OH, 431-440.

Halpin, J.C. (1969). "Stiffness and Expansion Estimates for Oriented Fiber Composites." *Journal of Composite Materials*, 3, 732-734.

Halpin, J.C. and Pagano, N.J. (1969). "The Laminate Approximation for Randomly Oriented Fibrous Composites." Journal of Composite Materials, 3, 720-724.

Halpin, J.C. and Tsai, S.W. (1969). *Effects of Environmental Factors on Composite Materials*, Technical Report AFML-TR-67-423, June.

Hibbler,R.C. Mechanics of Materials. 3rd Edition, Prentice Hall, 1994, Upper Saddle River, NJ.

Huang, J.S. and Gibson, L.J. (1995). "Microstructural Design of Cellular Materials: Honeycomb Beams and Plates." *Acta Metallugical et Materialia*, 43, 1643-1650.

Insulspan. Company Homepage. [online] Available: <http://www.insulspan.com/> (Accessed July 2003).

International Building Code. International Code Council, 2000, Falls Church, VA.

Jones, R.M. Mechanics of Composite Materials. 2nd edition, Taylor and Francis, 1999, Philadelphia, PA.

Karbhari, V.M. and Seible, F. (2000). "Fiber Reinforced Composites – Advanced Materials for the Renewal of Civil Infrastructure." *Applied Composite Materials*, 7, 95-124.

Lees, J.K. (1968). "A Study of the Tensile Strength of Short Fiber Reinforced Plastics." Polymer Engineering and Science, Vol. 8, No. 3, 195-201.

Mathcad. Computer Software. Mathsoft, 2001 Professional, 2000. Cambridge, MA.

Mathematica. Computer Software. Wolfram Research, version 4.2, 2002. Champaign, IL.

MATLAB. Computer Software. The MathWorks, version 6.5, 2003. Natick, MA.

Mishra, S., Mohanty, A.K., Drazal, L.T., Misra, M., Parija, S., Nayak, S.K. and Tripathy, S.S. (2003). "Studies on Mechanical Performance of Biofiber/Glass Reinforced Polyester Hybrid Composites." *Composites Science and Technology*, 63, 1377-1385.

Mishra, S., Misra, M., Tripathy, S.S., Nayak, S.K. and Mohanty, A.K. (2002). "The Influence of Chemical Surface Modifications on the Performance of Sisal-Polyester Biocomposites." *Polymer Composites*, 23, 164-170.

Mohanty, A.K., Misra, M. and Drzal, L.T. (2001). "Surface Modifications of Natural Fibers and Performance of the Resulting Biocomposites: An Overview." *Composite Interfaces*, 8, 313-343.

Mohanty, A.K., Misra, M. and Hinrichsen, G. (2000). "Biofibers, Biodegradable Polymers and Biocomposites: An Overview." *Macromolecular Materials and Engineering*, Vol. 276/277, 1-24.

Nickle, J. and Riedel, U. (2003). "Activities in Biocomposites." Materials Today, Vol. 6, No. 4, 44-48.

PCI Design Handbook: Prestressed and Precast Concrete. Precast Concrete Institute, 1999, Chicago, IL.

Phenix Biocomposites. Company Homepage [online] Available: <http://www.phenixbiocomposites.com/> (Accessed July 2003).

Piggott, M.R. Load-Bearing Fibre Composites. Pergamon Press, 1980, Oxford, UK.

Rout, J., Misra, M., Tripathy, S.S., Nayak, S.K. and Mohanty, A.K. (2001). "The Influence of Fibre Treatment on the Performance of Coir-Polyester Composites." *Composites Science and Technology*, 61, 1303-1310.

Shenton III, H.W., Wool, R.P., Hu, B., O'Donnell, A.O., Bonnaillie, L., Can, E., Chapas, R. and Hong, C. (2002). "An All-Natural Composite Material Roof System for Residential Construction." *International Conference on Advances in Building Technology*, Hong Kong, China, 255-262.

Stoll, F. and Banerjee, R. (2001), "Measurement and Analysis of Fiber-Composite-Reinforced-Foam Sandwich Material Properties." *Proceedings of the 46th International SAMPE Symposium and Exhibition*, Long Beach, CA, 1938-1946.

Strongwell. Company Homepage. [online] Available:<http://www.strongwell.com/> (Accessed July 2003).

Tsai, S.W. and Pagano, N.J. (1968). "Invariant Properties of Composite Materials." *Composite Materials Workshop*, Lancaster, PA, 233-252.

Thompson, D.W. On Growth and Form. Cambridge University Press, 1961, Cambridge, MA.

Timoshenko, S.P. (1925). "Analysis of Bi-Metal Thermostats." *Journal of the Optical Society of America*, 11, 233-255.

Vaia, RA (2002). "Polymer Nanocomposites Open a New Dimension for Plastics and Composites." *The AMPTIAC Newsletter*, Vol. 6, No. 1, 17-24.